Yrjö Rauste

Techniques for wide-area mapping of forest biomass using radar data

Techniques for wide-area mapping of forest biomass using radar data

Yrjö Rauste

VTT Information Technology

Abstract

Aspects of forest biomass mapping using SAR (Synthetic Aperture Radar) data were studied in study sites in northern Sweden, Germany, and south-eastern Finland. Terrain topography – via the area of a resolution cell – accounted for 61 percent of the total variation in a Seasat (L-band) SAR scene in a hilly and mountainous study site.

A methodology – based on least squares adjustment of tie point and ground control point observations in a multi-temporal SAR mosaic dataset – produced a tie point RMSE (Root Mean Square Error) of 56 m and a GCP RMSE of 240 m in the African mosaic of the GRFM (Global Rain Forest Mapping) project. The mosaic consisted of 3624 JERS SAR scenes. A calibration revision methodology – also based on least squares adjustment and points in overlap areas between scenes – removed a calibration artifact of about 1 dB.

A systematic search of the highest correlation between forest stem volume and backscattering amplitude was conducted over all combinations of transmit and receive polarisations in three AIRSAR scenes in a German study site. In the P-band, a high and narrow peak around HV-polarisation was found, where the correlation coefficient was 0.75, 0.59, and 0.71 in scenes acquired in August 1989, June 1991, and July 1991, respectively. In other polarisations of P-band, the correlation coefficient was lower. In L-band, the polarisation response was more flat and correlations lower, between 0.54 and 0.70 for stands with a stem volume 100 m^3/ha or less.

Three summer-time JERS SAR scenes produced very similar regression models between forest stem volume and backscattering amplitude in a study site in south-eastern Finland. A model was proposed for wide area biomass mapping when biomass accuracy requirements are not high. A multi-date regression model employing three summer scenes and three winter scenes produced a multiple correlation coefficient of 0.85 and a stem volume estimation RMSE of 41.3 m^3/ha. JERS SAR scenes that were acquired in cold winter conditions produced very low correlations between stem volume and backscattering amplitude.

Preface

This thesis summarizes the work published in six papers over the period 1990–2005. All six papers can be considered to contribute to a theme "Techniques for wide-area mapping of forest biomass using radar data". The term "wide-area mapping" here is understood to cover such mapping situations where the whole mapping area cannot be covered by a single space-borne SAR scene.

The supervisor of the work is Professor Henrik Haggren of the Laboratory of Photogrammetry and Remote Sensing in the Department of Surveying, Helsinki University of Technology, Finland. The work has been carried out at the VTT Technical Research Centre of Finland (Espoo, Finland) and the Joint Research Centre (JRC, Ispra, Italy) of the European Union.

List of Appended Papers

This thesis is based on six papers published between the years 1990 and 2005:

1. Rauste, Y. 1990. Incidence-angle dependence in forested and non-forested areas in Seasat SAR data, International Journal of Remote Sensing, Vol. 11, No. 7, p. 1267–1276, reprinted with permission from Taylor and Francis Journals UK, (http://www.tandf.co.uk).

2. Rauste, Y., De Grandi, G., Richards, T., Rosenqvist, Å., Perna, G., Franchino, E., Holecz, F., and Pasquali, P. 1999. Compilation of a bi-temporal JERS SAR mosaic over the African rain forest belt in the GRFM project, Proceedings of IGARSS'99, 28 June–2 July 1999, Hamburg, Germany, p. 750–752, reprinted with permission from IEEE.

3. De Grandi, G., Mayaux, P., Rauste, Y., Rosenqvist, Å., Simard, M., and Saatchi, S. 2000. The global rain forest mapping project JERS-1 radar mosaic of tropical Africa: Development and product characterization aspects, IEEE Transactions on Geoscience and Remote Sensing, Vol. 38, No. 5, September 2000, p. 2218–2233, reprinted with permission from IEEE.

4. Rauste, Y., Häme, T., Pulliainen, J., Heiska, K., and Hallikainen, M. 1994. Radar-based forest biomass estimation, International Journal of Remote Sensing, Vol. 15, No. 14, p. 2797–2808, reprinted with permission from Taylor and Francis Journals UK, (http://www.tandf.co.uk).

5. Rauste, Y. 1993. Multitemporal analysis of forest biomass using AIR-SAR data, Proceedings of the 25th International Symposium, Remote Sensing and Global Environmental Change, 4–8 April, 1993, Graz, Austria, p. I-328–I-338, reprinted with permission from Altarum Institute.

6. Rauste, Y. 2005. Multi-temporal JERS SAR data in boreal forest biomass mapping, Remote Sensing of Environment, Vol. 97, p. 263–275, reprinted with permission from Elsevier[1].

---

[1]Reprinted from Remote Sensing of Environment, Vol. 97, Rauste, Y., Multi-temporal JERS SAR data in boreal forest biomass mapping, p. 263–275, Copyright(2005), with permission from Elsevier.

The work can be divided into four themes:

- Incidence-angle effects on radar backscatter in forests (Paper 1),

- Pre-processing techniques – block adjustment in mosaicking and block adjustment in calibration revision of SAR images (Papers 2 and 3),

- Radar backscatter of forests in various wavelengths and polarisations (Papers 4 and 5), and

- Multi-temporal L-band radar backscatter in forest biomass mapping (Paper 6).

Paper 1 was written in VTT in project SLARSAR. I was the sole author of Paper 1.

Papers 2 and 3 were written at the Joint Research Centre (JRC) of the European Union while I was a post doctoral grant holder in 1997–1999. In Paper 2, my responsibility was the development of the methodology for tie point production, block adjustment for SAR mosaicking, application of these techniques to the GRFM dataset of Africa, and evaluation of the results obtained in terms of mosaic geometry. In Paper 3, my contribution was the development of geometry revision and calibration methods and experimental results described in sections V, VI, and VII of Paper 3.

Paper 4 was written in VTT during project MAESTRO. My contribution to Paper 4 was the development of methods and obtaining the experimental results using AIRSAR polarimetric SAR data.

Paper 5 was written in VTT during project MAC-Europe. I was the sole author of Paper 5.

Paper 6 was written in VTT during project MODIS Biomass. I was the sole author of Paper 6.

Contents

List of Figures

List of Tables

1 Introduction

The synthetic aperture radar (SAR) satellites Seasat (Lewis *et al.* 1983, Moore *et al.* 1983), ERS-1 and 2 (ESA 1988), JERS-1 (NASDA 1988), Radarsat-1 (Williamson 1990), and Envisat (Louet 2001) have created an opportunity to map various properties of the earth's surface at high resolution using microwave radiation. Future SAR satellites such as ALOS (Shimada *et al.* 2005 and Shimada *et al.* 2002a) will further extend the capabilities of space-borne microwave remote sensing. Vegetation cover is an important characteristic of the earth's surface. Mapping forest and vegetation cover using radar has been studied extensively since Morain and Simonett (1967). The biomass of vegetation cover is needed especially in environmental and climatological studies, where the greatest amount of uncertainty arises from lack of information on biomass density (*e.g.,* Sader *et al.* 1989 and Häme *et al.* 2003). Since tree trunks are the most important raw material of the Paper and timber industries, information on forest biomass is also needed in sustainable forestry.

In many countries, fertile low-lying flat areas are typically in agricultural use. Forests tend to be in areas with more pronounced topography. When mapping forest biomass – or other forest characteristics – the influence of topography on the radar signal needs to be known. Paper 1 studies the influence of topography (via incidence angle) on the radar signal that scatters back from various forest areas.

When mapping forest biomass for large areas, large numbers of SAR scenes must be used to cover the area. Individual scenes must be mosaicked together. This can be done in two ways: SAR scenes can be mosaicked before image analysis or the results from single-scene analysis can be mosaicked after the image analysis. In this mosaicking process, various sensor-specific geometric and radiometric characteristics must be taken into account. Mosaicking of SAR data and geometric and radiometric techniques needed in mosaicking are studied in Papers 2 and 3.

Radar signals from various radars interact with the forest canopy in different ways. When mapping forest biomass, the accuracy of results depends on the type of radar data used. In Papers 4 and 5, the use of various radar wavelengths and polarisations in forest biomass mapping is studied.

Even if a radar sensor is considered accurate and efficient in forest biomass mapping, practical space-borne mapping is restricted to those radar sensors that are available on satellites in the foreseeable future. In Paper 6,

the temporal development of L-band radar signal of forests and the possibilities of using multi-temporal methods in forest biomass mapping are studied.

The following sections describe the context in which the themes mentioned above were studied. Samples of relevant literature are mentioned until the year of submission of the corresponding paper. More recent literature is cited where this is necessary for understanding the relevance of the paper today.

Interferometric techniques (*e.g.*, Pulliainen *et al.* 2003, Wagner *et al.* 2003, Shimada *et al.* 2002b, Koskinen *et al.* 2001) in forest biomass mapping have been investigated in recent years. Repeat pass interferometry poses some additional requirements on image acquisition conditions (*e.g.,* low wind). Interferometric techniques at least double the number of image acquisitions (compared to techniques that can work with backscattering amplitude data only). For these reasons, interferometric techniques are not very attractive when aiming at covering large areas with homogeneous mapping results. Interferometric techniques are left outside the scope of this thesis.

Forest biomass is a quantity that is difficult to measure. In boreal forests, the biomass is tightly coupled to forest stem volume (Häme *et al.* 1992, Kauppi *et al.* 1995, and Häme *et al.* 1997). Häme *et al.* (1992) presented an (approximate) analytical form for this relation in boreal forest:

$$B = 0.6 \cdot V \tag{1}$$

where V is forest stem volume (m³/ha) and B is dry biomass (tons/ha). Equation (1) ignores differences between species (see *e.g.* Kauppi *et al.* 1995). Equation (1) may underestimate the biomass by up to 20 percent. In the absence of large datasets of biomass measurements, forest stem volume data were converted into forest biomass using Equation (1).

Radars measure the return of a signal emitted by the radar. The strength of this signal can be expressed as a power or amplitude. The amplitude is the square root of the received power. In the following, the term backscattering amplitude is used to refer to the square root of received power. In case of SAR, the radar does not measure directly the power backscattered from a resolution unit, but the final signal is derived in a computational process called SAR processing. In SAR data, the backscattering amplitude can be defined as the square root of the power that would have been measured by a real aperture radar that has the same resolution as the SAR. The term

backscatter is used in a more general context without making assumptions on power or amplitude formats.

Table 1. SAR sensors used in Papers 1 through 6.

Sensor	Band(Wave-length in cm)	Pols.	Res. (m) /Looks	Inc. (deg)	Launch	End of Life
Seasat	L(23)	HH	25/4	23	1978-06-28	1978-10-10
JERS	L(23)	HH	18/3	39	1992-02-11	1998-10-12
AIRSAR	C(6), L(23) P(63)	Full	12/4	30-70	N/A	N/A

Table 1 lists the main characteristics of radar systems used in this thesis. The column "Pols." lists the polarisations of the sensors. AIRSAR is a fully polarimetric sensor (measuring HH, HV, VH, and VV polarisations) in all three wavelength bands. Column "Res." gives the ground resolution and the number of looks for which the resolution is given. The AIRSAR resolution is approximate. Held *et al.* (1988) report a pixel spacing of 12.1 m in azimuth and 6.67 m in slant range. Column "Inc." gives the incidence angle. This is the mid-swath incidence angle for space-borne sensors and the minimum and maximum incidence angles over flat earth for the air-borne AIRSAR sensor. A nominal incidence angle of 38 degrees is mentioned in some literature for JERS SAR. The nominal orbit elevation of 570 km and mid-swath off-nadir angle of 35° (NASDA 1988) give a mid-swath incidence angle of 38.68 degrees.

1.1   Incidence Angle Effects on Radar Backscatter in Forests

Topographic effects have been observed to influence or even dominate SAR images of forests (*e.g.* Drieman 1987). Few studies have evaluated the topographic effects on SAR images of forests in quantitative terms.

Teillet *et al.* (1985) studied terrain effects in a rugged forested study site in Canada using data from the Canadian Convair-580 SAR. This SAR operates in X- and L-bands and can record in both bands four polarisations: HH, VV, HV, and VV. The terrain topography has its influence on radar backscattering amplitude by the (local) incidence angle (θ). Terrain elevation varied between 330 and 1100 m above sea level. In a shallow mode

scene (nominal incidence angle 22°), $cos(\theta)$ accounted for 26 to 38 percent of the total variation in HH- and HV-polarisations of X- and L-bands (in forested areas). In a steep mode scene (nominal incidence angle 43°), $cos^2(\theta)$ accounted for 8 to 27 percent.

Foody (1986) studied terrain effects in an undulating study site in England. A set of 227 grass covered fields were divided into seven zones (a minimum of 30 fields per zone) to minimize the variation due to antenna gain and sensor look angle. This grass-land study is included here because early works in forested areas are so rare in the published literature. The SAR data were acquired by the Canadian Convair-580 SAR system. The polarisation was HH in both X- and L-bands. The SAR had the nominal incidence angle range 32° to 63° (aircraft altitude 5.4 km, swath width 7 km in ground range). The square of the multiple correlation coefficient (R^2) was used to measure the effect (on radar backscatter) of two variables: slope and aspect (relative to the SAR look direction). The R^2 statistic was derived from zero and first order partial correlations using the formula: $R^2_{0.12} = r^2_{01} + r^2_{02.1}(1 - r^2_{01})$ where subscript 0 was image tone and subscripts 1 and 2 slope and aspect respectively. $R^2_{0.12}$ was the proportion of variance in image tone (0) accounted for by the variables 1 and 2 both jointly and separately and r was the correlation coefficient. The proportion of variation in L-band that was explained by slope and aspect was between 3 and 30 percent, except in the two zones furthest away from the radar, where 50 and 38 percent of the total variation was accounted for by these variables. In X-band, the proportion of variation that was explained by slope and aspect was between 3 and 30 percent in all zones.

Hinse *et al.* (1988) reported a reduction between 3 and 9.5 percent in the variance of spectral signatures of land cover types (variance in backscatter amplitude within a land cover type) after terrain corrections of an air-borne C-band (Convair-580 SAR) HH-polarised scene. The land cover types were deciduous, coniferous, corn, agriculture, and combined. The variance in backscatter amplitude in the corn land cover increased slightly in the terrain corrections. The study site (in Canada) had moderate relief (elevation variation of 210 m within the study site). The corrections were based on the total incidence angle (not an explicit calculation of scattering area).

In newer remote sensing literature, Small *et al.* (2004b) reported error histograms on the estimation of backscattering coefficient γ^o as a function of DEM resolution. The backscattering coefficient γ^o is related to the more widely used backscattering coefficient σ^o by: $\gamma^o = \sigma^o/cos(\theta)$. Small *et al.*

(2004b) produced a (radiometrically normalized) γ^o mosaic of Switzerland using five ASAR (C-band) wide-swath scenes (nominal incidence angle 19° to 38°) with opposing look directions.

Goering *et al.* (1995) reported a reduction of 30 and 13 percent in pixel value variance in an ascending and descending ERS-1 SAR scene, respectively, after removal of terrain effects, which included the effect of the size of a resolution cell. The study site was a tundra site (in Alaska) with moderate relief and elevations between 410 and 490 m. The nominal incidence angle in the 1.5 km by 1.5 km study site was 23.1319° for the ascending scene and 23.1619° for the descending scene.

Bayer *et al.* (1991) reported that local incidence angle accounted for 36 percent of the total variation in forested areas and the range component of local incidence angle 33 percent in a Seasat SAR scene in a German study site. The nominal incidence angle for the Seasat SAR was 23°. The regression analysis did not include a scattering area as an independent variable. The study site had terrain slopes of up to 53 degrees. The elevation varied between 46 and 180 m.

Sun *et al.* (2000 and 2002) presented a technique for radiometric correction of terrain topography when using polarimetric SAR data. Because the resolution of an available DEM (DTED level 1) was too low for radiometric corrections the dependence of backscatter on the incidence angle was estimated from model calculations for HH- and HV-polarised L-band data separately. The local incidence angle was estimated from HH-polarised data. The incidence angle was used to correct the HV-polarised data to the nominal incidence angle of the SIR-C SAR. The terrain-corrected L-band HV-polarised data were used to derive a forest biomass model ($\sqrt[3]{B} = 8.45 + 0.67\sigma^o$). The estimates produced by this model had an r^2 value of 0.91 with the ground data in a stand-wise forest biomass dataset, where the biomass varied between 11.6 and 240 tons/ha. The RMSE (root mean square error) was 18.1 tons/ha. 28 stands were used for model development and another 28 stands for testing.

Goyal *et al.* (1999) combined the incidence angle and soil roughness into a linear correction function when mapping soil moisture in a mountainous grass-land area. They used L-band HH-polarised data from the AIRSAR sensor. Elevation in the study site (56.25 km^2) varied between 1097 and 2252 m). The nominal incidence angle in the study site varied from 38° to 54°. The use of the regression model between radar backscattering intensity, incidence angle, and soil roughness (root mean square height) reduced the variance in σ^o by 85 percent.

The power measured by a radar can be described by the radar equation (here for real aperture radar, a fully focused SAR has R^3 instead of R^4, *e.g.* Rosisch and Meadows 2004):

$$P_r = \frac{P_t G^2 \lambda^2 \sigma}{(4\pi)^3 R^4} \qquad (2)$$

where
P_r = received power,
P_t = transmitted power,
G = antenna gain,
λ = radar wavelength,
σ = radar cross-section of the target, and
R = distance between the radar and the target.

In earth observation radars, where the target is a spatially extended piece of earth's surface, the radar cross-section σ can be expressed:

$$\sigma = \sigma^o A \qquad (3)$$

where
σ^o = radar cross-section per unit surface area,
A = surface area of a resolution cell.
The term σ^o is called the backscattering coefficient.

The radar equation can be written:

$$P_r = \frac{P_t G^2 \lambda^2 \sigma^o A}{(4\pi)^3 R^4}. \qquad (4)$$

The terms by which terrain topography affects the power measured by radars are the backscattering coefficient σ^o and the area of the resolution cell A.

The incidence angle (or angle of incidence) θ is defined as the angle (in 3-dimensional space) between the propagation direction of the radar signal and the normal vector of an (assumed planar) resolution cell.

The backscattering coefficient $\sigma^o(\theta)$ of smooth targets (in terms of radar wavelength) decreases steeply with an increasing incidence angle. The backscattering coefficient of rough targets does not decrease so steeply with the increasing incidence angle (Ulaby *et al.* 1982).

The area of resolution cell A depends not only on the total incidence angle, but on its components in azimuth (along track) direction θ_a and in range (cross track) direction θ_r.
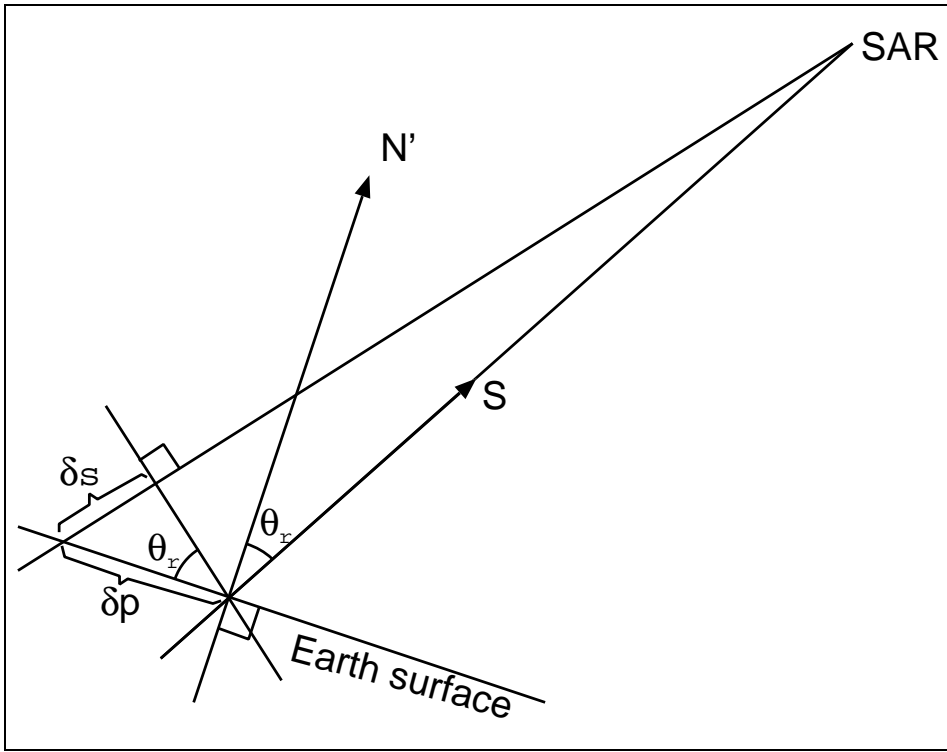
Figure 1. Dimension of a resolution cell in range direction.

Figure 1 shows a vertical cross-section plane that goes through the SAR and a pixel. N' is the orthogonal projection of the surface normal vector on the vertical plane. Angle θ_r is the angle between the vector S (pointing to the SAR) and N' in the vertical plane of Figure 1.

A space-borne SAR produces its resolution in the range direction using a pulse of finite duration (which is determined by the pulse compression technique utilized). Since the pulse length is constant, slant range resolution δ_s is constant through the image swath. As can be read in Figure 1, the range dimension δp of a resolution cell can be calculated:

$$\delta p = \frac{\delta s}{sin(\theta_r)} \qquad (5)$$

Figure 2 shows a vertical cross-section plane that goes through a pixel and is parallel to the SAR orbit. N" is the orthogonal projection of the surface normal vector on the vertical plane (of Figure 2). Angle θ_a is the angle between a vertical line and vector N" in the vertical plane of Figure 2. Angle θ_a is also the terrain slope in the orbit direction of the SAR.
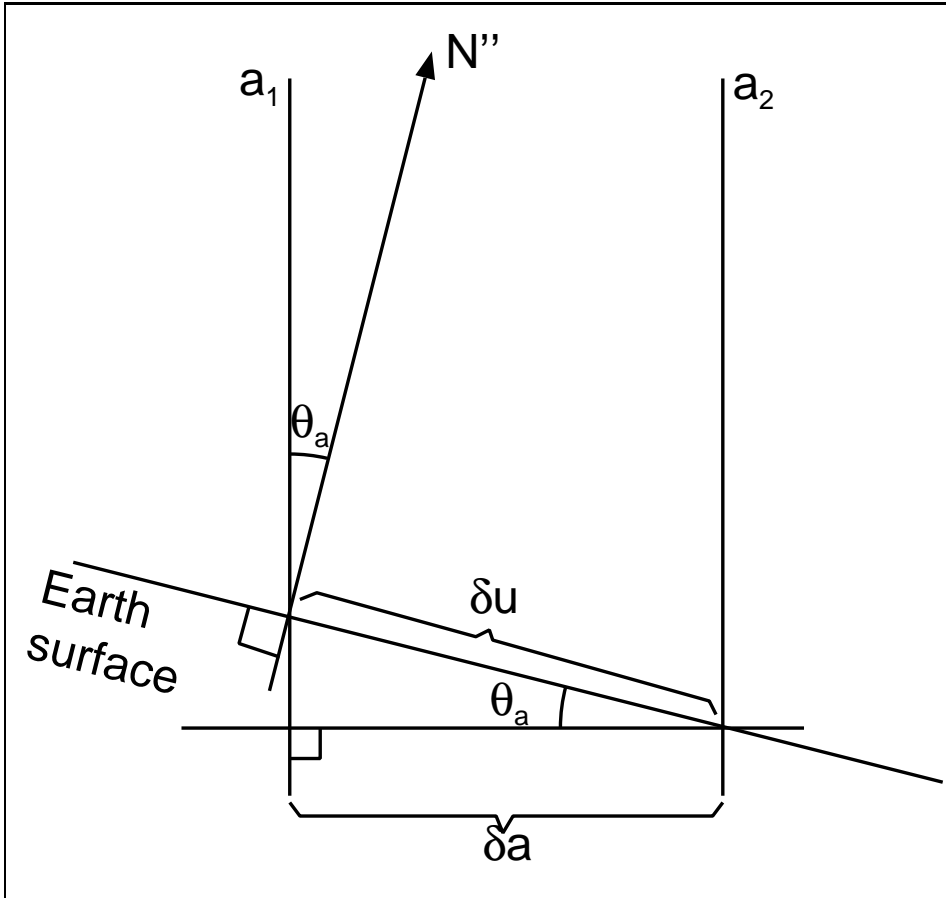
Figure 2. Dimension of a resolution cell in azimuth direction.

In a SAR scene, the azimuth resolution (on a horizontal surface) is constant through the image swath. The azimuth dimension of a (tilted) planar resolution cell is determined by two vertical planes (a_1 and a_2 in Figure 2, separated by azimuth resolution δa) that are orthogonal to the SAR orbit (unless the SAR scene has been acquired and processed in squint mode). The azimuth dimension of a tilted pixel δu can be calculated (see Figure 2):

$$\delta u = \frac{\delta a}{cos(\theta_a)} \tag{6}$$

The surface area A (in Equation 4) of a resolution cell is the product of range and azimuth dimensions:

$$A = \delta p \cdot \delta u = \frac{\delta s}{sin(\theta_r)} \frac{\delta a}{cos(\theta_a)} \tag{7}$$

In more recent literature, Ulander (1996) has presented an approach for terrain slope correction that takes into account the simultaneous effects of pixel tilting in azimuth and range directions. This approach is equal to the case where the plane of Figure 2 is not horizontal but tilted by θ_r. In this formulation, θ_a is no longer equal to the slope in the azimuth direction (unless θ_r equals zero). The angle θ_a can be defined as the angle between two planes: the vertical plane containing the sensor and the pixel (= plane 1), and the plane that contains the terrain normal vector and intersects plane 1 along the intersection of the terrain plane and plane 1. If θ_a is defined this way, Equation (7) is equal to the pixel area of Ulander (1996). As Ulander (1996) points out, the difference between these two approaches is insignificant (less than 0.01 dB) unless the terrain slope is higher than 20 degrees (and less than 0.1 dB within slopes between -40 and +40 degrees). In such high-relief landscapes lay-over seriously reduces the usefulness of SAR data regardless of terrain correction methods (unless multiple scenes with opposing look directions can be used as by Small *et al.* 2004a).

An alternative way for the backscattering coefficient σ^o is the (gamma) backscattering coefficient γ^o

$$\sigma = \gamma^o O \tag{8}$$

where
γ^o = radar cross-section per unit projected area,
O = projected area of a resolution cell.
As γ^o is directly proportional to the projected area of a resolution cell, and
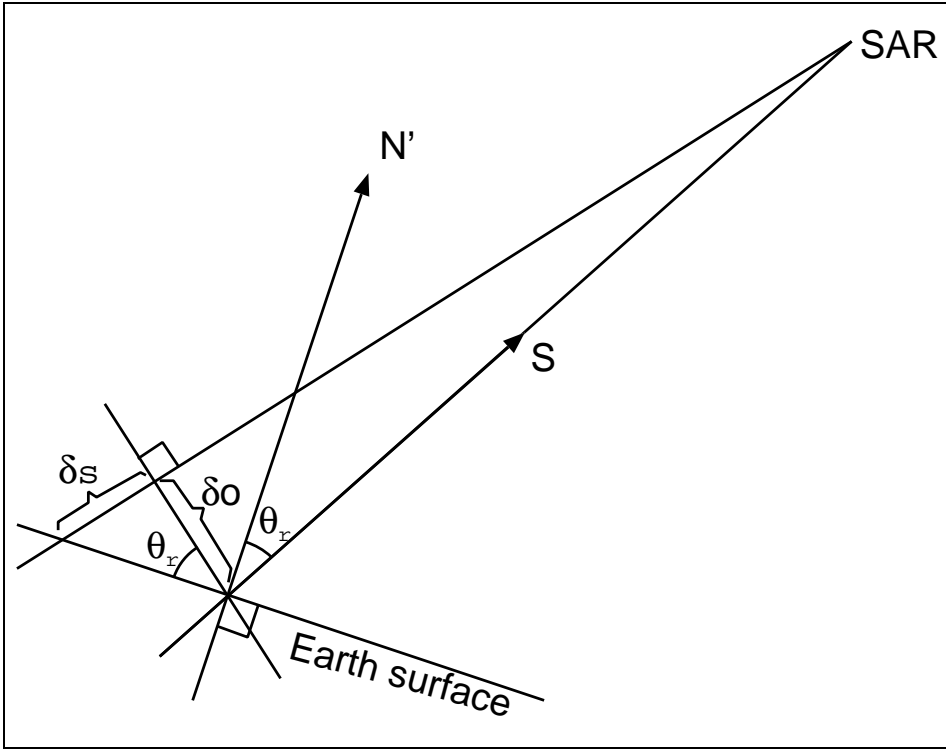
Figure 3. Projected dimension of a resolution cell in range direction.

consequently to the power intercepted by the resolution cell, the effects of terrain tilt components in range and azimuth directions are more uniform. In this alternative, the radar equation can be written:

$$P_r = \frac{P_t G^2 \lambda^2 \gamma^o O}{(4\pi)^3 R^4} \tag{9}$$

The projected resolution cell area O can be calculated (Figure 3, the same vertical plane as in Figure 1):

$$O = \delta o \cdot \delta a = \frac{\delta s \cdot \delta a}{tan(\theta_r)} \tag{10}$$

Noting that the received power must be the same in both Equations (4) and (9), the relation between σ^o and γ^o is:

$$\gamma^o = \frac{\sigma^o}{cos(\theta_r)cos(\theta_a)}. \tag{11}$$

20
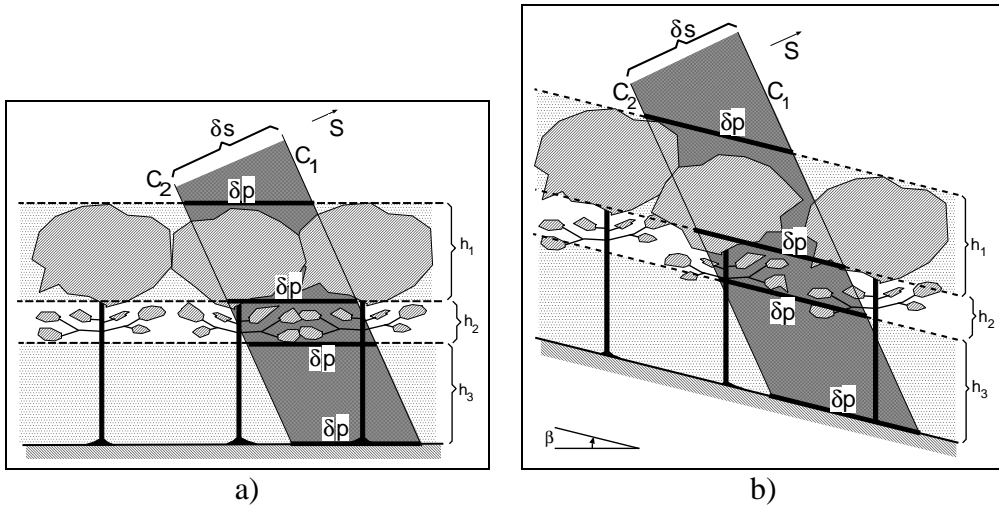
Figure 4. Resolution cell size for scattering volume. The scattering volume is proportional to the resolution surface area both with horizontal ground, a) and with sloping ground, b).

Because θ_r and θ_a are two orthogonal components of the total incidence angle θ, Equation (11) is equivalent to:

$$\gamma^o = \frac{\sigma^o}{cos(\theta)}. \tag{12}$$

Leclerc *et al.* (2001) describe in addition to σ^o and γ^o the backscatter relative to Lambertian scatterer ($\sigma^o cos^2\theta$). They used C-band HH- and VV-polarized data from the Convair-580 SAR in the so-called narrow mode (nominal incidence angles typically 45° to 76°). Slopes of up to 40° were present in the study site. After terrain correction relative to the Lambertian scatterer, forest and banana plantations could be distinguished from coffee plantations on slopes facing towards the radar.

The surface area of a resolution cell A and projected area O can be computed if a digital elevation model (DEM) is available. Small *et al.* (2004a) note that the assumption of a planar pixel has the disadvantage that it does not account for fore-shortening, lay-over, and radar shadow.

When correcting radar images for the area of resolution cell, the the same correction can be applied in areas dominated by surface scattering and those dominated by volume scattering. In most forest scattering models, the forest canopy is divided into layers of constant thickness that can be considered as homogeneous in terms of backscattering. The equidistant

21

circles (C_1 and C_2 in Figure 4, drawn as straight lines to describe the long distance to space-borne SAR sensors) that define the range resolution of a radar intersect an equal area ($\delta p \cdot \delta u$) of all boundary surfaces between the canopy layers and the ground surface. This is true for horizontal and tilted pixels (Figure 4). The size of scattering volume (the volume from which the scattering that contributes to a single resolution unit originates) is

$$V_{scat} = \delta p \cdot \delta u \cdot h \cdot cos(\beta), \tag{13}$$

where h is the vertical thickness of the layer and β (Figure 4) is the terrain slope component in range direction (*i.e.* in the cross track vertical plane). Normalisation to a constant unit scattering volume is not feasible because the balance of backscattering and absorption can vary widely in forest canopies of varying age. Normalisation to a constant unit scattering volume would also require that the thickensses of the layers within the canopy are known (or the tree heigth if the canopy is considered as a single layer). This is difficult to map with high resoltion using today's earth observation instruments. The application of the $cos(\beta)$ term in radiometric correction would require information on where the backscattering is dominated by surface scattering and where by volume scattering. This information is also difficult to map. The difference would also be small. For example for a terrain slope of 20° (36 percent slope), the $cos(\beta)$ term is 0.97 for amplitude images. The most varying term (excluding the layer thickness) in the expression of scattering volume (13) is the area of the (upper and lower) surface of the scattering layer. Radiometric correction by this term leads to a correction procedure that is identical to the corecction that is approporiate for areas dominated by surface scattering.

Similar to the surface area of volume scattering layers, the projected area of all layer boundaries is constant from boundary to boundary (Figure 5).

Backscatter modelling studies (*e.g.,* Richards *et al.* 1987, Sun and Simonett 1988) indicate that the so-called double-bounce scattering mechanism is important in L-band SAR data. This phenomenon should be visible in the angular backscatter curve $\sigma^o(\theta)$.

1.2   SAR Mosaicking Techniques

When several images are mosaicked together, the geo-location of individual scenes must fit on the image boundaries within a sub-pixel. If this is not the case, discontinuities – like rivers that do not flow continuously –
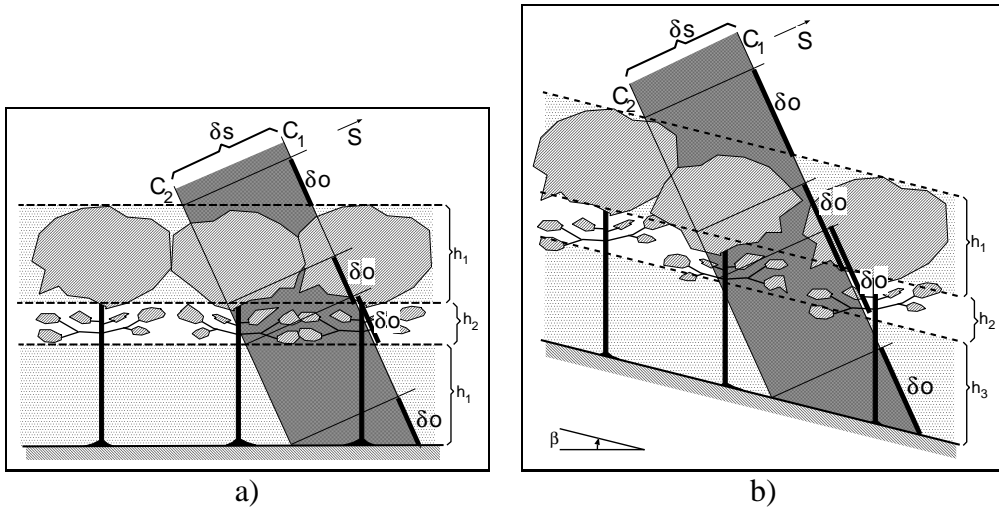
Figure 5. Projected area for volume scattering elements. The projected area of layer boundaries is constant from boundary to boundary both for horizontal ground, a) and for sloping ground, b).

occur at image seams. If a multi-temporal mosaic is compiled, the temporal components of the mosaic must also fit together within a fraction of a pixel. Otherwise mis-registration of mosaic components produces artifacts around high-contrast edges in multi-temporal image analysis techniques.

The scene radiometry must also be calibrated in such a way that no abrupt changes occur between individual scenes of the mosaic. Very sophisticated calibration methods have been developed for SAR data (*e.g.*, Menges *et al.* 2001). This approach makes a frequency table of backscatter values separately for each range co-ordinate in a SAR image. This table is then used as a look-up table in the actual calibration phase. The approach, which was applied to AIRSAR C-, L-, and P-band polarimetric dataset, assumes uniform distribution of land cover classes across image swath. The calibration method in mosaicking must be robust and free of restrictive requirements on scene contents.

The error sources of space-borne SAR data are different from those of air-borne data, and different methods are optimal for space-borne data, where the orbit information is usually more accurate. However, the orbit control and measurement accuracy of, for example, the JERS satellite was not very high. The initial (orbit-data based) geo-location accuracy of the SAR scenes was, consequently, also low. This emphasizes the need for adequate geometry revision techniques when mosaicking JERS SAR scenes.

Leberl (1975) studied mosaicking methods using a simulated set of 20 air-borne SAR strips (600 km long, 37 km wide, 63 percent sidelap). Sequential block formation with splines, followed by external interpolative adjustment, was found to be more robust and accurate than various forms of simultaneous block adjustment. The main error source in the simulation of the air-borne SAR data was the periodic error of the inertial navigation system that was used in the mosaic construction.

The GRFM (Global Rain Forest Mapping) project was launched by the Japanese space agency (NASDA) using the JERS SAR for rain forest mapping (Rosenqvist 1996). The major objectives of the project were to create spatially and temporally consistent JERS SAR image mosaics at 100-m resolution covering the entire equatorial belt and to provide these as 'ready-to-use' datasets freely and openly to the international science community and educational institutions as tools to help improve our understanding of the tropical ecosystems (Rosenqvist *et al.* 2000). In this international project, NASDA and NASA (Alaskan SAR Facility) processed raw SAR signals into image form. NASDA, JRC, and JPL produced SAR mosaics in South-East Asia, Africa, and South and Central America, respectively. The GRFM project was followed by the GBFM project. One of its main objectives was the generation of extensive, pan-boreal, SAR image mosaics to provide snap-shots of the forest, wetland, and open water status in the mid-1990'ies in the boreal forest zone of Eurasia and North America (Rosenqvist *et al.* 2004).

Rosaz *et al.* (1994) describe a methodology for using least squares adjustment in the compilation of a SAR mosaic. This technique was used when compiling a mosaic of 15 ERS-1 SAR scenes over the territory of French Guiana. Tie points between scenes were first measured manually and then refined using image correlation. SAR images of the same orbit were first combined into an image strip. A similarity transformation of the form:

$$\begin{bmatrix} x' \\ y' \end{bmatrix} = \begin{bmatrix} \cos\alpha & -\sin\alpha \\ \sin\alpha & \cos\alpha \end{bmatrix} \cdot \begin{bmatrix} x \\ y \end{bmatrix} + \begin{bmatrix} T_x \\ T_y \end{bmatrix} \tag{14}$$

was determined between two neighbouring strips. This was done using tie points and a least squares adjustment. One of the two strips was re-sampled to the geometry of the other strip using the parameters (rotation α and translations T_x and T_y in x and y) of the similarity transformation. The pair-wise combination of strips was repeated until all strips were combined into a mosaic.

Rosaz *et al.* (1994) made the mosaic compilation in a co-ordinate system

that was aligned with the azimuth-range (line-column) co-ordinate system of one of the image strips. In this approach, the need for the rotation angle α comes from the difference of the orbit heading of the reference scene and the orbit heading of the other scene where the latter heading is taken with respect to the meridian of the reference scene. The expected value of α is a non-zero function of scene latitude and depends on the imaging geometry of the (ERS-1) SAR sensor.

Rosaz *et al.* (1994) also normalized image radiometry in a pair-wise manner. One scene was modified on the basis of a transformation determined by a least squares estimation over a set of points in the overlap area between the two scenes.

Siqueira *et al.* (2000) presented a geometry revision methodology, which was also based on similarity transformation. The methodology was applied to the South-American JERS SAR dataset of the GRFM project. In this methodology, the transformation parameters were determined in a global least squares adjustment comprising all scenes in the mosaic, which included one acquisition layer. This methodology treats ground control points like adding a single, pan-continental scene that is not allowed to undergo any transformation (regarded as a "truth scene"). This treatment disturbs the structure of the normal equation coefficient matrix by adding an extended row and column since the "truth scene" has common elements with a large number of other scenes in the mosaic.

Shimada and Isoguchi (2002) presented a methodology for mosaicking long JERS SAR scenes (over 1000 km long path images) produced by the so-called Sigma-SAR processor. As the sensor yaw angle is known with high accuracy, this methodology uses only translations to make neighbouring scenes fit. Ground control points and an affine transformation are used to prevent error propagation due to path integration.

Shimada and Isoguchi (2002) used second-degree polynomials to normalize the range dependency of backscatter. Additional gain correction was determined on the basis of points in overlap areas between scenes and a least squares estimation.

Hutton *et al.* (2000) compiled a Radarsat-1 mosaic of Canada. Over 100 image strips (4 to 7 scenes each, 300 km by 300 km scenes, scanSAR narrow B beam mode, 50 m resolution) were mosaicked using approximately 3000 ground control points measured from 1:50 000 and 1:250 000 topographic maps. Radiometric balancing within image strips was performed when necessary. An algorithm was designed to automatically calculate ra-

diometric variations across a scene and to produce more consistent gray values in the output image. The global elevation model GTOPO30 was used in ortho-rectification. The output mosaic was produced in Lambert's conformal conical map projection with a pixel spacing of 250 m.

Noltimier *et al.* (1999) compiled a Radarsat-1 mosaic of Antarctica. The mosaic consisted of approximately 4000 Radarsat images acquired in standard beam modes 2 to 7 and extended high beam 4. The scenes, which had a ground resolution of 25 m, covered an area of 100 km by 100 km. The mosaic was constructed in blocks consisting of approximately 150 scenes. Ground control points, tie points (between image swaths), and satellite ephemeris data were used in block adjustment. A digital elevation model was used to ortho-rectify images. The ensemble of ortho-rectified images was radiometrically balanced to remove seams and other artifacts. Individual blocks were combined in the final processing stages including block to block balancing and grand geometric correction.

In Siberia project (Wagner *et al.* 2003), mosaicking was done after (interferometric) image analysis. ERS scenes acquired at the same track-frame co-ordinates were co-registered by cross-correlation. JERS scenes were co-registered to ERS-frames. A total of 122 ERS-JERS "stacks" were then mosaicked to a larger coverage after image analysis.

1.3 Radar Wavelength and Polarisation in Forest Biomass Mapping

The interaction between the electromagnetic radiation of a radar signal and components of forest canopy and forest floor depend strongly on the wavelength and polarisation of the radar (*e.g.*, Ulaby *et al.* 1982).

The electric field of a radar pulse oscillates in two dimensions that are orthogonal to each other and to the propagation direction of the radar pulse. These oscillations have a constant phase difference in such a way that the electric field vector draws an ellipse on the plane perpendicular to the propagation direction (Figure 6). The polarisation of the pulse can be described by two angles: the orientation angle ψ between the vertical and the semi-major axis of the ellipse and the ellipticity angle χ (van Zyl *et al.* 1987). The ellipticity angle χ is the angle between two end points of the semi-minor axis of the ellipse seen from the end point of the major axis (Figure 6).
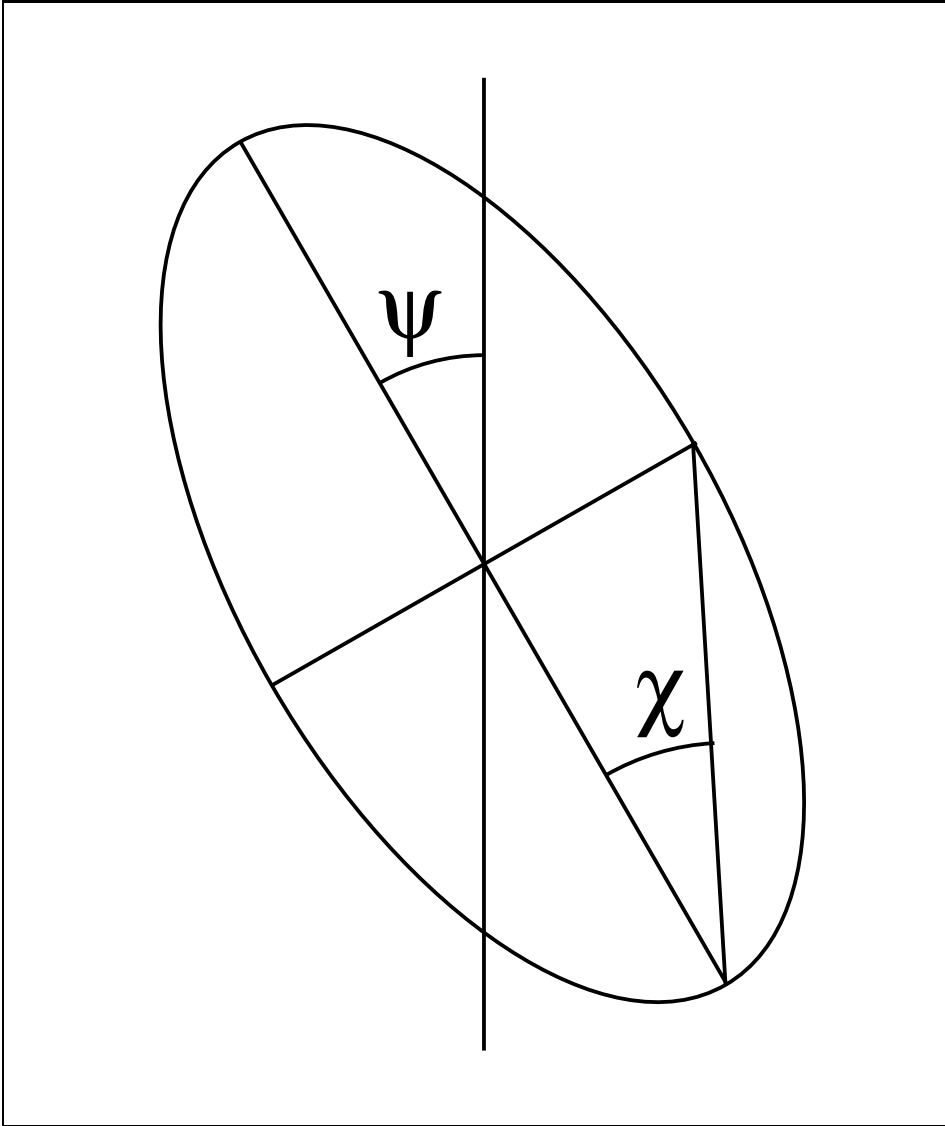
Figure 6. Orientation and ellipticity angles of an electromagnetic radar pulse on a plane orthogonal to the propagation direction of the pulse.

The ellipticity angle χ varies between -45° and 45°. The orientation angle ψ varies between -90° and 90°. An ellipticity angle of 0° produces a linear polarisation (where the electric field oscillates in one dimension only) and χ of 45° (or -45°) produces a circular polarisation.

Sader (1987) studied L-band SAR polarimetric data in forest biomass mapping. The sensor was a JPL-developed predecessor of the AIRSAR sensor (nominal incidence angle 15° to 60°), which was operated on a Convair 990 aircraft. A correlation coefficient of 0.76 was obtained in a dataset of nine forest stands between the biomass and HV-polarisation digital number. The HH- and VV-polarisations were not significantly correlated with biomass. The stands included two pine species: longleaf pine (*Pinus palustris* Mill.) and slash pine (*Pinus elliotti* Englem.) in a relatively flat study site (elevation 3 to 15 m). The green weight biomass varied from 25 to 230 tons/ha.

Hussin *et al.* (1991) also studied slash pine biomass and L-band polarimetric SAR data. The sensor was the JPL-developed polarimetric L-band SAR before the AIRSAR sensor (on-board a Convair 990 aircraft). A coefficient of determination (R^2) of 0.97 was obtained between HV-polarised SAR data and biomass data that had been transformed by the Box-Cox power transformation. The dataset contained 35 stands with an age of between 4 and 31 years. The biomass varied between 35 and 428 tons/ha.

Le Toan *et al.* (1991) studied forest biomass with AIRSAR multi-band polarimetric radar. High correlations (R^2 values of 0.95, 0.90, and 0.88) were obtained between stem biomass and P-band data in VH-, HH-, and VV-polarisations. The study site was on flat soil. The stem biomass varied between 0 and 105 tons/ha and stand age between 0 and 42 years. Tree species was mainly maritime pine (*Pinus pinaster* (Ait.)). The dataset consisted of 24 forest stands and 9 clear-cut stands.

In more recent literature, Hoekman and Quinones (1998 and 2000) studied AIRSAR data in forest biomass mapping in a tropical study site in Colombia. The ground data set consisted of 13 plots of primary forest, 10 plots of secondary forest, and 5 plots of grassland with bushes. The size of primary and secondary forest plots was 1000 m^2. The biomass varied between a few tons/ha and 315 tons/ha. The non-linear regression model (3 parameters) was between the logarithm of γ^o (dependent variable) and the exponential of the logarithm of biomass. C-band produced the lowest coefficient of determination, followed by L-band, and P-band, which produced the highest. In both L- and P-bands, the HV-polarisation produced the highest R^2 values (0.93 and 0.94). Hoekman and Quinones (2000, p.

693) note that the biomass map is useful for land and forest degradation assessment. The biomass map is of limited value for foresters who want to assess parameters such as timber volume.

Ranson and Sun (1994) studied forest biomass mapping in a study site in Maine, USA using AIRSAR data. The elevation varied only within 68 m. The ground dataset consisted of 39 stands with above-ground dry biomass between 0 and 350 tons/ha. The natural forest stands consisted of mixtures of hemlock-spruce-fir, hemlock-hardwoods and hardwood stands (mixtures of aspen, birch, maple and beech). Ranson and Sun (1994) used only HV-polarised data because earlier studies suggested HV-polarisation to be most correlated with forest biomass. In linear regression between the logarithm of biomass and backscatter, P-band produced an R^2 value of 0.81 and L-band 0.75. Using the band ratios P/C and L/C improved the R^2 values slightly.

Saatchi and Moghaddam (2000) used an AIRSAR mosaic (C-, L-, and P-bands, all in HH-, HV-, and VV-polarisations) for forest biomass mapping in a boreal study site in Canada. Elevation in the study site was between 550 and 730 m. The method started with estimating (using an iterative non-linear least squares estimation method) the parameters for a semi-empirical forest backscatter model for four homogeneous stands of trembling aspen, old jack pine, old black spruce, and young jack pine. The parameters included crown moisture content, stem moisture content, rms height of (ground) surface roughness, surface reflectivity (a function of soil moisture), and 11 attenuation or scattering cross-section coefficients. The crown and stem moisture content were used to estimate the crown and stem biomass (by a conversion factor). The method required at least seven independent radar measurements that were sensitive to these parameters. This condition was met in the AIRSAR polarimetric 3-band dataset. When applying the method in forest biomass estimation, a land cover map was included. For mixed stands, a separate set of structural model parameters was computed. A dataset of 18 stands (with biomass between 7.42 and 153.52 tons/ha) was used to evaluate the accuracy of forest biomass mapping. The total biomass mapping accuracy was 91 percent for a set of P-, L-, and C-bands (P-HH, P-HV, L-HV, and C-HV). The accuracies for polarimetric (HH-, HV-, and VV-polarised data) P-band and L-band datasets were 92 percent and 86 percent, respectively.

Balzter *et al.* (2002) studied forest biomass mapping in a Finnish study site using polarimetric EMISAR (C- and L-band) data. Landsat-derived forest inventory data were used as surrogate ground data. The most com-

mon tree species were pine (*Pinus sylvestris* L.), spruce (*Picea abies* L.), and birch (*Betula spp.*). The average forest stem volume was 50.5 m^3/ha (variation 0–140 m^3/ha). Pixel values averaged over 100 m by 100m pixels (20 by 20 averaging) were used as observations instead of the usual stand-wise data (about 410 observations). Single-band regression models – exponential in stem volume – produced correlation coefficients of 0.54 and 0.63 in L-band HH- and L-band HV-polarisations, respectively, (0.26, 0.55, and 0.57 in C-band HH-, HV- and VV-polarisations, respectively) between the estimated and measured stem volume.

Castel *et al.* (2001) studied forest stem volume mapping in a French study site using ERS (C-band VV-polarisation, 23° incidence angle), JERS (L-band HH-polarisation, 39° incidence angle), and SIR-C (C- and L-bands, HH- and HV-polarisations, 55° incidence angle) data. The ground dataset consisted of 58 stands (over 2 ha) of Austrian pine (*Pinus nigra nigricans*). The elevation was between 1600 and 1200 m. There were slopes of up to 45°. The stem volume varied between 0 and 700 m^3/ha. Terrain topography effects were corrected using a facet-based method. The terrain corrected σ^o was further modelled and corrected as a function of incidence angle (θ). Linear regression between the logarithm of the backscattering coefficient σ^o and the logarithm of the stem volume was employed. Summer acquisition of SIR-C data produced the highest coefficient of determination (R^2 values of 0.80, 0.71, 0.46, and 0.32 in L-HV, L-HH, C-HV, and C-HH, respectively), followed by JERS (R^2 values of 0.58) and ERS (R^2 values of 0.01).

Santos *et al.* (2001 and 2003) studied air-borne (AeroSensing) P-band SAR data for forest biomass mapping in a tropical study site in Brazilian Amazon. The data set included 17 (2001) and 18 plots (2003). The six primary forest plots measured 10 m x 250 m. The twelve regrowth plots measured 10 m by 100 m. Characteristic species in primary forest included *Carapa guianensis* Aubl., *Eschweilera odorata* (Poepp) Miers, *Syzygiopsis oppositifolia* Ducke, *Trattinickia rhoifolia*, *Tachigalia myrmecophylla* Ducke, *Coumarouma odorata* Aubl., and *Nectandra mollis* Nees. The most common species in regrowth areas were *Tapirira guianensis* Aubl., *Cecropia* spp., *Vismia guianensis* (Aubl) Choisy, *Guatteria poppigiana* Mart., *Didymopanax morototoni* Aubl., *Inga alba* (Sw) Willd., *Murcia bracteata* (Rich) D.C. The biomass was between 8.00 and 271.82 tons/ha. The regression model was logarithmic in biomass. R^2 values of 0.62, 0.65, and 0.47 were obtained for HH-, HV-, and VV-polarisations, respectively (Santos *et al.* 2001). HV-polarisation had the highest dynamic range, (Santos *et al.* 2003). Multiple (HH, HV, and VV) regression did not increase the signif-

icance of R^2 values compared to those obtained with HH- or HV- single-polarisation data.

Israelsson *et al.* (1997) studied CARABAS VHF SAR in forest biomass mapping. The CARABAS operated in the frequency range 20–90 MHz (wavelength 3–15 m) with HH-polarisation. The study site (in Öland, Sweden) was dominated by oak (*Quercus robur*), birch (*Betula sp.*), and alder (*Alnus Glutinosa*). In a dataset of 12 stands (2–12 ha), the forest stem volume varied between 0 and 210 m^3/ha. Incidence angle was between 60° and 65°. The study site had no variation in elevation. Israelsson *et al.* (1997) found that the backscattering coefficient increases with increasing stem volume without saturation in the stem volume range 0–200 m^3/ha.

Smith and Ulander (1998 and 2000) studied CARABAS data for forest biomass mapping in a study site in Finland (Tuusula). Dominant tree species were Scots pine (*Pinus sylvestris*) and Norway spruce (*Picea abies*) with some deciduous trees (most common birch, *Betula pendula*). The study site was generally flat. The dataset included about 140 stands (Smith and Ulander 1998) with size varying between 0.1 and 6 ha. Forest stem volume varied from close to zero to 550 m^3/ha. Disturbing non-forest objects (like power lines, buildings, and fences) were manually excluded from the dataset. In two scenes with incidence angles of 64° and 53°, R^2 values of 0.66 and 0.64 were obtained between the logarithm of σ^o and stem volume (Smith and Ulander 1998). Smith and Ulander (2000) used a regression model of the form $log_{10}(s^o) = c + m \cdot log_{10}(V)$ where s^o is backscattering amplitude and V forest stem volume. The model was determined from a set of 112 stands with stem volume higher than 100 m^3/ha. The inverted model was used to compute stem volume for the stands used. The correlation coefficient between the estimated and measured forest stem volume was 0.82 and 0.81 for the scene with 64° and 53°, respectively. The corresponding RMSE were 89 and 84 m^3/ha.

Fransson *et al.* (2000) studied CARABAS data in forest biomass mapping in a boreal coniferous study site (Tönnershöjden) in southern Sweden. The prevailing tree species were Norway spruce (*Picea abies*) with some Scots pine (*Pinus sylvestris*) and some deciduous species including beech (*Fagus sylvatica*). Elevation varied between 55 and 140 m. Forest stands on relatively flat terrain, larger than 2 ha, and more than 70 percent Norway spruce were selected for analysis. The data set was limited to stands with stem volume 80 m^3/ha or more (average 339 m^3/ha, highest 725 m^3/ha). The 80 m^3/ha limit was applied to avoid problems due to the noise floor of the CARABAS sensor. Disturbing non-forest ob-

jects (like power lines, buildings, and fences) were manually excluded from the dataset. Stands with terrain slope higher than 4° were also excluded. Fransson *et al.* (2000) obtained a correlation coefficient of 0.83 between stem volume and backscattering amplitude in a dataset of 201 stands. In a more limited, objectively inventoried dataset of 30 stands, an R^2 of 0.88 was obtained between the square of stem volume and backscattering co-efficient (σ^o). No saturation was observed in either of these datasets.

The sensitivity to environmental factors varies from radar bands to others. Dobson *et al.* (1991) observed that a rain shower had the strongest effect (in a C-, L-, and P-band AIRSAR dataset) on C-band and the weakest effect on the P-band.

The stability of the relation of radar backscatter with forest biomass and environmental factors has been studied among others by Villasenor *et al.* (1993), Ahern *et al.* (1993), Keil *et al.* (1994), Conway & Estreguil (1994), Ranson *et al.* (1995), Quegan *et al.* (2000), Ulander *et al.* (2000), Angelis *et al.* (2001), and Askne *et al.* (2003).

Villasenor *et al.* (1993) studied ERS-1 SAR data (C-band, VV-polarisation, incidence angle 23°) from the commissioning phase of the ERS-1 satellite (the same orbit repeated every 3 days) in a tundra site in Alaska, USA. The elevation in the study site varied typically between 430 and 730 m with some mountains up to 1220 m. Backscatter ratio from scene to scene was used to study the changes in backscatter. The freezing between images acquired on 26 and 29 September caused a drop of backscatter. This drop was over 4 dB higher in dryer, coarse textured soils on upper slopes than on lower, finer textured soils on a flood plain.

Ahern *et al.* (1993) studied HH-polarised data from the Canadian C-band SAR (on-board a Convair-580 aircraft) in a forested study site in Canada. The study site had low relief (generally less than 25 m). The dataset covered 18 forest areas dominated by black spruce (*Picea mariana*), white spruce (*Picea glauca* Voss.), jack pine (*Pinus banksiana* Lamb.), red pine (*Pinus resinosa* Ait.), white pine (*Pinus strobus* L.), tamarack (*Larix laricina*) and some deciduous species. In addition, the dataset included six clear-cut areas. No biomass or stem volume data were reported in Ahern *et al.* (1993) but the age varied between 32 and 100 years, height between 12 and 27 m and diameter at breast height between 12 and 36 cm in the forest areas. Canopy closure was high. The radar dataset of four acquisitions (August, October, February, and May) was not absolutely calibrated but the scenes were scaled to a common mean backscatter value. The dynamic range in the forested areas was highest in May (6 dB) and lowest

in February (3.5 db, temperature -4°, 46 cm of snow in forest). The range of backscatter from open forest land was large. The separation between forested and clear-cut areas was highest in February.

Conway & Estreguil (1994) studied a set of 21 ERS-1 SAR scenes in a tropical study site in Papua New Guinea. The study site was almost flat. Dense evergreen forest had a very stable backscattering coefficient varying less than 1 dB within the year. The backscattering coefficient of savannah varied by 4.5 dB. The contrast between forest and savannah was typically 4 dB in scenes acquired in the dry season and about 1 dB in scenes acquired in the rainy season.

Keil *et al.* (1994) studied four ERS-1 SAR scenes in a tropical study site in Brazil. They also observed that the contrast between rainforest and deforested areas was higher in the scenes that were more within the dry season.

Ranson *et al.* (1995) studied HV-polarised L- and C-band data from the Shuttle imaging radar SIR-C. The topography of the study site was gentle with elevations between 550 and 730 m. The dataset of 13 stands was dominated by jack pine (*Pinus banksiana*) with one spruce stand and one stand of mixture of jack pine and aspen (*Populus tremuloides*). The biomass varied between 6 and 251 tons/ha. Ranson *et al.* (1995) derived two regression models between the logarithm of L-band HV-polarised backscattering coefficient and the forest biomass for scenes acquired on 10 April, 1994 and 1 October, 1994. The April scene was acquired with air temperature around 4° C (after a night with -4°), but the soil (at the depth of 10 cm) still frozen. The October temperature was around +3° both in day and the preceding night, with 1 mm of rain during the 24 hours before the image acquisition. The biomass functions were:

$$y = 5.130 + 0.240x \tag{15}$$

for the April scene and

$$y = 4.540 + 0.201x \tag{16}$$

for the October scene. Here y = logarithm of forest biomass (kg/m^2) and x = backscattering coefficient (dB). The coefficient of determination was 0.863 for the April scene and 0.846 for the October scene. When evaluated at a backscattering coefficient of -20 dB, the April and October functions produce biomass estimates of 21 and 33 tons/ha, respectively. At -16 dB, they produce estimates of 195 and 210 tons/ha.

Quegan *et al.* (2000) studied ERS 1 and 2 data in an English site dominated by Corsican pine using a dataset of 20 SAR scenes. No data on

stem volume or biomass was available, but forest age was used as a variable correlated with biomass. The study site was flat. The soil was porous and dry and contained flints, sand, and chalk. The mean backscatter of Corsican pine first decreased with age, reached then its lowest level around 15–20 years, and then increased to a saturation level around -9 to -10 dB. The decline in backscattering with age (or biomass) arised from increased attenuation. The backscatter level and the slope of the curve depended strongly on ground return, which was time and site dependent. Quegan *et al.* (2000) studied the temporal stability of young forest, old forest, and non-forest areas. Young forest (2–5 years) changed by 7 dB over the year while old forest (13–60 years) changed by 2.5 dB. Non-forest (agricultural) areas changed by at least 5 dB. Quegan *et al.* (2000) used this difference in variability to map mature forest areas. They note that in boreal regions the times of freezing or snow must be excluded because these conditions cause marked changes in the forest backscatter.

Ulander *et al.* (2000) studied the VHF (20–80 MHz) radar CARABAS in a site (Tönnersöhede) in south-western Sweden. The site was dominated by Norway spruce (*Picea Abies*) and had a modest topography with elevations between 55 and 145 m. The backscatter amplitude remained stable over a period of 20 months. Linear regression analysis between the stand-wise averaged backscatter amplitude data from two acquisitions produced a coefficient of determination of 0.91. Ulander *et al.* (2000) also derived regression models between forest stem volume and CARABAS backscatter amplitude in five study sites dominated by conifers in Sweden, Finland, and France. The coefficient of determination in these regression analyses varied between 0.64 and 0.97. The differences in the regression coefficients between sites were due to differences in the ground reflection coefficient.

Angelis *et al.* (2001) studied a set of three ERS-1 scenes (acquired in July 1992, September 1993, and April 1996) in a tropical study site in Brazilian Amazonia. The first two scenes were normalized to the mean backscatter of the last scene. Forests with selective logging had higher backscatter than other forests, forests affected by fire had lower backscatter than other forests, and the undisturbed forest had a stable backscatter.

Askne *et al.* (2003 and 2004) studied JERS and ERS SAR data in forest stem volume mapping in a Swedish study site (Kättöle) dominated by Scots pine (*Pinus sylvestris*) and Norway spruce (*Picea abies*) with some deciduous trees like birch (*Betula pendula*). The topography of the site was relatively flat with elevations between 75 and 110 m. Forest stem

volume data from 42 stands (2–14 ha) varied between 8 and 335 m^3/ha (mean 135 m^3/ha). The ERS dataset consisted of nine tandem pairs (18 scenes) between ERS-1 and ERS-2 from the so called tandem phase (1-day difference between ERS-1 and ERS-2 acquisitions). The JERS dataset included nine scenes. Only one JERS coherence scene (between acquisitions on 15 April and 29 May, 1997) had high enough coherence values to use. Askne *et al.* (2003) found that the ERS backscatter for different acquisitions varied inconsistently from one image to another. Correlation coefficient (against forest stem volume) was typically less than 0.3. The coherence was more consistent and produced correlation coefficients higher than 0.6 in most cases. The RMSE (corrected for ground data sampling error) in forest stem volume mapping with the nine tandem coherence scenes varied between 20.9 and 151.5 m^3/ha. In JERS SAR backscatter data, the correlation coefficient with forest stem volume was generally of the order of 0.8. The (corrected) RMSE values in forest stem volume mapping using JERS backscatter data varied between 36.5 and 140.1 m^3/ha. The multitemporal stem volume mapping using three best JERS backscatter observations and one coherence observation produced (corrected) RMSE values of 27.2 and 38.0 m^3/ha depending on which half of the ground data was used as training and testing set. Using all nine backscatter observations, the RMSE was 36.4 or 59.0 m^3/ha. Askne *et al.* (2004) also made a multiple regression model of the backscatter estimation models of the three best JERS SAR scenes and the coherence estimation model, which produced a correlation coefficient of 0.91 between the estimated and measured stem volume. The use of the four best ERS coherence images (out of the nine pairs acquired) produced a (corrected) RMSE value of 10.0 m^3/ha. In the multitemporal estimation cases, each scene was weighted by its scene-specific RMSE value.

Change detection in forested areas using SAR data has been studied among others by Rignot & van Zyl (1993) and Kuntz *et al.* (1999).

Rignot & van Zyl (1993) studied ERS SAR data in two Alaskan sites. Compared to difference between acquisitions, the ratio between acquisitions had the benefit that the detection probability was independent of backscatter level. Rignot & van Zyl (1993) also used temporal decorrelation of speckle. As the decorrelation of speckle helped to detect changes in the position of scatterers the ratio method provided information about the magnitude of the observed changes. Rignot & van Zyl (1993) recommended that both methods should be used in detailed monitoring studies.

Kuntz *et al.* (1999) used colour composites of texture filtered and speckle reduced Radarsat and JERS SAR scenes in mapping clear-cutting, plantation, and shifting cultivation in a tropical rainforest in Kalimantan, Indonesia. Visual interpretation was done after geo-coding in a GIS system. The problems in separating clear-cutting, plantation, and shifting cultivation in undulating terrain could be overcome by using timeseries of images or by using image pairs acquired from ascending and descending orbits at almost the same time. The L-band JERS SAR data discriminated areas of recent clear-cuts and initial regrowth on plantations better than ERS or Radarsat (C-band) data.

1.4 Multi-Temporal L-Band Radar Backscatter in Forest Biomass Mapping

Boreal forest biomass mapping using L-band SAR data has been studied by, among others, Harrell *et al.* (1995), Fransson and Israelsson (1999), and Pulliainen *et al.* (1999). For further references, see the introduction of Paper 6.

Harrell *et al.* (1995) studied JERS SAR data for forest biomass mapping in Alaska in a study area of 14 sites with a minimum size of 25 ha. Dominant tree species were black spruce (*Picea mariana*) and white spruce (*Picea glauca*). The sites were selected avoiding extreme relief. The total biomass ranged between 0.7 and 5.6 kg/m^2. This corresponds to about 12 to 93 m^3/ha (Equation 1). Harrell *et al.* (1995) obtained an R^2 value of 0.40 (14 sites) between the logarithm of total biomass and logarithm of backscattered power in a mosaic acquired in July-August 1992. When recently burned sites were excluded R^2 rose to 0.66 (11 sites).

Fransson and Israelsson (1999) studied JERS SAR data for forest biomass mapping in north-eastern Sweden in a study site of 59 stands. The dominant tree species were Scots pine (*Pinus sylvestris*), Norway spruce (*Picea abies*), and birch (*Betula pendula* and *Betula pubescens*). Elevation varied between 30 and 310 m. The stem volume varied between 0 and 285 m^3/ha. Fransson and Israelsson (1999) obtained R^2 value of 0.57 between the exponential of stem volume and backscattering coefficient σ^o in a scene acquired in June 1992. In a subset of 37 stands (overlap with other scenes), R^2 rose to 0.60. Fransson and Israelsson (1999) also obtained R^2 values of 0.57 an 0.56 in scenes acquired in December 1992 and May 1994, respectively. The regression lines of the December and June scenes

were around 2 dB lower than the one of the May scene. Fransson and Is-raelsson (1999) also determined the saturation level of the backscatter *vs.* forest volume relation. The method used the backscattering coefficients of mature forest and ground, the slope of the backscattering coefficient *vs.* stem volume ($\partial \sigma^o / \partial V$), and the attenuation coefficient κ. The saturation level was at 136, 130, and 157 m^3/ha for JERS SAR scenes acquired in June 1992, December 1993, and May 1994, respectively.

Pulliainen *et al.* (1999) studied multi-temporal JERS SAR data in a boreal study site in southern Finland. The dominant tree species was Norway spruce (*Picea abies*). Ground data on stem volume was computed from a Landsat-derived forest inventory map and aggregated to six stem-volume classes between 25 and 260 m^3/ha. The scenes were acquired in December 1994, March 1995, April 1995, and May 1993. The backscatter level in frozen conditions was around 2 dB lower than in non-frozen conditions.

In more recent literature, Santos *et al.* (2002) studied biomass mapping with JERS SAR data in two tropical study sites in Brazil. Santos *et al.* (2002) used regression models (logarithm of biomass and a sigmoid function) to model L-band backscatter using a ground data set of 68 plots (2500 m^2 in primary forest, 1000 m^2 in secondary forest). They found that the sigmoid function has a high sensitivity below (above ground) biomass values of 60 tons/ha, where the backscattering coefficient (σ^o) saturates at about -7.45 dB.

Pierce *et al.* (2003) mapped re-growth biomass in two Brazilian (tropical) study sites using a combination of JERS and Radarsat wide-swath SAR data. The radar data were ortho-rectifed using a digital elevation model (DEM). The local incidence angle was also computed and used to calibrate the SAR data to account for the ground area illuminated. The logarithm of biomass was modelled as a linear combination of L- and C-band data. An R^2 value of 0.92 was obtained in a set of 15 ground plots of 10 m by 50 m. The biomass varied between 8 and 160 tons/ha.

Kuplich and Curran (1999) mapped forest biomass in a Brazilian study site using a time-series of ten JERS SAR scenes. The biomass was between 8 and 104 tons/ha for 15 regenerating plots and about 370 tons/ha for three primary forest plots. The size of plots was 10 m by 50 m (Luckman *et al.* 1997). A correlation coefficient of 0.67 (based on 18 plots) was obtained between the logarithm of above-ground biomass and the logarithm of the backscattering coefficient. The biomass-backscatter relation saturated at around 60 tons/ha.

Castel *et al.* (2000 and 2002) studied biomass mapping in Venezuela using a mosaic of six JERS SAR scenes. The stem volume varied between 0 and 200 m^3/ha in a dataset of 78 (76 in 2002) stands of Caribbean pine (*Pinus caribaea var. Hondurensis*) plantations. Using a semi-empirical forest backscattering model, a correlation coefficient of 0.85 (Castel *et al.* 2000) was obtained between the estimated and measured stem volume (0.92 in Castel *et al.* 2002).

Tsolomon *et al.* (2002) studied a site in Mongolia. Elevation varied between 1100 and 1600 m. They derived regression models between biomass (dependent variable) and the backscattering coefficient (independent variable) from JERS SAR data. The form of the regression model was a quadratic polynomial. Tsolomon *et al.* (2002) obtained R^2 values of 0.55, 0.68, and 0.72 for larch (10 to 30 tons/ha, *Larix sibirica*), pine (15 to 25 tons/ha, *Pinus sibirica*), and poplar (3 to 6 tons/ha, *Populas*) stands, respectively. The data set consisted of one scene and ground data for approximately 25 stands per species.

Kellndorfer and Ulaby (2003) studied JERS and ERS SAR data for biomass mapping in a boreal study site with 17 jack pine (*Pinus banksiana*) stands. The biomass varied between 1 and 90 tons/ha. R^2 values of 0.93 and 0.80 were obtained for JERS and ERS SAR data, respectively, between logarithm of biomass and logarithm of σ^o.

Askne *et al.* (2004) studied forest stem volume mapping with JERS SAR data in a boreal study site in Sweden (Kättböle). The data set included 42 stands between 2 and 14 ha in size. Elevation varied between 75 and 110 m. The dominant tree species were Scots pine (*Pinus sylvestris*) and Norway spruce (*Picea abies*) with some deciduous trees (most common birch, *Betula pendula*). The highest stem volume was 350 m^3/ha and the mean 135 m^3/ha. The backscatter model was exponential in stem volume. Askne *et al.* (2004) obtained stem volume estimation errors (RMSE, corrected for errors in *in situ* data) that varied between 36.5 m^3/ha and 85.4 m^3/ha in nine scenes. Askne *et al.* (2004) found only one interferometric pair (in a dataset of nine scenes) to be useful for stem volume estimation. Askne *et al.* (2004) made a multiple regression model of the backscatter estimation models of the three best scenes and the coherence estimation model, which produced a correlation coefficient of 0.91 between the estimated and measured stem volume.

Santoro *et al.* (2004) studied forest stem volume mapping with JERS SAR data in a boreal study site in Russia near the city Krasnoyarsk. The dominant tree species were spruce (*Picea sibirica*), fir (*Larix dahurica* and *Larix*

sibirica), and birch (*Betula spp*). The study site consisted of four compartments. In one compartment, elevation varied between 220 and 260 m, whereas other compartments had an elevation variation of several hundred metres. SAR backscatter data were corrected for topographic effects using the GTOPO30 elevation model (resolution about 800 m). The terrain correction did not produce significant improvements in stem volume estimation. Forest stem volume varied between 5 and 470 m^3/ha in the study site. In the subset (used in analysis) of stands of 8 ha or larger, the stem volume varied between 5 and 410 m^3/ha. The backscatter model was exponential in stem volume. One third of the data was used for determination of the coefficients of the backscatter model and two thirds for validation. The best R^2 values (in a set of 13 SAR scenes) were 0.71, 0.52, 0.35, and 0.70 for compartments 1 (91 stands), 2 (146 stands), 3 (113 stands), and 4 (156 stands), respectively. The corresponding RMSE values were 57, 74, 87, and 63 m^3/ha, respectively.

If various physiological properties affect the backscatter in various seasonal conditions multi-temporal techniques can benefit from efficient use of data from various seasons. The year can be divided (Paper 6) into the following periods and image acquisition conditions:

G1: the peak bio-chemical activity during the first half of the growing season,

G2: the second half of the growing season before the drop of the leaves of deciduous trees,

G3: the leaves-off period before the first snow,

WD: dry winter conditions, and

WW: wet winter conditions.

2 Materials and Methods

2.1 Study Sites and Data

The selection of study sites in the papers of this thesis was based on the availability of the necessary data, primarily the availability of SAR data, but also of ground data.

Study sites were located in three European countries (Sweden, Germany, and Finland) and in Africa. SAR data were used from the satellites Seasat and JERS and the airborne AIRSAR sensor.

2.1.1 Site and Data for Incidence Angle Study

The study site where topography and incidence angle effects on radar backscatter (Paper 1) were studied was in northern Sweden close to the village Arjeplog. The centre co-ordinates of the site were 66°.0 N (northern latitude) and 17°.3 E (eastern longitude relative to Greenwich).

The site includes mixed forests (mainly pine dominated), plantations of Norway spruce (*Picea abies*) and Scots pine (*Pinus sylvestris*), clear-cut areas, marshes, and lakes. In this northern study site, forest stem volume ranges form zero to about 100 m^3/ha. The soil type is mainly till (glacial drift). The soil contains stones and boulders up to 50 cm in diameter. The elevation varies between 420 and 780 m above mean sea level. The area can be considered as hilly or mountainous.

The Seasat SAR image of the site was acquired on 20 August 1978. Seasat SAR was an L-band, HH-polarised radar with a nominal mid-swath incidence angle of 23 degrees (Pravdo *et al.* 1983). The incidence angle varied between 20° (near range) and 26° (far range). The nominal (4-look) ground resolution was 25 m. The Seasat image was SAR processed by FOA (National Defence Research Establishment, currently FOI, Swedish Defence Research Agency, in Linköping, Sweden).

A digital elevation model (DEM) was used to geo-code the SAR image into the Swedish national grid ("rikets nät") and to compute incidence angles and resolution cell areas (A in Equation 7). The DEM (grid cell size 25 m by 25 m) was derived from the contour lines of Swedish topographic maps to a scale of 1:100 000 (contour interval 10 m). The DEM was generated by the Institute for Image Processing and Computer Graphics, Joanneum

Research Centre, Graz, Austria. The DEM covered an area of 19 km by 21 km. The terrain slopes in the area are smaller than 23 degrees. No accuracy estimate of the DEM were available. If half of the contour interval is used to describe the accuracy of the interpolated DEM – like in the case of a Finnish DEM (see section 2.1.4) – the vertical accuracy of the DEM in the Arjeplog study site can be assumed to be of the order of 5 m.

Estimation of forest stem volume and forest type classification were derived from an analysis of a Landsat Thematic Mapper scene (world reference system identifier 197-14) acquired on 25 June 1986. The RMSE of the stem volume model was 17.8 m^3/ha (R^2 of 0.67) in the training data. Since the model was applied to another TM scene, the estimation error can be much worse, perhaps of the oder of 30...40 m^3/ha.

2.1.2 Site and Data for SAR Mosaicking Study

The study site where JERS SAR mosaicking techniques (Papers 2 and 3) were studied comprised the whole forest belt of Africa. The mosaic area covers latitudes 10° S to 10° N and longitudes 14° W to 42° E. The mosaic includes large areas of tropical rain forest, with tree and grass savannah along the northern and southern borders of the area. Most of the area is flat or gently undulating below 500 m, but the eastern part of the area includes high mountains (*e.g.* Mount Kilimanjaro 5985 m).

SAR scenes (Paper 2) that were acquired for the GRFM African mosaic were divided in two acquisition layers: low water layer and high water layer. Two acquisitions were made in the GRFM project to allow the use of multi-temporal techniques in analysis of the mosaic images. The naming of these layers was based on the water level of the most important river system in the mosaic area, the Congo river. The low water layer covered the whole area as described above. The high water layer covered only longitudes 8° E to 36° E. The two layers included a total of 3624 JERS SAR scenes. The low water layer was acquired in January–March 1996. The high water layer was acquired in October–November 1996.

Each JERS SAR scene covered an area of 80 km by 80 km. The images were SAR processed by the Japanese Space Agency NASDA (currently JAXA) using the so-called NASDA processor. The pixel spacing in the 3-look images was 12.5 m. The images were standard level 2.1 products with geo-location data in Universal Transverse Mercator (UTM) co-ordinates. The images were down-scaled to 100 m pixel spacing by a wavelet-based technique (Simard *et al.* 1998).

Two types of cartographic data were used for geometric control of the mosaic:

- shore line polygons from the World Vector Shoreline database, and

- raster images of topographic maps.

The World Vector Shoreline database (NOAA 2005) was compiled by the Defense Mapping Agency (DMA) of the US (currently NIMA, National Imagery and Mapping Agency). The database was intended for use in a scale of 1:250 000 or smaller. The database was derived mainly from Joint Operations Graphics and coastal nautical charts produced by DMA. The accuracy requirement in this database is that 90 percent of identifiable features are within 500 m from their true position. The (preferred) datum is WGS-84.

The topographic maps were digitized raster images of 1:200 000 topographic maps in the Central African Republic and in the Republic of Congo. The maps were produced by the French mapping agency IGN and digitized by the Belgian company I-Mage in a World Bank program. The accuracy of these maps is not known.

2.1.3 Site and Data for Wavelength and Polarisation Study

The wavelength and polarisation aspects of forest biomass mapping (Papers 4 and 5) were studied in a study site in Schwarzwald, Germany. The study site (centre 48°03' N, 8°23' E) is located near the town of Villingen-Schwenningen. The site was the German study site (named Freiburg study site) in the MAESTRO-1 program (Churchill and Attema 1991) organized by the Joint Research Centre (JRC) of the European Union and the European Space Agency (ESA).

Due to the fairly high elevation (750 to 970 m) the site is dominated by tree species that are typical in boreal forest. Norway spruce (*Picea abies* Karst.) covers 1370 ha, Scots pine (*Pinus sylvestris* L.) 280 ha, and Silver fir (*Abies alba* Mill.) 200 ha. Forest stem volume varied between 0 and 830 m^3/ha.

The SAR data in Paper 4 consisted of two AIRSAR scenes (Held *et al.* 1988) acquired on 18 August 1989. Each scene had three bands: C, L, and P (wavelengths 6 cm, 23 cm, and 63 cm, respectively). The data

were SAR processed by Jet Propulsion Laboratory (JPL). Each pixel in each band contained the full scattering matrix: HH-, HV-, VH-, and VV-polarisations as complex numbers. The scattering matrix AIRSAR data were 1-look data (with nominal ground resolution of 4 m in azimuth and 14 m in range at 45° incidence).

The data were uncalibrated, but a number of 1.8 m trihedral corner reflectors were deployed in the study site during image acquisition. The incidence angle varied between 35° and 55° in scene 1105 and between 48° and 55° in scene 1107, which covered the study site only partially.

The SAR data in Paper 5 consisted of (in addition to the MAESTRO-1 scene 1105) two new AIRSAR scenes acquired on 15 June 1991 (scene 3169) and 16 July 1991 (scene 3275). These data were also SAR processed by JPL. These data were 16-look compressed Stokes matrix data (nominal ground resolution of 16 m in azimuth and 14 m in range at 45° incidence).

A number of 1.8 m trihedral corner reflectors were also deployed in the study site during the 1991 acquisitions. The author of this thesis (assisted by JRC personnel) constructed a 5 m trihedral corner reflector (of chicken wire) for the calibration of P-band data. The July 1991 scene was already calibrated by JPL, but the June 1991 scene was uncalibrated.

Meteorological data for the AIRSAR scenes of the study site is scarce. On 18 August 1989, temperature was 22 degrees C and air humidity 36 percent. Cloud cover was 4/8. There was no rain up to 24 hours before the image acquisitions (JRC 1990). There were some slight rain a few days before 15 June 1991. The day of image acquisition was without rain. The weather was partly cloudy (the AIRSAR aircraft was visible from the study site most of the image acquisition time) and the wind was weak. No meteorological data are available for 16 July 1991. High contrast between agricultural fields and forests suggest that vegetation has not at least been soaked with rain water.

DEM was used in the geo-coding of SAR data. The DEM was made in the MAESTRO-1 program by Universität Stuttgart/Instut für Navigation. The DEM (grid spacing 30 m) was produced using contour lines from German topographic maps of a scale of 1:50 000. An evaluation of the accuracy of the DEM was made against a more accurate topographic map in scale 1:25 000. Horisontal displacements in contour line positions of up to 45 m were found between the DEM and the 1:25 000 topographic map. The maximum vertical difference (in a set of three controlled points) in hill-top elevations was 8.9 m.

Forest inventory ground data in Papers 4 and 5 covered 230 forest stands totaling 1 920 ha (19.2 km^2). The inventory was made in 1981. The accuracy of this stand-wise inventory data is not known. An average RMSE in stand-wise stem volume inventory in Finland has been estimated to be of the order of 24.1 percent (Haara & Korhonen 2004). As the forest inventory data in the Freiburg study site was 8 and 10 years old at the time of SAR data acquisitions, it can be assumed that the forest inventory ground data in Papers 4 and 5 was less accurate than the ground data in the Ruokolahti study site in Paper 6. The forest inventory data consisted of a stand map in a scale of 1:10 000 and stand-wise data sheets (situation 1 October 1981). An attempt was made to take tree growth into account. Forest stem volume was plotted against stand age and a piece-wise linear regression model was fitted with the data. The forest stem volume of the forest inventory dataset was then updated with this simple "growth model" over the 8 year time before the first AIRSAR acquisition. The updated forest stem volume data were compared to ground measurements (June 1991, Rauste 1991) in eight stands. The difference between the updated forest stem volume data and the ground measurements were more random than the difference between the 1981 forest stem volume and the ground measurements. For this reason, the updating approach was abandoned and data from the 1981 forest inventory was used in analysis of the AIRSAR data.

2.1.4   Site and Data for Multi-Temporal L-Band Radar Backscatter Study

The study site (centre 61°31' N, 28°46' E) for the multi-temporal L-band study was located in south-eastern Finland within the municipalities Puumala and Ruokolahti (Paper 6). The most common tree species in the site were Scots pine (*Pinus sylvestris* L.), Norway spruce (*Picea abies* Karst.), and birch (*Betula pendula* and *Betula pubescens*). The dominant soil type was till (glacial drift). Forest stem volume varied between 0 and 364 m^3/ha.

The SAR data included six JERS SAR scenes. The JERS SAR is an L-band, HH-polarisation SAR with a nominal incidence angle of 39°and 3-look ground resolution of 18 m. The JERS SAR scenes were acquired on 20 February 1993, 25 January 1995, 20 July 1995, 2 September 1995, 16 October 1995, and 14 March 1998. These scenes are later referred to as scenes Dry93Feb, Wet95Jan, S95Jul, S95Sep, S95Oct, and Dry98Mar, respectively. All scenes were acquired on the same nominal orbit path so that the imaging geometry is identical from scene to scene. Summer

scenes were acquired in fairly dry conditions. The precipitation on the acquisition day varied between 0.1 and 1.5 mm and on the preceding day between 0.1 and 2.4 mm. The dry winter scenes were acquired in cold conditions. The temperature had been below zero for four days before the scene Dry93Feb and for 13 days before the scene Dry98Mar. The scene Wet95Jan was acquired on a day when the maximum temperature was 0.2° C and the minimum -2.1. The precipitation (as snow) on the acquisition day of the scene Wet95Jan was 1.4 mm and on the previous day 9.7 mm.

The first JERS scene was SAR processed by ESA. The 1995 scenes were SAR processed by NASDA using the so called new NASDA processor. The last scene was processed by NASDA using the Sigma-SAR processor. The first scene was uncalibrated. For the other five scenes NASDA provided calibration factors (Shimada 1996, Shimada and Isoguchi 2002).

The DEM (25 m grid spacing) used in the geo-coding of the SAR data was produced by the Finnish National Land Survey. Contour lines of topographic maps of the scale of 1:20 000 were used in the DEM production. The DEM covered an area of 38 km by 51 km. The vertical accuracy of the DEM is considered to be 2.5 m (half of the contour interval of the topographic map material, Haggrén & Honkavaara 2004).

Forest inventory ground data were available from two sources:

- the forest management information system of Stora Enso Ltd. (the forest owner), and

- measurement of a grid of plot data by the Finnish Forest Research Institute.

The stand-wise data were inventoried in 1997. The stand-wise forest inventory dataset did not include accuracy estimate of the data. Haara and Korhonen (2004) have studied the reliability and accuracy of stand-wise forest inventory data that were made using similar inventory methods. Haara and Korhonen (2004) found the RMSE of stand-wise forest stem volume data to be 21.4 percent (of the stem volume). They also found that the RMSE in stem volume inventory varied from 10.6 to 33.9 percent depending on the person who made the inventory. The stand-wise forest management data included – after elimination of stand boundary areas and stands smaller than 2 ha – 206 stands that covered a total of 845 ha.

The plot data (covering an area of 1 km by 1 km inside the area covered

by the stand-wise inventory data) were measured in a regular grid with 50-m spacing between grid points. The diameter of a plot was about 25 m. The plot data were measured in 2000. The plot size is of the order of one (3-look) pixel in JERS SAR data. This means that very little averaging can be done in SAR data to obtain accurate backscattering coefficient data for each plot. For this reason, the plot data was used in Paper 6 as an independent but less representative data source to verify results obtained using the stand-wise data.

2.2 Methods

2.2.1 Methods for Incidence Angle Study

Pre-processing of Seasat SAR data in Paper 1 included ortho-rectification using a DEM and manually measured ground control points (Rauste 1988). The SAR data were averaged to 75 m pixel size to reduce speckle before statistical analysis.

Linear regression analysis was used to determine the amount of variation in the SAR data explained by terrain topography (including topography-simulated SAR data, resolution cell area, slope and aspect) or forest stem volume.

A simulated SAR scene that depends only on terrain topography was made. Using only land pixels (water masking by Landsat TM data), each pixel value (backscattering amplitude in the SAR scene) was divided by the square root of the area of the resolution cell A. The data were then cross-tabulated against the incidence angle. A second-degree polynomial was then fit to the cross-tabulated data. This polynomial gives the backscattering coefficient σ^o as a function of incidence angle. In the simulation stage, the incidence angle was computed from the DEM. A σ^o value was then computed using the polynomial. The σ^o was then multiplied by the area of the resolution cell A, which was also computed using the DEM.

In the computation of the simulated SAR scene, the so-called thermal noise floor was first subtracted from Seasat SAR data. The noise floor was estimated from the SAR data using the darkest water areas of the scene.

The double-bounce backscattering mechanism is illustrated in Figure 7. When the ground is flat and horizontal (Figure 7 a), vertically growing tree
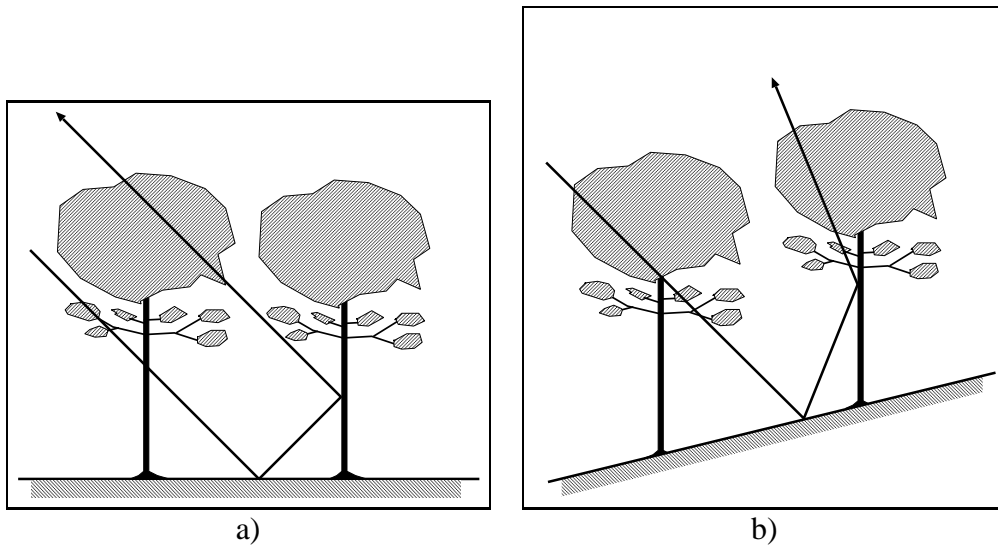
Figure 7. Double-bounce scattering with horizontal ground, a) and with sloping ground, b).

stems form a 90 degree angle to the ground. This geometry forms a corner reflector: the incoming radar signal reflects from the ground and the tree stems in such a way that it always returns back to the direction it came from – independent of the incidence angle. If the ground is tilted and the tree stems vertical (Figure 7 b), there is no 90 degree angle between the ground and tree stems. The double-bounce signal is then reflected in a direction away from the radar.

The following hypothesis was proposed: If the double-bounce component is important in the SAR data of a study site, the backscattering coefficient (σ^o, corrected for the scattering area effects as described above) of horizontal flat pixels should be higher than the σ^o of pixels where the terrain slope is higher. For the testing of this hypothesis, the dataset was divided into two parts:

- pixels with a slope of between 0 and 2 degrees, and

- pixels with a slope of between 2 and 5 degrees.

Pixels with very high slopes were excluded because very steep slopes tend to have sparse forest cover and outcrops, which could influence the analysis.

In the absence of forest inventory data from the study site of Arjeplog, forest stem volume was estimated using a Landsat TM scene and a regression model developed in a northern Finnish study site by Tomppo (1986). A forest type classification was also made.

The dependence of σ^o on incidence angle was studied using linear regression. The σ^o values were cross-tabulated against incidence angle (θ) separately for various forest types. A linear regression model σ^o *vs.* θ was derived for each forest type. The slope of these linear models was then used to study differences in the σ^o *vs.* θ relation between forest types. The slope terms were compared in pair-wise students t-tests between forest types.

2.2.2   Methods for SAR Mosaicking Study

The SAR mosaicking methodology is described separately for scene geometry and scene radiometry.

Geometric Methodology for SAR Mosaicking   The image geometry revision method adopted in the mosaicking of JERS SAR data (Papers 2 and 3) is based on automatic correlation-generated tie points and on the use of least squares adjustment over the whole set of SAR scenes. In addition to the global adjustment as described by Siqueira *et al.* (2000) this approach includes the multi-temporal dimension, which guarantees the multi-temporal consistency between mosaics acquired at different times.

Since the scene geo-location data of JERS SAR level 2.1 products can be considered to describe the internal image geometry well, these data were used as the starting point in mosaic geometry revision. Like in Rosaz *et al.* (1994) and Siqueira *et al.* (2000), the similarity transformation (Figure 8) was chosen as the geometric model of scene revision.

Unlike in Rosaz *et al.* (1994) and Siqueira *et al.* (2000), the co-ordinates x and y are not image co-ordinates (azimuth-range) but cartographic co-ordinate differences relative to the scene centre. The map projection of the northing-easting co-ordinates (N and E in Figure 8) can be chosen. The Mercator projection had been chosen in connection with the definition of the GRFM project.

Also unlike in Rosaz *et al.* (1994) and Siqueira *et al.* (2000), the rotation angle α is not a heading difference between orbits but a deviation from
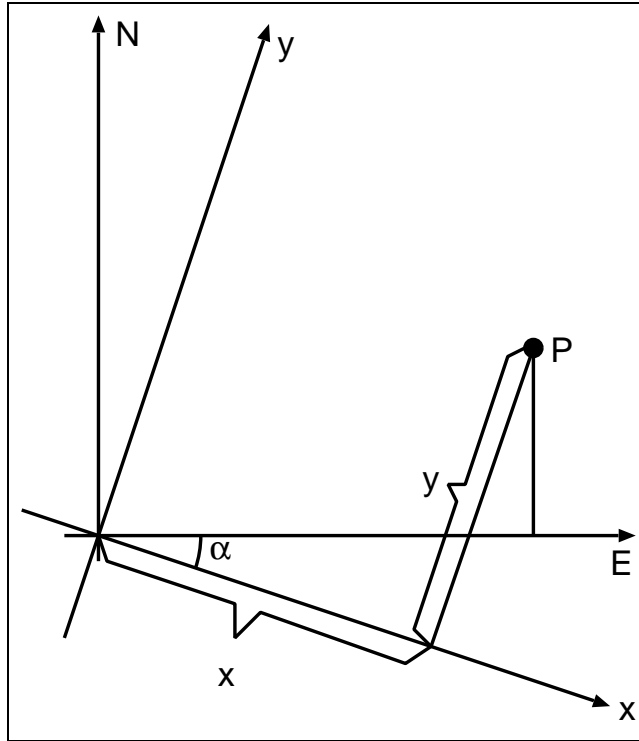
Figure 8. Image co-ordinate systems centred at scene centre.

the scene orientation as estimated by the SAR processor. Therefore, the expected value of α is zero, and its variance can also be expected to be small because the orbit heading can be reliably estimated from orbit data.

In the least squares adjustment (*e.g.*, Hirvonen 1965), observations are expressed as a function of unknown parameters (vector $\mathbf{x}$):

$$v_i = f(\mathbf{x}). \tag{17}$$

Here $f(\mathbf{x})$ is a function of the form where the observed quantity is subtracted from the theoretically calculated value of that quantity.

The number of observations n must be greater than the number of parameters m. Linearizing Equation 17 gives:

$$v_i = \sum_{j=1}^{m} \frac{\partial f}{\partial x_j} \delta x_j + f 0_i. \tag{18}$$

Here δx_j is the improvement to the initial value $x0_j$. $f0_i$ is the estimated value of observation i with initial values of vector $\mathbf{x}$. Equation 18 can be written in vector form:

$$\mathbf{v} = \mathbf{A}\mathbf{x} + \mathbf{l} \tag{19}$$

where $\mathbf{v}$ = residual vector of n elements, $\mathbf{l}$ = vector of n $f0$ values (before-adjustment discrepancies), and $\mathbf{A}$ is an n by m matrix of partial derivatives:

$$a_{i,j} = \frac{\partial f_i}{\partial x_j}, \tag{20}$$

evaluated at the point corresponding to observation i.

If the observations have different weights ($\mathbf{P}$ is a diagonal weight matrix with $p_{i,i}$ the weight of observation i) the weighted square sum of errors is:

$$\mathbf{v}^\mathbf{T}\mathbf{P}\mathbf{v} = \mathbf{x}^\mathbf{T}\mathbf{A}^\mathbf{T}\mathbf{P}\mathbf{A}\mathbf{x} + 2\mathbf{x}^\mathbf{T}\mathbf{A}^\mathbf{T}\mathbf{P}\mathbf{l} + \mathbf{l}^\mathbf{T}\mathbf{P}\mathbf{l}. \tag{21}$$

Using the following notations:

$$\mathbf{N} = \mathbf{A}^\mathbf{T}\mathbf{P}\mathbf{A} \tag{22}$$

and

$$\mathbf{u} = \mathbf{A}^\mathbf{T}\mathbf{P}\mathbf{l}, \tag{23}$$

the minimum of the weighted square sum of errors can be found by solving (Hirvonen 1965)

$$\mathbf{N}\mathbf{x} + \mathbf{u} = \mathbf{o} \tag{24}$$
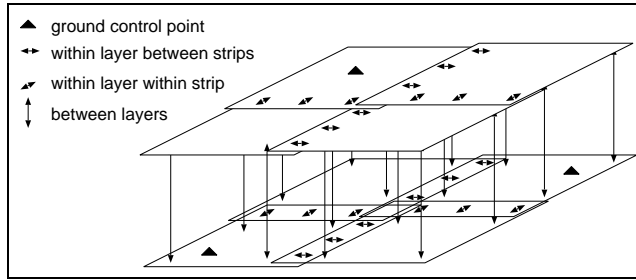
Figure 9. Ground control points and types of tie points with respect to acquisition layers and image strips (orbits).

for $\mathbf{x}$. Matrix $\mathbf{N}$ is called the normal equation coefficient matrix. The vector $\mathbf{o}$ is a vector of m zeroes.

In the block adjustment method adopted in Papers 2 and 3, the observation Equations (17) are of three different types:

1. tie point equations between scenes,

2. ground control point equations between a scene and the cartographic co-ordinate system, and

3. orbit data equations.

Tie points can be further divided into three groups (Figure 9):

1. tie point within a single acquisition layer between two adjacent strips,

2. tie point within a single acquisition layer within a strip between two consecutive frames, and

3. tie point between two acquisition layers.

If scenes of an orbit are acquired on the same day, tie points within strips (type 2 above) are special in the sense that these points can be correlated without strong contrast in the scene. This is due to the fact that the speckle pattern is identical in both scenes in the overlap area (due to common raw data in SAR processing). Other tie point types require a contrast-rich feature that remains stable over the image acquisition interval. From the point of view of observation equations, all tie point types are identical.

51

In the following observation equations, the unknown parameters that are solved in the least squares adjustment are:

δN^c = translation in northing of the scene,
δE^c = translation in easting of the scene, and
α = rotation of the scene.

For tie point observation equations, we can read in Figure 8:

$$N^p = N^c + \delta N^c + y * cos(\alpha) - x * sin(\alpha) \tag{25}$$

$$E^p = E^c + \delta E^c + x * cos(\alpha) + y * sin(\alpha) \tag{26}$$

where
N^p = northing of point P,
E^p = easting of point P,
N^c = northing of the scene centre,
E^c = easting of the scene centre,
x, y = image co-ordinates relative to scene centre (see Figure 8).

For a tie point observed in two scenes, the observation equations are:

$$
\begin{aligned}
V_{N^p} &= N_1^p - N_2^p \\
&= N_1^c - N_2^c + \delta N_1^c - \delta N_2^c + y_1 * cos(\alpha_1) - y_2 * cos(\alpha_2) - \\
& \quad x_1 * sin(\alpha_1) + x_2 * sin(\alpha_2)
\end{aligned} \tag{27}
$$

and

$$
\begin{aligned}
V_{E^p} &= E_1^p - E_2^p \\
&= E_1^c - E_2^c + \delta E_1^c - \delta E_2^c + x_1 * cos(\alpha_1) - x_2 * cos(\alpha_2) + \\
& \quad y_1 * sin(\alpha_1) - y_2 * sin(\alpha_2),
\end{aligned} \tag{28}
$$

where V_{N^p} and V_{E^p} are the residual error of the tie point co-ordinates in northing and easting, respectively.

For ground control points with known geodetic co-ordinates N_g and E_g and estimated co-ordinates N_e and E_e, the observation equations are:

$$
\begin{aligned}
V_{N^g} &= N_e^p - N_g^p \\
&= N^c + \delta N^c + y * cos(\alpha) - x * sin(\alpha) - N_g^p
\end{aligned} \tag{29}
$$

and

$$
\begin{aligned}
V_{E^g} &= E_e^p - E_g^p \\
&= E^c + \delta E^c + x * cos(\alpha) + y * sin(\alpha) - E_g^p,
\end{aligned} \tag{30}
$$

where V_{N^g} and V_{E^g} are the residual error of the ground control point coordinates in northing and easting, respectively.

The orbit data equations are:

$$v_{N^c} = \delta N^c, \tag{31}$$

$$v_{E^c} = \delta E^c, \text{ and} \tag{32}$$

$$v_\alpha = \alpha. \tag{33}$$

In the linearization of observation equations (computation of partial derivatives needed in the matrix $\mathbf{A}$) the following approximations were made because the angle α is always very small:

$$sin(\alpha) \approx \alpha \approx 0 \tag{34}$$

and

$$cos(\alpha) \approx 1 \tag{35}$$

The partial derivatives needed in matrix $\mathbf{A}$) were derived from Equations (27) through (33).

Residual errors after least squares block adjustment can be used as a diagnostic tool to evaluate the geometry of the resulting SAR image mosaic. An additional tool for the evaluation is a diagram of error ellipses of the estimated scene centres. The semi-major (m_{uu}) and semi-minor (m_{vv}) axes of the error ellipses are (Hirvonen 1965):

$$m_{uu} = m_o \sqrt{Q_{uu}} \tag{36}$$

$$m_{vv} = m_o \sqrt{Q_{vv}} \tag{37}$$

where m_o is the mean square error of a unit weight observation and

$$Q_{uu} = \frac{1}{2}(Q_{NN} + Q_{EE} + W) \tag{38}$$

$$Q_{vv} = \frac{1}{2}(Q_{NN} + Q_{EE} - W). \tag{39}$$

Here Q_{NN} and Q_{EE} are the main diagonal elements (of the inverse of the normal equation coefficient matrix) corresponding to the northing and easting translations of the scene in question and

$$W = \sqrt{(Q_{NN} - Q_{EE})^2 + 4Q_{NE}^2} \tag{40}$$
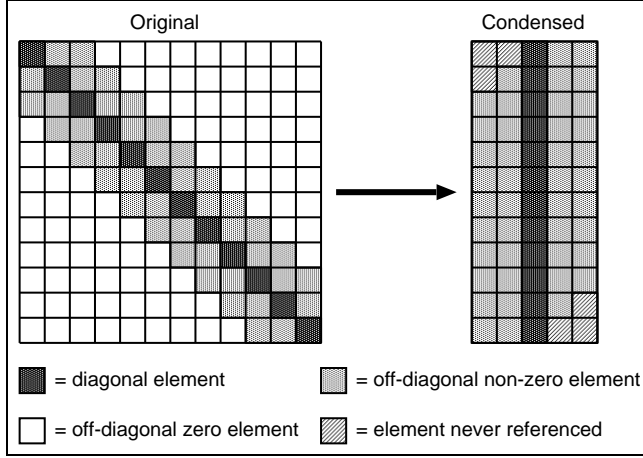
Figure 10. Condensed form of the normal equation coefficient matrix $\mathbf{N}$.

where Q_{NE} is the off-diagonal element corresponding to the northing and easting co-ordinates of the scene in question.

The orientation angle t of the semi-major axis can be solved from:

$$sin(2t) = \frac{2Q_{NE}}{W} \tag{41}$$

$$cos(2t) = \frac{Q_{NN} - Q_{EE}}{W}. \tag{42}$$

The dimension m of the normal equation coefficient matrix $\mathbf{N}$ is three times the number of scenes in the adjustment. If thousands of scenes are included, the $\mathbf{N}$ matrix becomes large. If the scenes are numbered systematically, the $\mathbf{N}$ matrix is a block diagonal matrix with a limited band-width w. The band-width depends on the order in which the various indices grow in the mapping from indices to image number. If scene numbering is such that the fastest growing index (of acquisition layer, strip, and scene within strip) is scene within strip, then acquisition layer, and slowest strip, the band-width is:

$$w = (2 * s_m + 1) * n_l * 3 \tag{43}$$

where s_m is the maximum number of scenes in a single strip (in an acquisition layer) and n_l the number of acquisition layers.

The $\mathbf{N}$ matrix was stored in the condensed form (Figure 10). Matrices $\mathbf{A}$ and $\mathbf{P}$ were not constructed, but the contribution to the matrix $\mathbf{N}$ (and to the $\mathbf{u}$ vector) of each observation equation was summed up directly to the

condensed-form N matrix (and u vector) when processing tie point and ground control point observations.

The conjugate gradient method (Press *et al.* 1992) was used to solve the normal equation system (24).

Radiometric Methodology for SAR Mosaicking   The radiometric calibration revision was carried out in two phases:

1. removal of constant range dependent artifacts, and

2. radiometric adjustment in overlap areas.

The constant range dependent artifacts result from the sensor antenna pattern, the sensor STC (Sensitivity Time Control) pattern, and the uncertainties connected with the removal of these effects in the SAR processor. The STC is a technique that aims at keeping the recorded signal level approximately constant despite the changes in antenna gain and spreading loss across the image swath. A major source of uncertainty in these corrections is the uncertainty of satellite attitude sensors (roll in particular) because the antenna gain changes rapidly with varying look angle close to the margins of the (vertical) antenna pattern.

An average range pattern was determined over all scenes in the mosaic (Paper 3). Each scene was then scaled (using the average range pattern) so that the average range pattern of the scaled scenes was a linear function of range.

As in Rosaz *et al.* (1994), the scene radiometry was adjusted using least squares adjustment. Unlike the pairwise processing of Rosaz *et al.* (1994), the least squares adjustment (in Paper 3) determined the calibration revision parameters for all scenes of the mosaic in a single adjustment.

The use of calibration tie points in scene-overlap areas and the aiming at identical radar responses in both scenes is justified because the backscattering coefficient γ^o can be expected to

1. be constant over the incidence angle range of JERS SAR , and

2. stay constant over the image acquisition interval.

The first assumption has been confirmed by scatterometer measurements in C-band (Lecomte and Attema 1992) and by JERS SAR data (Shimada

1996). The second assumption can be made because the African JERS SAR data of adjacent orbits were acquired on consecutive days for the major part of the mosaic area.

A bi-linear multiplicative calibration model was adopted in Paper 3 between the original backscattering amplitude r_o and the calibrated backscattering amplitude r_c:

$$
\begin{aligned}
r_c &= f * r_o & (44) \\
&= (f_0 + x * f_1 + y * f_2 + x * y * f_3) \cdot r_o & (45)
\end{aligned}
$$

where x and y are the normalized centred image coordinates.

Denoting:

$$
\begin{aligned}
f_0 &= 1 + \delta f_0, \\
f_1 &= (0+)\delta f_1, \\
f_2 &= (0+)\delta f_2, \text{ and} \\
f_3 &= (0+)\delta f_3
\end{aligned}
$$

the observation equation for a calibration tie point P was:

$$
\begin{aligned}
V^P = &\ r_1^P * \delta f_0^1 + x_1 * r_1^P * \delta f_1^1 + y_1 * r_1^P * \delta f_2^1 + x_1 * y_1 * r_1^P * \delta f_3^1 + r_1^P - \\
&\ r_2^P * \delta f_0^2 - x_2 * r_2^P * \delta f_1^2 - y_2 * r_2^P * \delta f_2^2 - x_2 * y_2 * r_2^P * \delta f_3^2 - r_2^P \quad (46)
\end{aligned}
$$

where V^P is the error (difference between the backscattering amplitudes in the two overlapping scenes) at point P. Here

r_1^P	=	observed backscattering amplitude in scene 1,
r_2^P	=	observed backscattering amplitude in scene 2,
δf_0^1	=	improvement of term f_0 for scene 1,
δf_1^1	=	improvement of term f_1 for scene 1,
δf_2^1	=	improvement of term f_2 for scene 1,
δf_3^1	=	improvement of term f_3 for scene 1,
δf_0^2	=	improvement of term f_0 for scene 2,
δf_1^2	=	improvement of term f_1 for scene 2,
δf_2^2	=	improvement of term f_2 for scene 2,
δf_3^2	=	improvement of term f_3 for scene 2.

Corresponding to the orbit data Equations (31) to (33) in geometric block adjustment, the calibration adjustment included the following observation equations for the calibration parameters:

$$
V_{f0} = \delta f_0 \quad (47)
$$

56

$$V_{f1} = \delta f_1 \tag{48}$$
$$V_{f2} = \delta f_2 \tag{49}$$
$$V_{f3} = \delta f_3. \tag{50}$$

where V_{f0} to V_{f3} are the errors of calibration revision coefficients f_0 to f_3, respectively.

2.2.3 Methods for Wavelength and Polarisation Study

Polarimetric AIRSAR data were used when studying the optimal wavelengths and polarisations for forest biomass mapping (Papers 4 and 5). Those AIRSAR scenes that were not already calibrated were calibrated using the methods described by van Zyl (1990) and Zebker and Lou (1990). The August 1989 scenes, which were stored in scattering matrix format, were converted to Stokes matrix format. A linear correction was made to the range pattern of the June 1991 scene to correct for a calibration anomaly in that scene.

The Stokes matrix scenes were ortho-rectified using ground control points and a digital elevation model. Averaging was done in ortho-rectification to reduce speckle. Gaussian weights were used in the resampling of Stokes matrix elements of the ortho-rectified scenes. The amount of speckle reduction was controlled by the standard deviation of the Gaussian weight function. In the ortho-rectification of the August 1989 scenes, the standard deviation was 0.8 pixels in slant range and 0.8 pixels in azimuth (about 70 percent of the 12.5 m pixel spacing of the ortho-rectified scenes). In the ortho-rectification of the 1991 scenes (with lower speckle due to 16-look format), the standard deviation of the Gaussian weight function was 0.35 pixels in slant range and 0.5 pixels in azimuth.

The Stokes matrix elements, which were proportional to received power quantities, were corrected for topographic effects:

$$P_c = P_o \frac{tan(\theta_r)}{tan(\theta_n)} \tag{51}$$

where P_c is the terrain-corrected Stokes matrix element, P_o is the original Stokes matrix element, θ_r is the incidence angle in range (depending on the local topography), and θ_n is the nominal incidence angle (which varies across the image swath) assuming a flat earth. This form of terrain-correction means that the corrected Stokes matrix elements are proportional to γ^o of Equation (9).

Stokes matrix data were averaged per forest stand using a digital stand mask derived from the forest inventory map.

A systematic search was used to find the polarisation combination that maximised the correlation between backscattering amplitude and forest stem volume. Starting with the stand-wise averaged Stokes matrix data and forest stem volume data for stands:

- the received power was computed for each stand using polarisation synthesis (van Zyl *et al.* 1987),

- correlation coefficient was computed between the forest stem volume and the backscattering amplitude over all stands.

The above optimisation was computed over the 4-dimensional space of polarisation combinations (receive orientation, transmit orientation, receive ellipticity, and transmit ellipticity) in a grid with a grid spacing of 10 degrees in all dimensions.

Visual comparison of correlation coefficient diagrams was used to analyse the temporal stability of the forest biomass *vs.* backscattering amplitude relation. Multiple linear regression analysis was used to study the relation between forest stem volume and backscattering amplitude. The form of the regression function was:

$$V = \alpha_o + \alpha_1 \cdot x_1 + \alpha_2 \cdot x_2 + \alpha_3 \cdot x_3 (+\epsilon) \tag{52}$$

where V was forest stem volume, independent variables x_1 to x_3 were the AIRSAR acquisitions of August 1989, June 1991, and July 1991, respectively, α_o to α_3 were regression coefficients, and ϵ was the random error. Scatter plots between backscattering amplitude data from two acquisitions were used for change detection.

2.2.4 Methods for Multi-Temporal L-Band Radar Backscatter Study

Multi-Temporal L-band SAR data in forest biomass mapping were studied in the Ruokolahti study site (Paper 6). JERS SAR scenes were ortho-rectified using a DEM, manually measured ground control points, and tie points between scenes.

The JERS SAR data, which were in backscattering amplitude format, were corrected for terrain effects on image radiometry:

$$r_c = r_o \sqrt{\frac{tan(\theta_r)}{tan(\theta_n)}} \qquad (53)$$

where r_c is the terrain-corrected backscattering amplitude, r_o is the original backscattering amplitude, θ_r is the incidence angle in range, and θ_n is the nominal incidence angle (39 degrees for JERS SAR; since the study site was only 40 km wide a constant θ_n could be used for a space-borne sensor). This form of terrain-correction means that the corrected backscattering amplitude is proportional to $\sqrt{\gamma^o}$ of Equation (9). Since the terrain correction is made relative to the nominal incidence angle, the average level of the backscattering amplitude does not change from the original level. The calibration factors presented by Shimada (2001) are therefore also applicable to the terrain-corrected backscattering amplitude data. The result of the calibration equations in Shimada (2001) is called σ^o. Because all radar-biomass relations published in the literature have been described in terms of σ^o (not γ^o) the notion of σ^o was used in Paper 6 also.

JERS SAR data were averaged (in power format) per forest stand using a stand mask from forest inventory data. The stands were first eroded by one (25 m) pixel, and only those stands were included in analyses where the stand was 2 ha or more after the erosion step.

Regression analysis, both simple regression and multiple regression, were used to analyse the relation between forest stem volume and L-band backscattering amplitude. Regression analyses were made for various datasets limited by the stem volume range. In these analyses, the number of observations (stands) varied between 19 and 206. In Paper 6, the adjusted R_A^2 (Rudner *et al.* 2002) was used to take this variation into account:

$$R_{A_1}^2 = R^2 - \frac{(1 - R^2) \cdot p}{n - p + 1} \qquad (54)$$

where R^2 is the coefficient of determination, n = number of observations, and p = number of independent variables (1 to 6 SAR scenes). There are at least two other variations of the adjusted R_A^2 (Wulder 2005):

$$R_{A_2}^2 = R^2 - \frac{(1 - R^2) \cdot (p - 1)}{n - p} \qquad (55)$$

and (Jensen 2005):

$$R_{A_3}^2 = 1 - \frac{(1 - R^2) \cdot (n - 1)}{n - p - 1}. \qquad (56)$$

The R_A^2 values of these definitions are also listed in section 3.5.

3 Results and Discussion

3.1 Incidence Angle Effects on L-band Radar Backscatter in Forests

Incidence angle effects – due to local topography – were studied in the Arjeplog study site in northern Sweden. Five independent variables were used in regression analysis where the dependent variable was the Seasat SAR-measured (not corrected for any topographic effects) backscattering amplitude:

topo: topography-simulated SAR image in amplitude as described in section 2.2.1,

vol: forest stem volume estimated from Landsat TM data,

area: (square root of the) area A of the resolution cell computed using DEM data, as described in section 1.1 (Equation 7),

slope: terrain slope computed using DEM data, and

aspect: azimuth of steepest slope with respect to the SAR illumination direction.

Table 2 shows the coefficient of determination (the proportion of total variance accounted for by the independent variables) and the correlation coefficient from linear regression. The correlation coefficient in Table 2 can be considered as the correlation coefficient between a predicted and observed backscattering amplitude when using the independent variables as predictors. In the single-variable cases this is equal to the correlation coefficient between the independent variable and the observed backscattering amplitude (the dependent variable).

The terrain topography is the strongest single factor contributing to the variation in backscattering amplitude in the study site. The topography-simulated SAR image explained 63.1 percent of the total variance in the SAR scene. It is possible that a more detailed and accurate DEM would have increased the proportion of variation that is accounted for by terrain topography. Visual inspection of the SAR scene and the DEM suggested that the SAR scene contained fine-scale topographic variation that was poorly described by the DEM. However, the averaging of the SAR scene to 75 m pixel spacing reduced this fine-scale variation.

Table 2. Regression analysis results in the Arjeplog study site. Dependent variable is the digital number (backscattering amplitude) in a Seasat SAR scene. See section 3.1 for the independent variables. The number of observations (pixels) was 23446 (Paper 1).

Independent variables	Coefficient of determination (%)	Correlation coefficient
topo + vol	65.4	0.81
topo	63.1	0.80
vol	0.3	0.05
area + vol	62.4	0.79
area	60.8	0.78
slope + aspect	3.4	0.19

When adding the (Landsat-derived) stem volume, the proportion of explained variance rose to 65.4 percent. When correlating the stem volume against SAR data that has not been corrected for topographic effects, stem volume is almost uncorrelated to SAR data (the correlation coefficient is only 0.05).

Most of the topography influence comes from the variation of the area of the resolution cell because this (the variable 'area' in Table 2) alone explained 60.8 percent of the total variance. Adding the dependence of the backscattering coefficient σ^o on the incidence angle (variable 'topo' in Table 2), increased the coefficient of determination to 63.1 percent.

Terrain slope and aspect do not explain well (in linear regression analysis) the effects of topography on backscattering amplitude. This can be understood because an increasing terrain slope on fore-slopes (slopes toward the radar) increases the backscattering amplitude whereas an increasing terrain slope on back-slopes (slopes away from the radar) decreases the backscattering amplitude (see Equations 4 and 9).

The proportion explained by terrain topography in Foody (1986) was significantly lower than the 60 percent accounted for by scattering area in Table 2. The main reasons for this might be the higher nominal incidence angle of the Convair-580 sensor (32° to 63° *vs.* 23° of Seasat), which reduces the topographic effects, and a study site (undulating) with less topographic variation. The proportion of variation explained by slope and aspect in Foody (1986) was on the average higher than the 3.4 percent in Table 2. The reason for the higher R^2 in Foody (1986) is most likely the

different statistical analysis techniques (multiple linear regression in Paper 1 *vs.* computation using zero and first order partial correlations in Foody, 1986).

The hypothesis on the double-bounce scattering component was tested with flat (slope 0 to 2 degrees) and non-flat (slope 2 to 5 degrees) forested pixels. The flat average backscattering amplitude was 104 (in arbitrary units) while the non-flat average backscattering amplitude was 106. This suggests that the double-bounce component is not very important in the study site. The reason may be rough (in terms of the 23 cm wavelength of the Seasat SAR) ground (glacial drift with stones and boulders). Rough ground reduces the ground reflection of the double-bounce component (in flat pixels) and also increases the direct backscattering component (both in flat and sloping pixels). Pulliainen *et al.* (1999) also found in a Finnish study site that the stem-ground reflection is small compared to the direct backscattering from forest canopy.

Figure 11 shows the square root of backscattering coefficient (σ^o) as a function of incidence angle in the Arjeplog study site and linear regression functions for the following forest types:

- spruce-dominated mixed forest,

- pine-dominated mixed forest,

- deciduous-dominated mixed forest, and

- clear-cut areas.

The independent variable in the regression analysis was $cos(\theta)$ and the dependent variable $\sqrt{\sigma^o}$. The forest types were mapped using a Landsat TM scene (section 2.2.1). When using tens of thousands of pixels as observations, the slope terms of the regression functions differed significantly (at a 5 percent significance level) between all possible pairs of forest types. The slightly different backscatter-dependence on incidence angle is probably due to different stem volumes in different forest types. On average, spruce-dominated mixed forests had the highest average stem volume in the study site. Also many other factors can have an influence such as understory, soil type, and tree structure.

Even though the regression functions were different for different forest types the σ^o data of forest types overlapped. At 30° incidence angle, where the forest type differences were largest, the average L-band backscattering
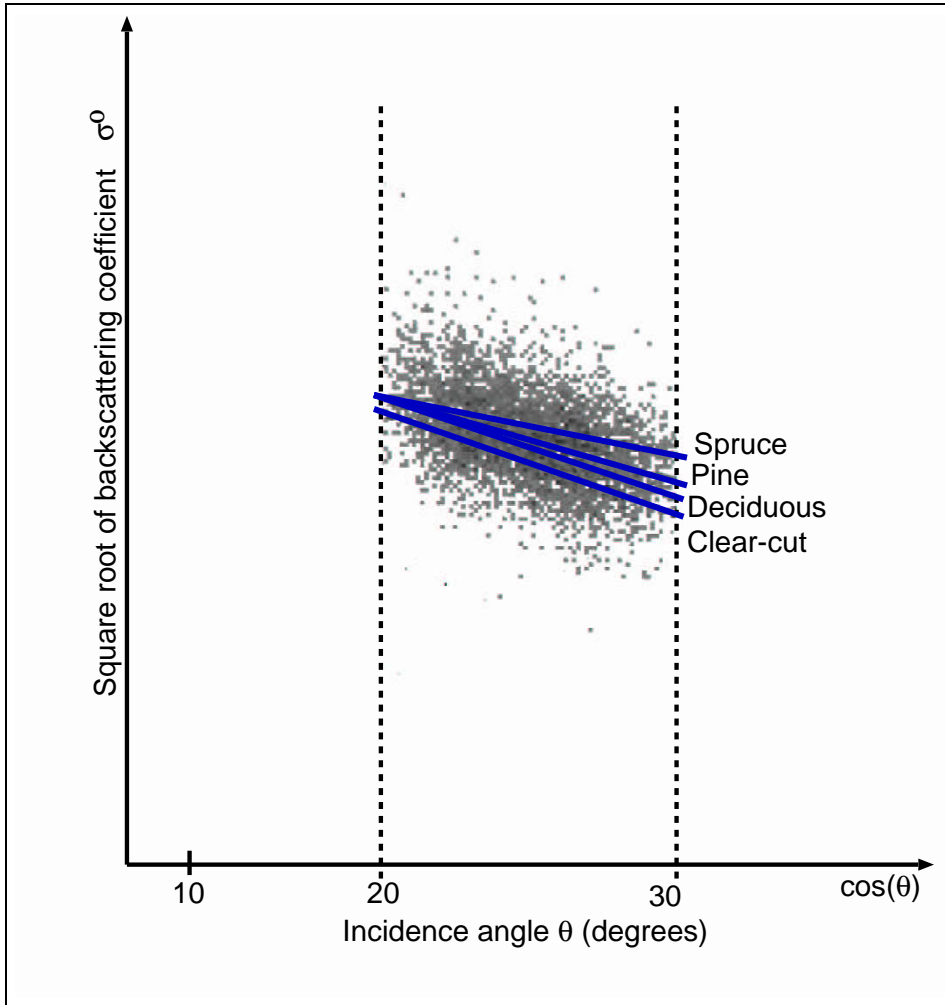
Figure 11. Backscattering coefficient (σ^o) in L-band Seasat SAR data as a function of incidence angle (θ) for various forest types in the Arjeplog study site. Total number of observations (pixels) = 23 446.

amplitude for spruce-dominated mixed forests was only 17 percent higher than that of clear-cut areas and 11 percent higher than the deciduous-dominated mixed forest.

3.2 Geometry in SAR Mosaicking

The geometry revision approach described in Papers 2 and 3, and in section 2.2.2 was applied to the GRFM African dataset of JERS SAR scenes. A total of about 62 000 tie points were produced using an automatic image correlation method. A set of 248 ground control points (GCPs) were measured using an interactive method by displaying shoreline polygons on top of JERS SAR scenes from the World Vector Shoreline database. A set of about 50 GCPs were measured from topographic maps. Water areas and outlines of land features were displayed as opaque colours (other areas as transparent) on top of JERS SAR data.

Table 3 shows the root mean square error (RMSE) statistics when the tie point and GCP datasets were used in block adjustment. The column 'Tie point' gives RMSE computed over all 62 000 tie points in the adjustment, separately for easting and northing. The column 'Scene centre' gives the square average of all scene translations (a scene translation is considered as an error, Equations 31 and 32), separately in easting and northing. The column 'GCP' gives RMSE computed over the set of GCPs, separately in easting and northing. The column 'p_g' gives the weight assigned to GCP observations. The weight of a tie point observation was always 1. The weight of the scene centre Equations (31 and 32), was always $\frac{1}{1000}$. The $\frac{1}{1000}$ weighting of scene centre positions from scene header data corresponds approximately to the estimated variance ratio between these data and the tie point measurements as estimated in some problem scenes in connection with preliminary mosaicking attempts.

When compiling the GRFM African mosaic, obtaining accurate and reliable cartographic data for geometric validation was difficult. The strategy for evaluating the geometric accuracy of the mosaic was to use the tie point and GCP datasets in different combinations. Table 3 shows the RMSE statistics for three adjustments:

1. the adjustment where only tie points and orbit data were used to determine the mosaic geometry,

2. the adjustment where tie points, orbit data, and GCPs from the World

Table 3. Root mean square error statistics of the geometric block adjustments of the GRFM African JERS SAR mosaic. All values are in metres. N = northing, E = easting (Paper 2).

Case	Tie point		Scene centre		GCP		p_g
	N	E	N	E	N	E	
1	33.2	34.8	477.5	751.7	503.0	1021.4	0
2	35.5	40.8	532.0	736.2	193.7	201.6	2
3	40.1	39.7	543.3	758.0	173.2	166.3	2

Vector Shoreline database were used to determine the mosaic geometry, and

3. the adjustment where tie points, orbit data, and GCPs from the World Vector Shoreline database and topographic maps were used to determine the mosaic geometry.

In the first adjustment (case 1 in Table 3) GCPs from the World Vector Shoreline database were included but their weight was zero. The GCPs served as independent validation data. The tie point RMSE values of 33.2 and 34.8 m (in easting and northing) indicate that the mosaic internal consistency is good at sub-pixel level. The pixel size of the scenes to mosaic was 100 m. The RMSE values in GCPs (503.0 m in northing and 1021.4 m in easting) show that absolute geo-location accuracy is (on average) of the order of 10 pixels if no GCPs are used. The scene centre Figures (477.5 m in northing and 751.7 m in easting) tell how large relative movements (from the scene positions given in scenes' geo-location data) are needed to compile a spatially consistent JERS SAR mosaic when using SAR scenes from the so-called new NASDA processor.

In the second adjustment (case 2 in Table 3), GCPs from the World Vector Shoreline database were included in the determination of the mosaic geometry also. The tie point RMSE increased slightly compared to the tie-points-only case, but the RMSE is still within a sub-pixel of the mosaic. The mosaic was shifted by about 0.5 to 1 km with respect to the location derived from the scenes' geo-location data. This shift decreased the RMSE values of GCPs to about 200 m. This value is smaller than the accuracy requirement of the World Vector Shoreline polygons (90 percent of features within 500 m of its true location).

In the third adjustment (case 3 in Table 3), GCPs from topographic maps

(in the Central African Republic and Republic of Congo) were also added. This shifted the mosaic only slightly, and the RMSE values did not change much from case 2. This suggests that adding new GCPs would not change the mosaic geometry much. The mosaic geo-location accuracy (Paper 2) was therefore considered to be most likely within a few hundred meters throughout the mosaic.

The accuracy figures of Table 3 cannot be directly compared to accuracy figures from other studies. This is due to the differences in SAR systems, SAR processors, and orbital data used in the SAR processors. Rosaz *et al.* (1994) presented no geometric accuracy figures for the compiled ERS-1 SAR mosaic. Siqueira *et al.* (2000) estimated the mean geo-location error of the JERS-1 SAR mosaic of Amazon to be 38 m in latitude and 32 m in longitude, when applying average geo-location correction to clusters of 1 degree by 1 degree. This error describes the internal accuracy of the mosaic. When the mosaic was transformed using similarity transformation (rotation and shifts in latitude and longitude) the residuals in GCPs (27 used to tie down the mosaic, 30 used to estimate geo location accuracy) were estimated to be within +/- 400 m. Shimada and Isoguchi (2002) estimated the geometric accuracy of the Southeast Asian JERS-1 SAR mosaic to be 406 m. Hutton *et al.* (2000) estimated the geometric accuracy of the Radarsat-1 mosaic of Canada to be in the order of one pixel or 250 m. Noltimier *et al.* (1999) estimated the absolute geometric accuracy of the Radarsat-1 mosaic of Antarctica to be 150 m or better.

The error ellipses (for case 3 in Table 3) were computed using Equations (36) to (42) and shown in Figure 1 of Paper 2. The semi-major axis of the error ellipse (for a scene centre) varied between 6 and 55 m (median 11 m). The semi-minor axis varied between 6 and 30 m (median 10 m).

Most of the error ellipses were almost circular, which indicates that the uncertainty in the geo-location in these areas is approximately equal in all directions. Most of the ellipses were also of the average dimension, which indicates that the uncertainty in geo-location in these areas is approximately uniform over the area. In sea areas, where tie points were impossible to find between neighbouring strips (orbits), the error ellipses increased in dimension and became elongated. Other such areas where larger and less regular error ellipses indicated worse geo-location accuracy were found along the northern and southern margin of the mosaic area. These were areas where the closest GCPs were distant. Irregular shaped "extensions" of the mosaic area also produced large error ellipses. This phenomenon was especially prominent in the north-western and north-eastern corners of the mosaic.

66

a)   b)
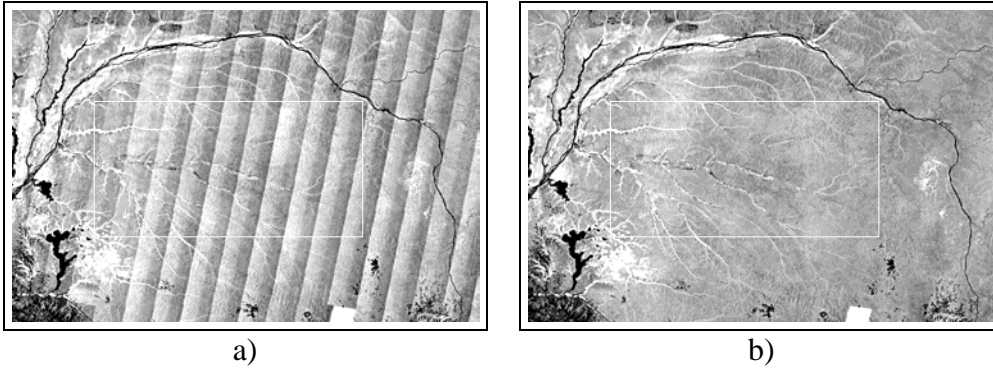
Figure 12. A subset of the high-water acquisition layer of the GRFM African mosaic before a), and after b) calibration revision. The area covered is about 1000 km in east-west direction and about 670 km in north-south direction (Paper 3).

The geometric methods of mosaicking that were applied in the compilation of the GRFM African mosaics can be applied to other similar SAR data sets. This requires that the SAR data has associated geo-location data the describes the internal geometry of SAR scenes reliably even though absolute locations may include random or systematic errors of hundreds of meters or even kilometres.

3.3   Radiometry in SAR Mosaicking

No simultaneous calibration measurement were made for validation of the calibration level of the GRFM African mosaic. Removal of visible artifacts were used as an indication of the calibration revision in Paper 3.

Figure 12 shows an example of the calibration approach. There is a clear calibration artifact in the mosaic before calibration (Figure 12 a). As the look direction of the JERS SAR was from east to west, the backscatter increases with increasing range (all scenes were acquired in descending orbits). The calibration method has removed this artifact completely (Figure 12 b).

Figure 13 shows a profile computed cross the white rectangle in Figure 12. The profiles were computed summing all pixels within the rectangle along lines parallel to the orbit direction of JERS. The near-range to far-range increase in backscattering amplitude is about 1 dB (Figure 13 a).
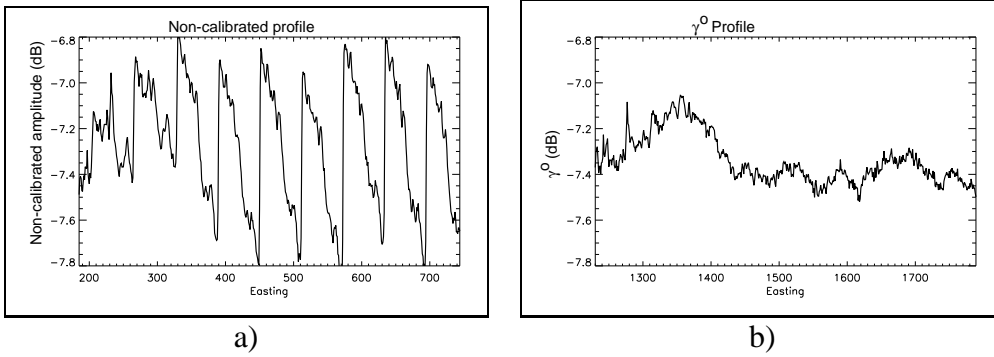
Figure 13. A range profile in the GRFM African mosaic extract before a), and after b) calibration revision (Paper 3).

The calibration has clearly removed the artifact. The remaining variation in backscattering amplitude in Figure 13 b) is due to variation in land cover type and vegetation characteristics.

In addition to the validation techniques discussed above, mosaic data can be used in computerized image analysis algorithms to evaluate the possible existence of calibration artifacts. In Paper 3, a land-cover classification was made (not by the author of this thesis) using the calibrated mosaic data. This classification (Figure 12 in Paper 3) does not show visible calibration-related artifacts, which indicates that the calibration method is suitable for producing mosaics for land-cover classification.

As with geometric accuracy, the comparison of mosaic methods in terms of radiometric accuracy is not feasible due to differences in SAR sensor, SAR processors, and available verification data for radiometric accuracy.

The radiometric methods of mosaicking that were applied in the compilation of then GRFM African mosaics can be applied to other similar SAR datasets. The assumption of stable backscattering between neighbouring scenes in the overlap areas must be valid. In SAR systems where the acquisition interval between neighbouring orbits is longer than one day the validity of this assumption can be less probable than in the case of the JERS-1 SAR system. Also higher-frequency SAR systems can have less stable backscattering as a result of changes in weather conditions.

3.4 Radar Wavelength and Polarisation in Forest Biomass Mapping

Multi-band polarimetric AIRSAR data were studied in the Freiburg study site (Papers 4 and 5). Table 4 shows the correlation coefficient between backscattering amplitude and the forest stem volume for the August 1989 scene. There were two scenes of August 1989 (1105 and 1107). Only scene 1105 is included in Table 4 because scene 1107 covered the study site only partially. Table 4 was computed using the stand-wise averaged Stokes matrices of all 230 stands of the study site except for those cases where stem volume range was limited to 0–170 m^3/ha. When computed over the whole range of stem volumes (0–830 m^3/ha) the correlation coefficients in C- and L-bands are negative. This is because the radar backscatter *vs.* stem volume relation saturates at fairly low stem volume levels in C- and L-bands as seen in Figure 14, which shows the HV-polarised backscattering amplitude as a function of forest stem volume for all AIRSAR bands. In L-band, the saturation level is somewhere between 120 and 150 m^3/ha. Figure 14 cannot be said to be in disagreement with the saturation values (130 to 157 m^3/ha) reported by Fransson and Israelsson (1999).

Even though the saturation point is somewhere between 120 and 150 m^3/ha, the backscattering amplitude does not drop rapidly after the saturation point. Fairly high linear correlation coefficients can be obtained up to about 170 m^3/ha. When including only those stands where the stem volume is 170 m^3/ha or less, the L-band correlation coefficients turn positive and the magnitude increases to about 0.45. The highest correlation coefficient (0.73) between backscattering amplitude and stem volume was obtained using P-band HV-polarised data.

Estimation RMSE was computed in Paper 4 for those regression models whose correlation coefficient was larger than 0.40. In the L-band analysis of the 0–170 m^3/ha stem volume range, the dataset included only 72 stands. The RMSE was estimated from the same dataset that was used for the development of the regression model. The RMSE values were 41.7, 40.9, and 42.5 m^3/ha for the HV, HH, and VV models, respectively. The 0–830 m^3/ha dataset that was used for the P-band model included 230 stands. This dataset was split in two equally sized subsets, one for model development and one for computing an estimation RMSE. For P-band HV-polarisation data, the estimation RMSE was 141.7 m^3/ha (in a data set where the forest stem volume varied between 0 and 830 m^3/ha).

The correlation coefficients in P-band (0.73, 0.31, and 0.21 in HV-, HH-, and VV-polarisations, respectively) are lower than those obtained by Le Toan *et al.* (1991) in a French study site (R^2 values of 0.95, 0.90, and 0.88). Two reasons have probably contributed to the lower correlations in the Freiburg study site:

1. Species composition: in the French study site, pine is practically the only tree species in evenly-aged stands whereas the forest in the Freiburg study site includes spruce, fir, pine, and some deciduous species. The age distribution within a stand is also wide in the Freiburg study site.

2. The 8-year old forest inventory data in the Freiburg study site may have lowered the correlation coefficients.

Table 4. Correlation coefficient between AIRSAR backscattering amplitude and forest stem volume for C-, L-, and P-bands in various polarisations in the Freiburg study site. The AIRSAR data were acquired in August 1989 (scene 1105). The number of observations (stands) was 230 for the stem volume range 0-830 and 72 for the range 0-170 (Paper 4).

| Band and polarisation	Stem volume (m³/ha)	Correlation coefficient
C-HV	0-830	-0.37
C-HH	0-830	-0.33
C-VV	0-830	-0.06
L-HV	0-830	-0.19
L-HV	0-170	0.47
L-HH	0-170	0.50
L-VV	0-170	0.43
P-HV	0-830	0.73
P-HH	0-830	0.31
P-VV	0-830	0.21
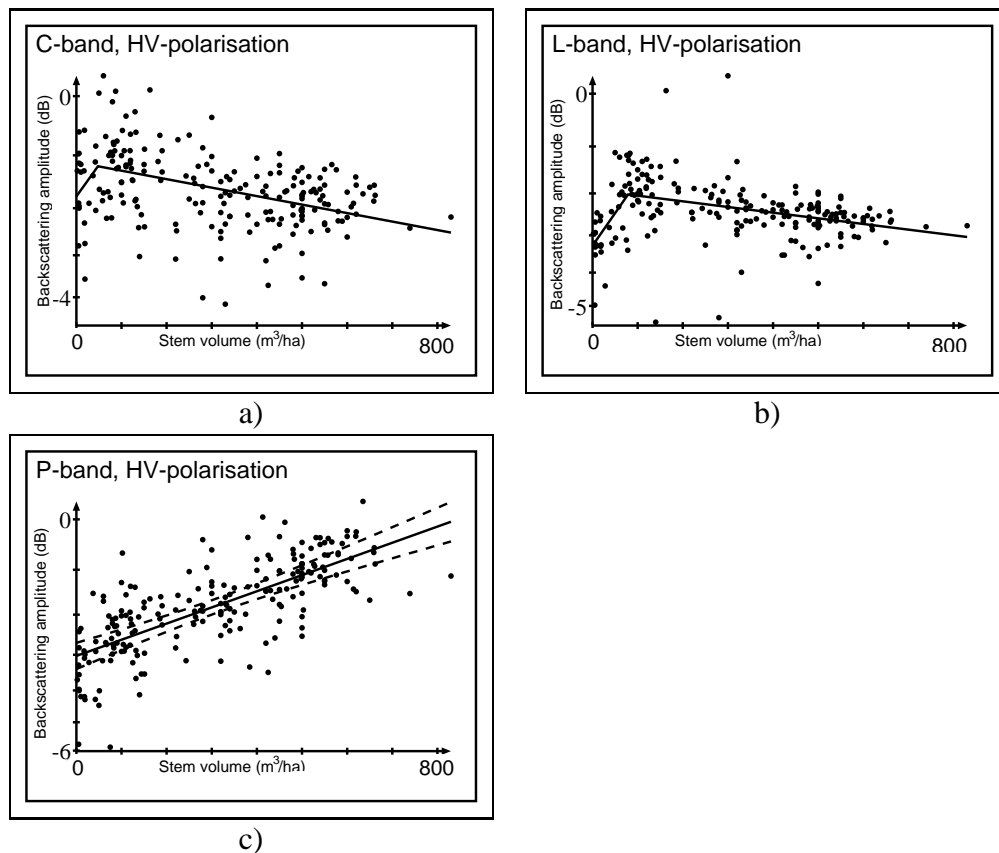
Figure 14. AIRSAR HV-polarised backscattering amplitude as a function of forest stem volume in the Freiburg study site: a) C-band, b) L-band, c) P-band. The 99 percent confidence limits of the regression function are shown as dashed lines for the P-band regression function. The AIRSAR data were acquired in August 1989 (scene 1105, Paper 4).

The search for optimal polarisation for stem volume mapping was conducted separately for each radar band in the 4-dimensional space of polarisation combinations using the search method described in section 2.2.3. The optimal polarisation combination was always at, or close to, the original linear polarisations measured by the radar (HH, HV, VV, VH).

Figure 15 shows the correlation coefficient between the backscattering amplitude and forest stem volume as a function of polarisation combination. Two sub-spaces of the 4-dimensional space of polarisation combinations are shown (in Figure 15): the co-polarised (receive orientation equals transmit orientation, receive ellipticity equals transmit ellipticity) and the cross-polarised (receive orientation is orthogonal to transmit orientation, receive ellipticity is the transmit ellipticity multiplied by -1). In Figure 15 a and b, only those stands were included where stem volume is 170 m^3/ha or lower.

In L-band, the correlation coefficient between backscattering amplitude and stem volume varied very little with the polarisation combination (Figure 15 a and b). In P-band, on the other hand, the correlation has a strong and narrow peak at HV- and VH-polarisations, while the rest of the co-polarisation and cross-polarisation sub-spaces are in the 0.3 to 0.4 range.
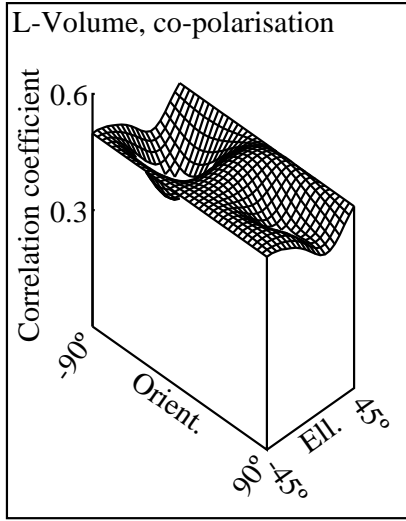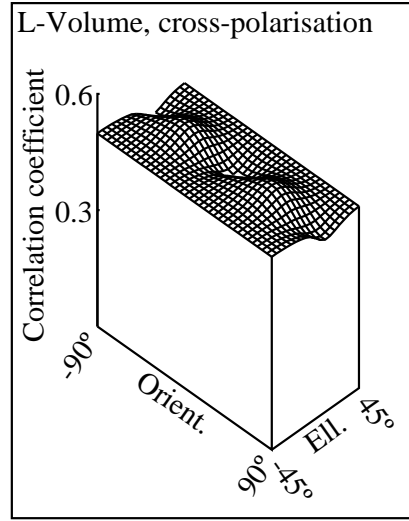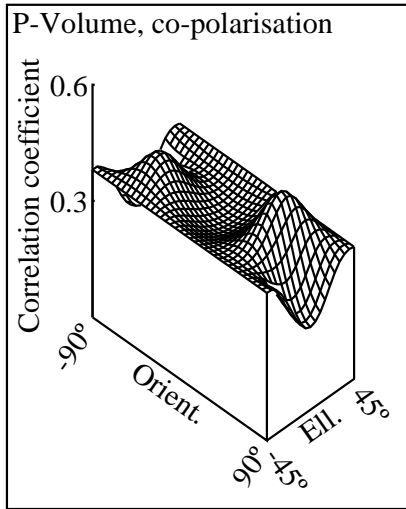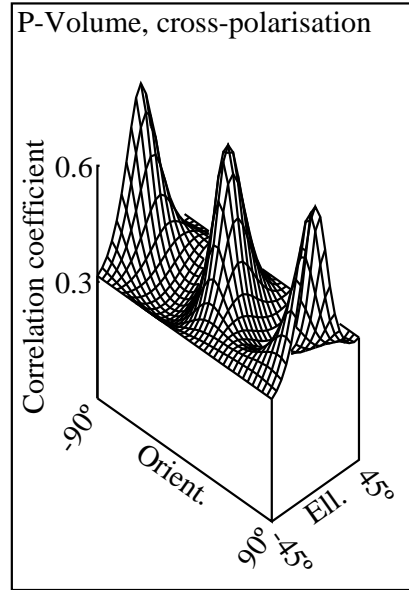
Figure 15. Correlation coefficient between backscattering amplitude and forest stem volume as a function of polarisation combination for AIRSAR data (August 1989, scene 1105) in the Freiburg study site: a) L-band, co-polarisation, b) L-band, cross-polarisation, c) P-band, co-polarisation, and d) P-band, cross-polarisation. In the L-band figures, only those stands were included where stem volume is 170 m³/ha or lower. Number of observations (stands) was 230 in P-band and 72 in L-band (Paper 4).
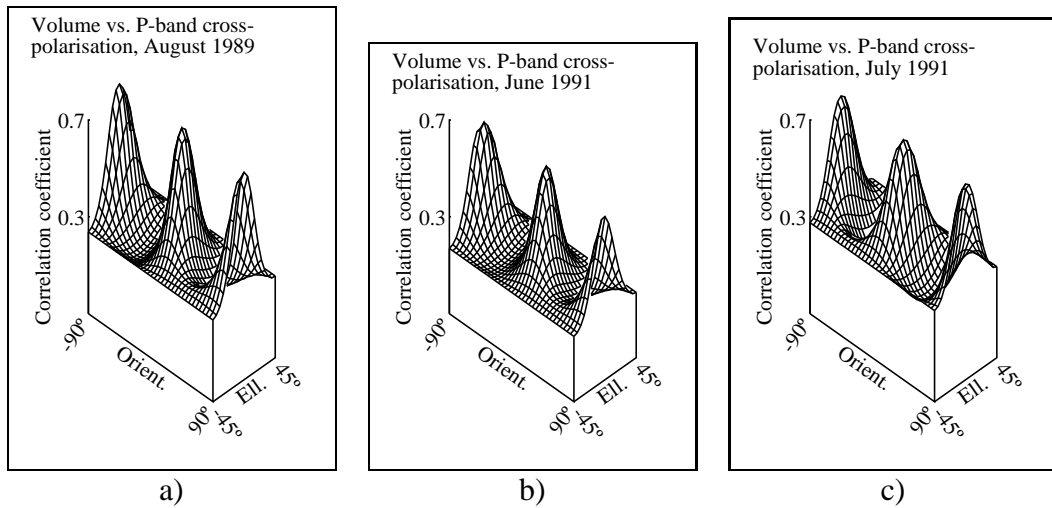
Figure 16. Correlation coefficient between backscattering amplitude and forest stem volume as a function of polarisation combination for P-band AIRSAR data in the Freiburg study site: a) August 1989 (scene 1105), b) June 1991, and c) July 1991. Only stands of 1 ha or larger were included. The number of observations (stands) was 182, 176, and 179 for August 1989, June 1991, and July 1991, respectively (Paper 5).

The temporal stability of the relation between stem volume and radar backscatter was also studied in the Freiburg study site (Paper 5). Figure 16 (Paper 5) shows the correlation coefficient between the P-band backscattering amplitude and forest stem volume as a function of polarisation combination for three dates:

a) August 1989,

b) June 1991, and

c) July 1991.

All sub-figures of Figure 16 correspond to the same cross-polarised subspace of the 4-dimensional space of polarisation combinations as Figure 15 d). Figure 16 a) was computed from the same data as Figure 15 d), but only stands of 1 ha or larger were included in Figure 16. As can be seen in Figure 16 a) to c), the relation between the stem volume *vs.* backscattering amplitude is fairly constant over time. The corresponding correlation surfaces of C- and L-bands have a lower level of the correlation coefficient and irregular shape. This is in agreement with the observation by Dobson

et al. (1991) that rain shower had the weakest effect on P-band (out of C-, L-, and P-bands).

Table 5 illustrates the development of the correlation coefficients between stem volume and backscattering amplitude for AIRSAR C- and L-band data. As the C-band saturation limit is about 60 m^3/ha and the L-band limit somewhere between 120 and 150 m^3/ha, 100 m^3/ha has been used in Table 5 as compromise between these two values. This choice also allowed the C-band dataset to include more stands than a limit of 60 m^3/ha. Only stands of 1 ha or larger were included in Table 5. The number of such stands varied between 35 and 37. The C-band correlation coefficients varied widely except in VV-polarisation. The L-band correlations were constantly between 0.5 and 0.7.

Table 5. Correlation coefficient between AIRSAR backscattering amplitude and forest stem volume for C- and L-bands in various polarisations in the Freiburg study site in three acquisition times. Only stands of 1 ha or lager with stem volumes 100 m^3/ha or less were included. The number of observations (stands) was between 35 and 37 (Paper 5).

Scene	Band	Correlation coefficient		
		HH	VV	HV
August 1989	C	0.315	0.575	0.215
June 1991	C	0.107	0.631	0.491
July 1991	C	-0.062	0.667	0.386
August 1989	L	0.539	0.674	0.671
June 1991	L	0.635	0.584	0.637
July 1991	L	0.684	0.679	0.699

In addition to the stability of of the relation between stem volume and radar backscatter, the temporal stability of the backscattering was also studied in Paper 5. As the meteorological and soil moisture data were limited, no conclusions could be drawn on the reasons of changes in backscatter between image acquisition times.

In Figure 17, forest stem volume is plotted against the estimated stem volume using AIRSAR P-band HV-polarised data from three dates. The model of the regression function was of the form:

$$V = ax_1 + bx_2 + cx_3 + d \ (\ + \epsilon \ ) \tag{57}$$
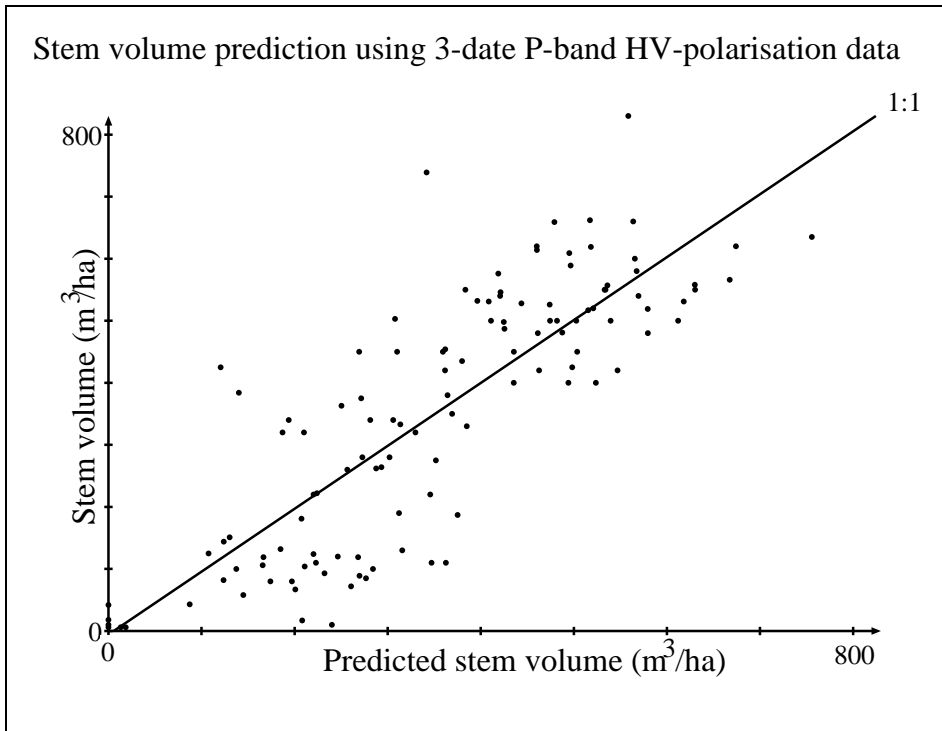
Figure 17. Multi-date regression analysis results for forest stem volume using AIRSAR P-band HV-polarised data in the Freiburg study site. The number of observations (stands) was 120 (Paper 5).

where
V	=	forest stem volume
x_1	=	backscattering amplitude in the August 1989 scene (1105),
x_2	=	backscattering amplitude in the June 1991 scene,
x_2	=	backscattering amplitude in the July 1991 scene,
$a, b, c,$ and d	=	regression coefficients, and
ϵ	=	random error.

The multiple correlation coefficient (the correlation coefficient between the predicted stem volume and the true stem volume) was 0.82, which is higher than any of the single-date correlations (0.79, 0.60, and 0.75). Only stands of 2 ha or larger were included in this multiple regression model (120 observations).

76
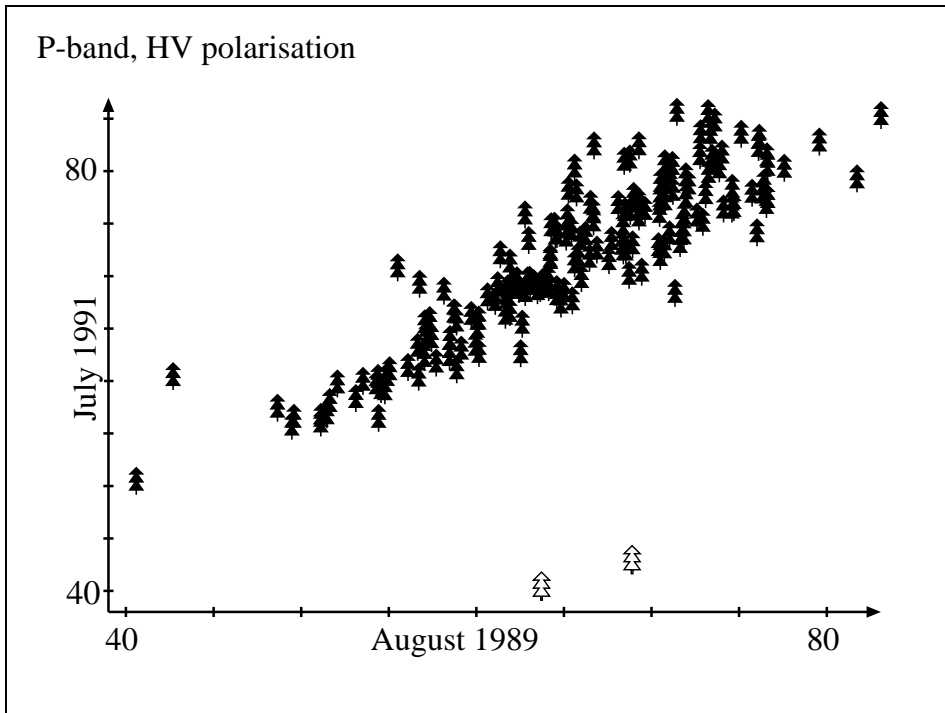
Figure 18. Change detection in the Freiburg study site using stand-wise AIRSAR P-band HV data. Backscattering amplitude of August 1989 (scene 1105) is shown on the horizontal axis and the backscattering amplitude of July 1991 on the vertical axis. The number of observations was 179. The filled symbols are forest stands that were not clear-cut between 1989 and 1991. The two outlined symbols are stands that were clear-cut between August 1989 and July 1991 (Paper 5).

Figure 18 shows a change detection example using AIRSAR P-band HV-polarised data. The figure shows the stand-wise backscattering amplitude of July 1991 plotted against the backscattering amplitude of August 1989. The two stands (open symbols) that have been logged between image acquisitions are clearly separable from other stands.

3.5 Multi-Temporal L-Band Radar Backscatter in Forest Biomass Mapping

Multi-temporal L-band JERS SAR data were studied in the Ruokolahti study site. Table 6 shows single-date regression results for the six SAR scenes that were available (Paper 6). Columns A and B give the slope and intercept of a linear regression model of the form:

$$V = A \cdot r_c + B \left(+ \epsilon \right) \tag{58}$$

where V is forest stem volume (m^3/ha), r_c is backscattering amplitude corrected for topography (relative to the σ^o calibration factor 68.2 dB, $\sigma^o = 10 \cdot log(r_c^2) - 68.2$ dB, all scenes were scaled to this calibration standard before regression analyses), and ϵ is random error. Column RMSE gives the the root mean square error of the estimated forest stem volume. The RMSE values of Table 6 were computed using the leave-one-out method.

The correlation coefficient is highest (0.63 to 0.81) for the summer scenes. One of the winter scenes (Wet95Jan), had also a correlation coefficient similar to those of the summer scenes. This was a scene acquired in conditions where a layer of moist new snow was present on top of older snow layers, which also were thawed. The other two winter scenes, which were acquired in cold and dry conditions, had low correlations. This is in agreement with the observation by Santoro *et al.* (2004) that frozen conditions were least suitable for forest biomass retrieval.

The level of the summer-time correlation coefficients and the scene Wet95Jan in Table 6 is in agreement with the correlation coefficients of Askne *et al.* (2003) who found the correlation coefficients to be generally of the order of 0.8. The RMSE values of Table 6 are generally lower than the RMSE values of single-date JERS SAR results (69.5–140.1 m^3/ha) in Askne *et al.* (2003) even though the RMSE values in Table 6 have not been corrected for uncertainty of the ground data. The main reason for this is most likely the lower average stem volume in the Ruokolahti study site (100 m^3/ha) compared to that in the Kättböle study site (140 m^3/ha).

Summer Scenes   As the summer-time response of L-band backscattering amplitude to forest stem volume is stable from scene to scene, a general L-band model was proposed in Paper 6 for approximative mapping of forest stem volume and biomass. The general function was computed from the three summer scenes combined, leaving out clear-cut areas. The function

Table 6. Correlation coefficients (r) and parameters of linear regression functions (A = slope, B = intercept) between forest stem volume and JERS backscattering amplitude at various times of the year in the Ruokolahti study site. The RMSE was computed using the leave-one-out method. There were 206 observations in all six cases. The regression was significant at 5 % confidence level in all cases except the Dry98Mar. See section 2.1.4 for scene identifiers (Paper 6).

Scene	A	B	r	RMSE (m^3/ha)
S95Jul	0.60	-562	0.81	44.79
S95Sep	0.72	-743	0.70	56.18
S95Oct	0.87	-894	0.63	61.25
Dry93Feb	3.22	-3239	0.40	72.93
Wet95Jan	0.71	-560	0.78	49.22
Dry98Mar	-30.33	26896	-0.05	79.27

was derived from Equation (58):

$$V = 0.65 \cdot r_c - 634 \tag{59}$$

or

$$V = 0.65\sqrt{10^{(\sigma^o+68.2)/10}} - 634 \tag{60}$$

where V is forest stem volume in m^3/ha and r_c is L-band backscattering amplitude (relative to calibration factor 68.2 dB). This function is valid for VV-polarised L-band radar scenes (with a nominal incidence angle of about 39°) that are acquired in summer conditions similar to the conditions of the three scenes used in Paper 6 (i.e., no heavy rain in the weeks preceding radar data acquisition).

In Paper 1, forest stem volume was correlated against L-band Seasat backscattering amplitude that had not been corrected for topography effects. The very low correlation coefficient (0.05) shows that stem volume mapping is not feasible without terrain corrections in a hilly or mountainous area. One reason why forest stem volume estimation was not attempted in Paper 1 after radiometric correction of terrain effects (as done in Paper 6) was the coarse ground data and DEM. Another reason was the poor (Landsat derived) stem volume data in the Arjeplog site.

The summer-time correlations in Table 6 (0.81, 0.70, and 0.63) are slightly higher than the correlations obtained for young stands in the Freiburg study

site using AIRSAR L-band HH-polarised data (0.54, 0.64, and 0.68, Table 5). The reasons for the slight difference can be:

- less accurate ground data in the Freiburg study site (8- or 10-years old inventory in an area where forest growth is fast) than in the Ruokolahti study site (2-year time difference between forest inventory and SAR image acquisition in 1995), and

- a narrower range of stem volumes (restricted to stands with 0 to 100 m^3/ha) in the Freiburg study site than in the Ruokolahti study site (stands with 0 to 364 m^3/ha), which tends to lead to lower correlation coefficients in regression analysis; correlation coefficients in scenes S95Jul, S95Sep, and S95Oct were 0.78, 0.62, and 0.45, respectively, when computing over the 95 stands with stem volume of 100 m^3/ha or less.

Differences in tree species composition, understory, and soil conditions may also have contributed to the differences on correlation coefficients between the Freiburg and Ruokolahti study sites.

Figure 19 shows regression functions and stand-wise observations between backscattering amplitude and forest stem volume for all six scenes. In addition to similar correlation coefficients, the linear regression functions are also similar between all summer scenes.

Winter Scenes   In the dry winter scenes (Figure 19), the average backscatter is about 2 dB lower than in the summer scenes. This is in agreement with the well known phenomenon of backscatter drop when the forest canopy freezes. Kwok *et al.* (1994) observed a drop of 3 dB in L-band HH-polarised data when the forest canopy and ground froze. Ranson and Sun (2000) reported a difference of about 2.5 dB between the frozen and thawed state in non-water areas. Santoro *et al.* (2004) found an increase of approximately 4 dB in spring when the forest went from frozen winter conditions to snow-free summer conditions. Santoro *et al.* (2004) mentioned that the calibration error was 1–2 dB.

The dry winter scenes are almost uncorrelated with stem volume. One explanation of this could be that the forest canopy – in areas with average stem volume of about 100 m^3/ha – in a frozen state is almost transparent to L-band radar, and therefore the ground backscattering dominates the radar image.
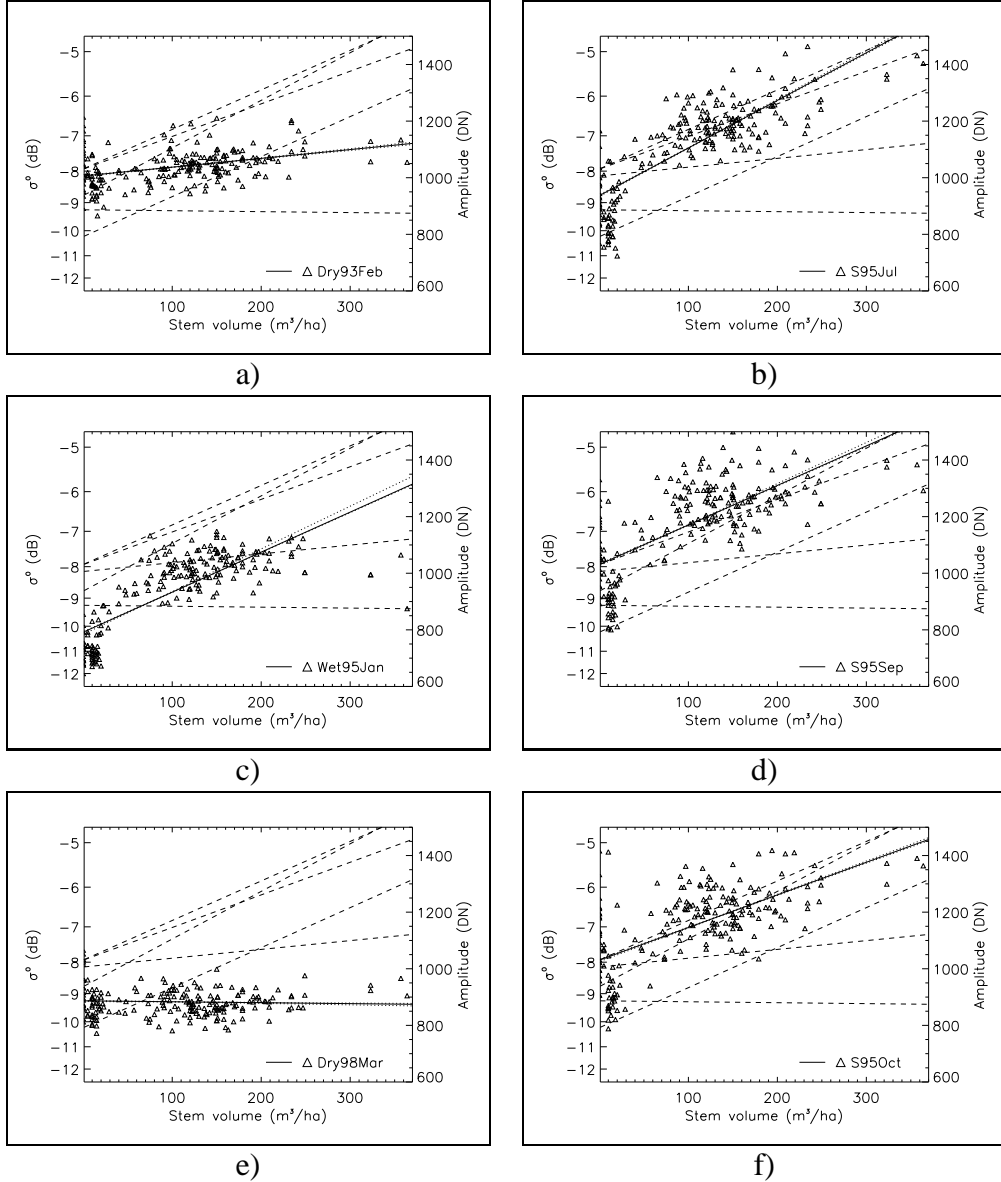
Figure 19. Regression functions between JERS backscattering amplitude and forest stem volume for winter (left) and summer (right) scenes in the Ruokolahti study site. The solid line shows the regression line computed for the observation data in the diagram. The dashed lines show the regression lines for the other five scenes. The dotted lines around the solid line show the variation of the regression function in the leave-one-out testing method (Paper 6).
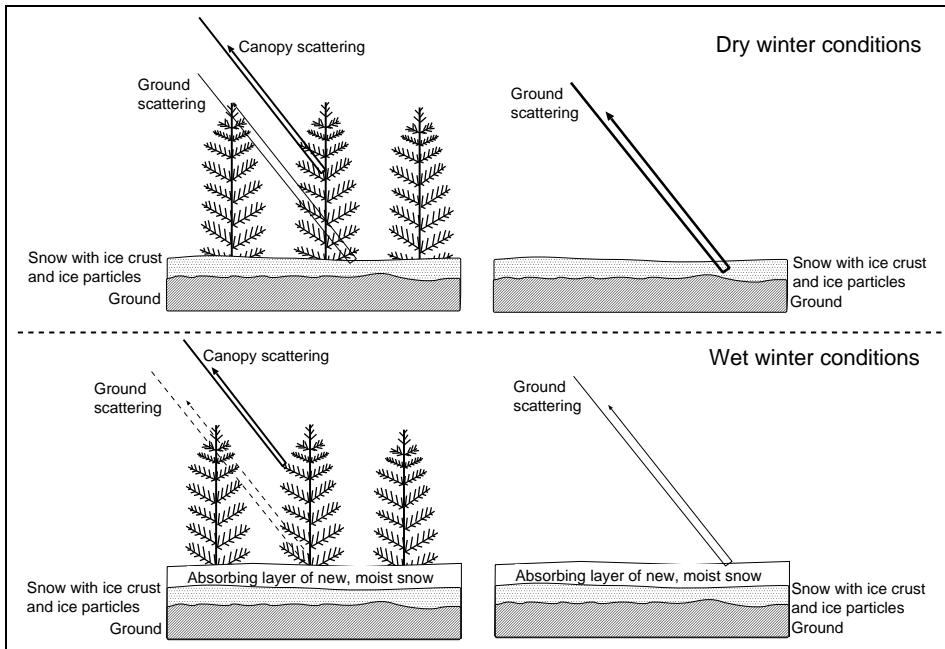
Figure 20. Forest and clear-cut backscatter (schematically) in dry and wet winter conditions (Paper 6).

The wet winter scene Wet95Jan (Figure 19) has a regression function with a similar slope to those of the summer scenes, but the backscatter level is about 2 dB lower than in the summer scenes. This can be an indication that forest canopy and soil included very small amount of liquid water during the acquisition of the scene Wet95Jan, when the temperature had risen to about 0 C in January. The scene Wet95Jan also discriminates well between clear-cut areas and forested areas.

Figure 20 shows a possible explanation for the high correlation coefficient between backscattering amplitude and forest stem volume in wet winter conditions. In dry, frozen winter conditions, the backscatter from the forest canopy is not notably higher than the backscatter from open areas – from the ice particles in the snow pack and from stones and other scattering sources under the snow. If a wet snow layer absorbs the backscatter from ground and lower snow pack, open area backscatter becomes very low. The backscatter from the forest canopy may increase if the liquid water contents of canopy components increases. This increases the correlation coefficient between backscattering amplitude and forest stem volume and also increases the separation between open and forested areas.

Multi-Date Regression Analysis   Multiple linear regression analyses (dependent variable forest stem volume, independent variables six JERS SAR scenes) were made in a series varying the stem volume range included in the dataset (Paper 6). Table 7 shows the results of these regression analyses. Column 'R^2' gives the coefficient of variation. Columns '$R^2_{A_1}$' to '$R^2_{A_3}$' give the adjusted R^2 as computed using Equations (54) to (56). Column 'RMSE' gives the root mean square error of the multiple linear regression model as computed by the leave one out method. The column 'RelE' gives the RMSE as a percentage of the width of the forest stem volume range included in the analysis.

Table 7. Multiple regression analysis results as a function of forest stem volume range. The dependent variable was forest stem volume. The independent variables were the six JERS scenes (1 = Dry93Feb, 2 = Wet95Jan, 3 = S95Jul, 4 = S95Sep, 5 = S95Oct, 6 = Dry98Mar). RelE = relative RMSE = RMSE/(Vol_{max} - Vol_{min}). S = significant at 5 % risk level, - = not significant (Paper 6).

Vol-Rg	n	R^2	$R^2_{A_1}$ eq 54	$R^2_{A_2}$ eq 55	$R^2_{A_3}$ eq 56	RMSE (m^3/ha)	RelE (%)	1	2	3	4	5	6
0-360	206	0.71	0.70	0.70	0.70	42.8	11.7	S	S	S	-	-	S
50-360	139	0.37	0.34	0.35	0.34	47.2	15.0	S	-	S	-	-	-
100-360	112	0.35	0.31	0.32	0.31	44.8	16.9	S	-	S	-	-	-
150-360	59	0.43	0.37	0.38	0.36	44.6	20.7	-	S	S	-	-	-
200-360	19	0.53	0.33	0.35	0.30	68.8	41.7	-	-	-	-	-	-
0-300	202	0.77	0.76	0.76	0.76	35.2	11.7	S	S	S	-	-	S
0-250	202	0.77	0.76	0.76	0.76	35.2	14.1	S	S	S	-	-	S
0-200	187	0.79	0.78	0.78	0.78	30.1	15.0	-	S	S	-	-	S
0-150	152	0.83	0.82	0.82	0.82	22.9	15.3	-	S	S	-	-	S
0-100	95	0.83	0.82	0.82	0.82	15.5	15.5	-	S	-	-	-	S
0-50	67	0.64	0.61	0.61	0.60	7.6	15.2	-	S	-	-	-	S

In the first set of cases (the upper end of the stem volume range, increasing the lower bound of the range), the coefficient of determination decreases with decreasing range of stem volumes (and decreasing number of stands). The number of significant variables also decreases – the last case with only 19 stands makes the whole regression insignificant at 5 percent significance level. The RMSE increases with decreasing range of stem volumes. Only one (S95Jul) summer scene out of three is significant. This is because sumer scenes are highly correlated among themselves.

In the second set of cases (the lower end of the stem volume range, decreasing the upper bound of the range), the coefficient of determination increases with decreasing range of stem volumes (and decreasing number of stands) until 0–150 or 0–100 m³/ha. In other words, the highest coefficient of determination (in the lower range of stem volumes) is obtained when including data below the saturation zone only. The RMSE decreases with decreasing range of stem volumes. Also in this set of cases, the scene S95Jul is the only summer scene with a significant contribution to the regression.

A two-piece multi-temporal stem volume estimator was derived from the multiple regression analyses. This estimator is a combination of two multiple linear regression models having three independent variables:

W = backscattering amplitude in the wet winter scene, Wet95Jan,

D = backscattering amplitude in the dry winter scene, Dry98Mar, and

S = average backscattering amplitude in the three summer scenes (S95Jul, S95Sep, and S95Oct).

The two piece-wise estimates are (e_L for the lower stem volume range, e_H for the upper stem volume range):

$$e_L = -118.8 + 0.243 \cdot W - 0.056 \cdot D \tag{61}$$

and

$$e_H = -174.9 + 0.183 \cdot W - 0.239 \cdot D + 0.273 \cdot S. \tag{62}$$

The combined estimate is computed:

$$
\begin{aligned}
\text{if } e_H > 120: \quad e &= e_H \\
\text{if } e_H < 80: \quad e &= e_L \\
\text{if } e_H \geq 80 \text{ and } e_H \leq 120: \quad e &= \frac{120 - e_H}{40} e_L + \frac{e_H - 80}{40} e_H.
\end{aligned}
\tag{63}
$$

It was decided to split the forest stem volume range at 100 m³/ha and not at 150 m³/ha which is closer to the saturation point of L-band backscattering amplitude. This decision, which was based on experimentation, aimed at stronger correlation in the lower stem volume range. The regression coefficients of the upper stem volume range were determined using the whole stem volume range of 0–360 because the function for the upper
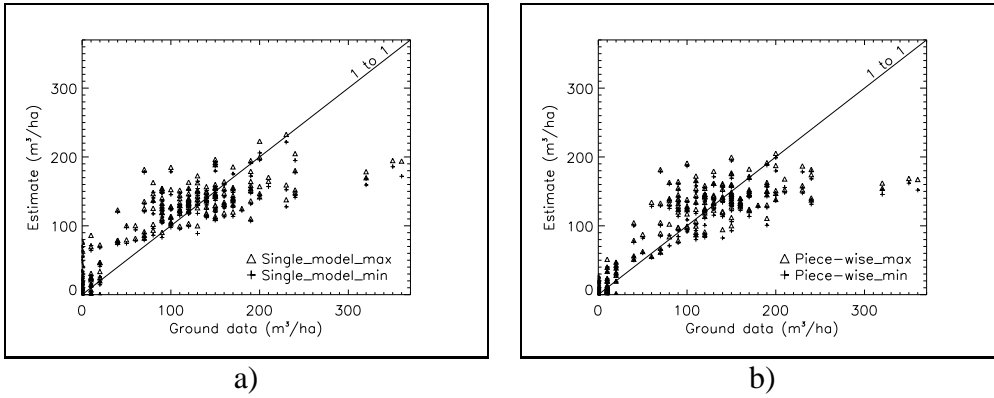
Figure 21. Estimated stem volume for multi-date regression models in the Ruoko-lahti study site. All six JERS SAR scenes were used as independent variables of a linear model in a). The 2-piece model (see section 3.5) was used in b). There were 208 observations in both cases. A triangle marks the maximum estimated stem volume in the leave-one-out method. A plus sign marks the corresponding minimum estimate.

stem volume range was used to select between the pieces of the two-piece estimator. All regression coefficients in Equations (61) and (62) were significant at 5 percent risk level.

Figure 21 shows the estimated *vs.* true forest stem volume for a 6-date lin-ear multiple regression model (a) and the 2-piece model described above. Both models had very similar RMSE figures (41.3 m^3/ha for 6-date lin-ear, 41.6 m^3/ha for the 2-piece model) as estimated by the leave-one-out method. The 2-piece model, which depends more on the wet winter scene, reduces the bias at the lower end of the forest stem volume range. The RMSE value (41.3 m^3/ha) of the six-date estimation is lower than the RMSE obtained by Askne *et al.* (2003) in the Kättböle study site with nine-date JERS backscatter data (36.4 or 59.0 m^3/ha, depending on the selection of training and test datasets) when taking into account that no uncertainty figures for ground data has been subtracted from the RMSE value in the Ruokolahti site. If a similar reduction was made in the RMSE value of the Ruokolahti study site, it would be about on the level (27.2–38.0 m^3/ha) of the RMSE of the model that used three backscatter observations and one coherence observation in Askne *et al.* (2003). The reason for smaller RMSE values in the Ruokolahti study site is most likely the lower mean stem volume in Ruokolahti.

In addition to the two-piece estimator of Equations (61) and (62), another
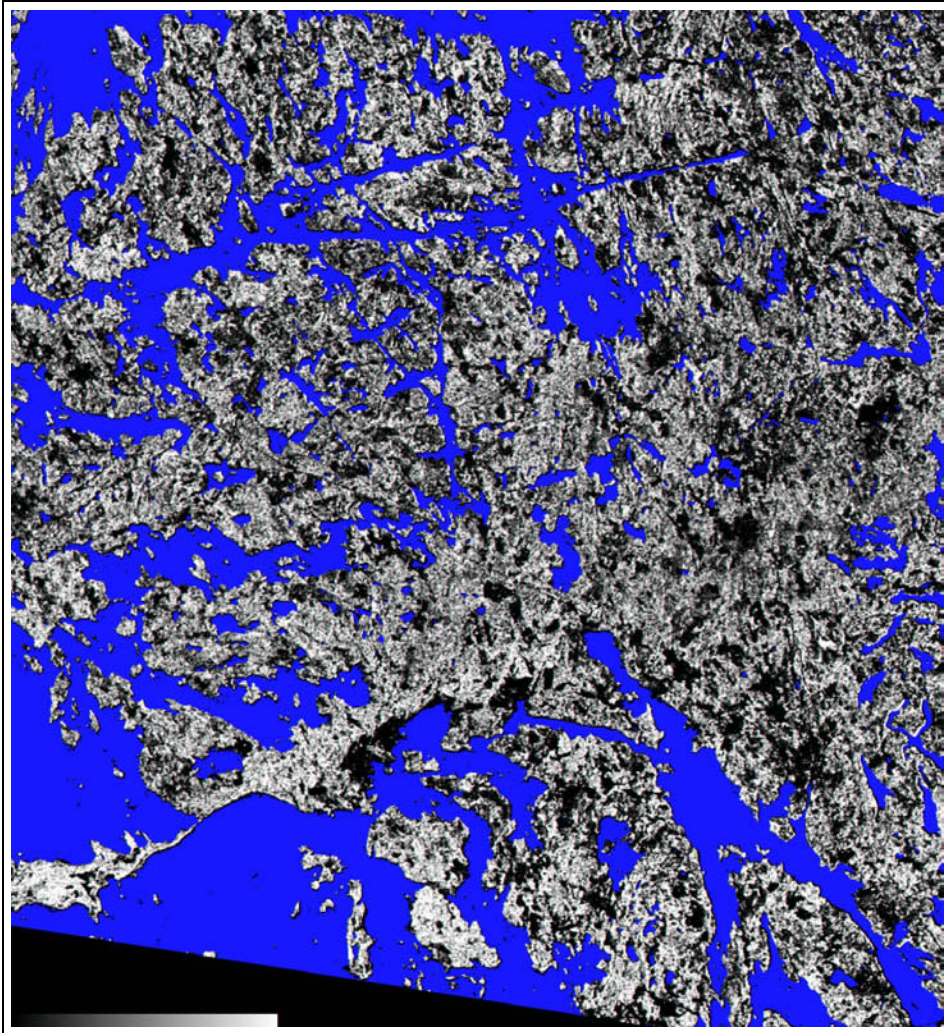
Figure 22. JERS-estimated forest stem volume for a 38 km by 38 km area in the Ruokolahti-Puumala region. Black corresponds to a stem volume of 0 m^3/ha and white to 200 m^3/ha. Compact blue is water. For a colour version, see the front cover of this publication (Paper 6).

estimator was derived using those original scenes (not the averaged summer scene) that produced significant regression coefficients. The upper stem volume range model was determined using only data from the stem volume range of its validity, not over the whole range 0–360 m^3/ha. This estimator produced a better correlation coefficient between the estimated and ground-measured forest stem volume and also a smaller RMSE[2]. This model was abandoned because it produced very poor estimates outside the area of the stands that were used in its derivation.

Figure 22 shows the combined multi-temporal stem volume estimate (two-piece estimate, Equations 61 and 62) computed over an area of 38 km by 38 km around the Ruokolahti study site.

---

[2]It appears that the RMSE figure of the 2-piece model that was reported in Paper 6 (28.5 m^3/ha) was computed using this model, not the one described by Equations (61) and (62). This was an error in Paper 6.

4 Summary of Papers and Contribution

In Paper 1, the incidence angle effects due to local topography on L-band Seasat SAR data in a forested area were analyzed using a digital elevation model. Topographic effects accounted for over 60 percent of the total variation in the L-band Seasat SAR scene in a hilly and mountainous study site in northern Sweden. The most important topographic factor was the size of the resolution cell, which varies with varying incidence angle components. This was the first study where topographic effects – in the form of the size of a resolution cell – were analysed in quantitative terms in a large study site in boreal forest.

In Paper 2, a methodology for the revision of the geometry of SAR scenes for mosaicking multi-temporal sets of SAR scenes was presented. JERS scenes of the GRFM African mosaic were used as SAR data. Sub-pixel internal consistency of the mosaic was obtained. Absolute geometric accuracy was estimated to be within a few hundred meters. This was the first time that a rigorous least squares adjustment was applied to a multi-temporal SAR mosaic dataset of over 3000 scenes. Error ellipses were used to evaluate the spatial distribution of the uncertainty in scene locations.

In Paper 3, the geometric mosaicking method was described in more detail. A methodology for improving the calibration of SAR scenes when a large number of scenes are mosaicked was also presented. The same set of JERS SAR scenes was used as SAR data as in Paper 2. The calibration artifacts before the calibration revision were about 1 dB or even higher. The calibration revision method produced mosaics that enabled image analysis without scene boundary effects.

In Paper 4, the characteristics of various radar wavelengths and polarisations were analysed in mapping forest biomass. AIRSAR data were used in a German study site. A systematic method was presented to find the optimal combination of transmit and receive polarisations for forest biomass mapping. The method uses stand-wise averaged Stokes matrix data and a polarisation synthesis algorithm. This method maximises the correlation coefficient between forest stem volume and SAR backscattering amplitude. P-band HV-polarisation was the optimal single radar dataset in mapping forest stem volume. In stands with stem volumes less than 170 m^3/ha, L-band also had a strong correlation between stem volume and backscattering amplitude. Paper 4 was the first study where optimal polarisation was systematically analysed – using the correlation

coefficient between forest stem volume and backscattering amplitude – over the whole transmit-receive polarisation space in a dataset of over 200 conifer-dominated forest stands.

Paper 5 extended the wavelength-polarisation analysis of Paper 4 to a multi-temporal AIRSAR dataset. In P-band, the HV-polarisation was the optimal single radar dataset in all three scenes acquired in August 1989, June 1991, and July 1991. The form of the correlation surface (between forest stem volume and backscattering amplitude) in the P-band cross-polarised sub-space was also similar from scene to scene. Also in L-band, the correlation coefficients between forest stem volume and backscattering amplitude were almost constant from scene to scene when the analysis was restricted to stands with stem volumes less than 100 m^3/ha. In C-band, the stem volume correlations varied from scene to scene in HH- and HV-polarisations.

In Paper 6, a multi-temporal JERS SAR dataset was studied in a site in south-eastern Finland. The dataset included three scenes acquired in summer (July to October), two scenes acquired in freezing winter conditions, and one scene in winter conditions with a moist new snow layer on top of old snow. The forest inventory ground data included 206 stands of boreal forest. In the JERS SAR scenes that were acquired in freezing winter conditions the correlation between stem volume and backscattering amplitude was low. The relation between forest stem volume and backscattering amplitude was so similar in summer scenes that one regression model could be proposed for forest stem volume mapping in wide areas if accuracy requirements are not high.

5   Conclusions

An optimal tool – among weather independent microwave sensors – for space-borne forest biomass mapping is a P-band HV-polarised SAR. This is due to its strong relation with forest biomass as shown in Paper 4 and the literature (*e.g.,* Le Toan *et al.* 1991). The P-band relation with forest biomass is also sTable as shown in Paper 5.

In the absence of a space-borne P-band SAR in the foreseeable future, summer-time L-band SAR data can be used for approximate forest biomass mapping in areas where biomass is not very high, *e.g.,* in the northern part of the boreal forest zone. The L-band has a stable relation with forest biomass in areas with fairly low biomass as shown in Papers 5 and 6. This stability of the relation between L-band backscattering amplitude and forest biomass was observed in a dataset that only included SAR scenes acquired in fairly dry conditions. The L-band biomass mapping – using the biomass function derived in Paper 6 – may require that SAR scenes are not degraded by excessive amounts of rain that could decrease the contrast between high and low biomass areas. The results of Conway & Estreguil (1994) and Keil *et al.* (1994) suggests that rain has an impact on the contrast between open and forested areas in C-band SAR data. The relation between L-band backscattering amplitude and forest biomass in rainy SAR scenes was not studied in Paper 6 because the dataset did not include scenes acquired in very rainy conditions.

L-band forest biomass mapping in wide areas requires accurate mosaicking of a large number of SAR scenes. This can be achieved using geometry revision techniques like that described in Paper 2. Application of forest biomass estimation models to a mosaic of SAR data requires good relative calibration from scene to scene. Such calibration can be obtained by calibration revision techniques, for example the technique that was described in Paper 3.

In all forest biomass mapping using SAR backscattering amplitude, the effects of terrain topography must be corrected from the SAR scenes before forest biomass estimation models are used. Terrain topography can account for more than 60 percent of the variation in SAR backscattering amplitude in hilly forested areas as shown in Paper 1.

6   Future Research

The future space-borne SAR systems – especially the Japanese ALOS PALSAR, which operates in L-band – will enhance the potential for wide area forest biomass mapping. The results of Paper 6 suggest that the derived biomass function can be used in forest biomass mapping in wide boreal forest areas with L-band HH-polarised SAR. As these results were verified in a single study site, the biomass function should be validated in a larger set of study sites with wider variation in forest types and forest management practices.

Polarimetric interferometry has been proposed for forest biomass mapping. As this technique requires fully polarimetric data acquisitions, the technique may turn out too demanding in terms of data acquisition and area coverage. In fully polarimetric mode, the SAR sensors of the near future have an image swath width that is only half of the nominal single-polarisation swath. The so called dual-polarisation configuration, which includes simultaneous HH- and HV-polarised data, covers the whole swath of the single-polarisation mode. Therefore, the use of HV-polarisation – alone or in addition to the HH-polarised data – is a central research topic in the coming years.

The forest biomass function derived in Paper 6 is valid in forested areas. Mapping of forest and non-forest land cover types should be made prior to forest biomass mapping to avoid gross errors and mis-interpretation of mapped biomass values. Even though forest area mapping has been studied for a long time reliable discrimination between forest and various non-forest land cover types is challenging in wide areas that include wide variation in climatic and topographic conditions. When forest biomass is mapped in country-wide or continent-wide areas mapping of forest and non-forest land cover types requires research on reliable and accurate methods and on earth observation data that can be used in this task.

A digital elevation model (DEM) was a key element in geometric and radiometric processing of SAR scenes in Papers 1 and 4 through 6. In all these cases, the DEM-based processing was done on single SAR scenes. In wider areas, a mosaicking process hides the growth direction of the range co-ordinate, which is essential for both geometric and radiometric DEM-based processing of SAR scenes. Use of DEMs in geometric and radiometric processing of SAR mosaics requires further research.

References

Ahern, F., Leckie, D., and Drieman, J. 1993. Seasonal changes in relative C-band backscatter of northern forest cover types, *IEEE Transactions on Geoscience and Remote Sensing*, **31(3)**, p. 668–680.

Angelis, C., Freitas, C., Dutra, L., and Valeriano, D. 2001. ERS-1 multitemporal backscatter analysis of different types of land cover in Brazilian Amazonia, Proceedings of the International Geoscience and Remote Sensing Symposium IGARSS 2001, Sydney, Australia, 9–13 July, 2001, IEEE, Piscataway, NJ, USA, Vol. 5, p. 2019–2021.

Askne, J., Santoro, M., Smith, G., and Fransson, J. 2003. Multitemporal repeat-pass SAR interferometry of boreal forests, *IEEE Transactions on Geoscience and Remote Sensing*, **41(7)**, p. 1540–1550.

Askne, J., Smith, G., and Santoro, M. 2004. L-band observations of boreal forest stem volume, Proceedings of the 23rd Symposium of the European Association of Remote Sensing Laboratories, Ghent, Belgium, 2–5 June 2003, Millpress Science Publishers, Rotterdam, the Netherlands, p. 159–165.

Balzter, H., Baker, J., Hallikainen, M., and Tomppo, E. 2002. Retrieval of timber volume and snow water equivalent over a Finnish boreal forest from airborne polarimetric synthetic aperture radar, *International Journal of Remote Sensing*, **23(16)**, p. 3185–3208.

Bayer, T., Winter, R., and Schreier, G. 1991. Terrain influences in SAR backscatter and attempts to their correction, *IEEE Transactions on Geoscience and Remote Sensing*, **29**, p. 451–462.

Castel, T., Beaudoin, A., Stach, N., Stussi, N., Le Toan, T., and Durand, P. 2001. Sensitivity of space-borne SAR data to forest parameters over sloping terrain – Theory and experiment, *International Journal of Remote Sensing*, **22(12)**, p. 2351–2376.

Castel, T., Guerra, F., Caraglio, Y., and Houllier, F. 2000. Retrieval biomass of a large Venezuelan pine plantation using JERS-1 SAR data, Proceedings of the International Geoscience and Remote Sensing Symposium IGARSS 2000, Honolulu, USA, 24–28 July, 2000, IEEE, Piscataway, NJ, USA, Vol. 1, p. 396–398.

Castel, T., Guerra, F., Caraglio, Y., and Houllier, F. 2002. Retrieval biomass of a large Venezuelan pine plantation using JERS-1 SAR data, Analysis of

forest structure on radar signature, *Remote Sensing of Environment*, **79**, p. 30–41.

Churchill, P. and Attema, E. 1991. The European airborne polarimetric SAR campaign MAESTRO 1, Proceedings of the International Geoscience and Remote Sensing Symposium IGARSS'91, Helsinki University of Technology, Espoo, Finland, 3–6 June, 1991, IEEE, Piscataway, NJ, USA, Vol. II, p. 327–328.

Conway, J. and Estreguil, C. 1994. Evaluation of multi-temporal ERS-1 SAR data for tropical forest mapping in Papua New Guinea, Proceedings of the Second ERS-1 Symposium – Space at the Service of our Environment, Hamburg, Germany, 11–14 October, 1993, ESA SP-361 (January 1994), p. 481–484.

Dobson, C., Mc Donald, K., Ulaby, F., and Sharik, T. 1991. Relating the temporal change observed by AIRSAR to surface and canopy properties of mixed conifer and hardwood forests of Northern Michigan, Proceedings of the 3rd Airborne Synthetic Aperture Radar (AIRSAR) Workshop, May 23–24, 1991, JPL Publication 91–30, p. 34–43.

Drieman, J. 1987. Evaluation of SIR-B imagery for monitoring forest depletion and regeneration in western Alberta, *Canadian Journal of Remote Sensing*, **13(1)**, p. 19–25.

ESA 1988. ERS-1 – A keen eye on the earth, ESA F12, 2nd edition, European Space Agency, the Netherlands, August 1988, 6 p.

Foody, G. 1986. An assessment of the topographic effects on SAR image tone, *Canadian Journal of Remote Sensing*, **12(1)**, p. 124–131.

Fransson, J. and Israelsson, H. 1999. Estimation of stem volume in boreal forests using ERS-1 C- and JERS-1 L-band SAR data, *International Journal of Remote Sensing*, **20(1)**, p. 123–137.

Fransson, J., Walter, F., and Ulander, L. 2000. Estimation of forest parameters using CARABAS-II VHF SAR data, *IEEE Transactions on Geoscience and Remote Sensing*, **38**, p. 720–727.

Goering, D., Chen, H., Hinzman, L., and Kane, D. 1995. Removal of terrain effects from SAR satellite imagery of arctic tundra, *IEEE Transactions on Geoscience and Remote Sensing*, **33**, p. 185–193.

Goyal, S., Seyfried, M., and O'Neill, P. 1999. Correction of surface roughness and topographic effects on airborne SAR in mountainous rangeland areas, *Remote Sensing of Environment*, **67**, p. 124–136.

Haara, A. and Korhonen, K.T. 2004. Kuvioittaisen arvioinnin luotettavuus (Reliability of stand-wise forest inventory data, in Finnish), *Metsätieteen aikakauskirja*, publ. Metsäntutkimuslaitos and Suomen Metsätieteellinen Seura, 4/2004, p. 489–508.

Haggrén, H. and Honkavaara, E. 2004. Luento 10: Topografinen peruskar-toitus, 'http://ns.foto.hut.fi/opetus/220/luennot/10/L10_2004.pdf', checked 21 October 2005.

Harrell, P., Bourgeau-Chavez, L., Kasischke, E., French, N., and Chris-tensen, N. 1995. Sensitivity of ERS-1 and JERS-1 radar data to biomass and stand structure in Alaskan Boreal forest, *Remote Sensing of Environ-ment*, **54**, p. 247–260.

Held, D., Brown, W., Freeman, A., Klein, J., Zebker, H., Sato, T., Miller, T., Nguyen, Q., and Lou, Y. 1988. The NASA/JPL multifrequency, multi-polarization airborne SAR system, Proceedings of the International Geo-science and Remote Sensing Symposium IGARSS'88, 12–16 September, Edinburgh, Scotland, UK, IEEE, Piscataway, NJ, USA, p. 345–350.

Hinse, M., Gwyn, Q., and Bonn, F. 1988. Radiometric correction of C-band imagery for topographic effects in regions of moderate relief, *IEEE Transactions on Geoscience and Remote Sensing*, **26**, p. 122–132.

Hirvonen, R. 1965. Tasoituslasku. Teknillisten tieteiden Akatemia, Helsinki, Finland, 240 p.

Hoekman, D. and Quinones, M. 1998. Land cover type and biomass clas-sifications using AirSAR data for evaluation of monitoring scenarios in the Colombian Amazon, Proceedings of the 2nd International Workshop on Retrieval of Bio- and Geophysical Parameters from SAR Data for Land Applications, 21–23 October, 1998, ESTEC, Noordwijk, The Netherlands, 'www.estec.esa.nl/conferences/ 98c07/review_open/papers/99mb04.pdf', checked 12 May 2005, 9 p.

Hoekman, D. and Quinones, M. 2000. Land cover type and biomass clas-sifications using AirSAR data for evaluation of monitoring scenarios in the Colombian Amazon, *IEEE Transactions on Geoscience and Remote Sens-ing*, **38**, p. 685–696.

Hussin, Y., Reich, R., and Hoffer, R. 1991. Estimating slash pine biomass using radar backscatter, *IEEE Transactions on Geoscience and Remote Sensing*, **29(3)**, p. 427–431.

Hutton, C., Adair, M., Forest, C., and Parashar, S. 2000. Radarsat-1 mo-

saic of Canada, Proceedings of the 22nd Canadian Symposium on Remote Sensing, Victoria, B.C., Canada, 21–25 August, 2000, National Resources Canada, 7 p.

Häme, T., Salli, A., and Lahti, K. 1992. Estimation of carbon storage in boreal forest using remote sensing data, Pilot study, in: The Finnish programme on climate change, Progress report, edited by M. Kanninen and P. Anttila, Publications of the Academy of Finland 3/92, Helsinki, Finland, p. 250–255.

Häme, T., Salli, A., Andersson, K., and Lohi, A. 1997. A new methodology for the estimation of biomass of conifer-dominated boreal forest using NOAA AVHRR data, *International Journal of Remote Sensing*, **18(15)**, p. 3211–3243.

Häme, T., Sirro, L., Rauste, Y., Ahola, H., van Brusselen, J., Schuck, A., Wegmüller, U., Wiesmann, A., and Hippi, I. 2003. Treaty enforcement services using earth observation (TESEO) theme carbon – Main results, Proceedings of the International Geoscience and Remote Sensing Symposium IGARSS 2003, Toulouse, France, 21–25 July, 2003, IEEE, Piscataway, NJ, USA, Vol. III, p. 1480–1482.

Israelsson, H., Ulander, L., Askne, J., Fransson, J., Frölind, P., Gustavsson, A., and Hellsten, H. 1997. Retrieval of forest stem volume using VHF SAR, *IEEE Transactions on Geoscience and Remote Sensing*, **35**, p. 36–40.

Jensen, A., 2005. Adjusted R_square, California State University, Sacramento, College of Business Administration, 1 p., "http://www.csus.edu/indiv/j/jensena/mgmt105/adjustr2.htm", checked 14.10.2005.

JRC 1990. MAESTRO 1, Airborne synthetic aperture radar (SAR) campaign 1989, Data report, Report number IRSA/MWT/1.90, version 2.0, June, 1990, Commission of the European Communities, Joint Research Centre, Ispra, Italy, 210 p.

Kauppi, P., Tomppo, E., and Ferm, A. 1995. C and N storage in living trees within Finland since 1950s, *Plant and Soil*, **168**–**169**, p. 633–638.

Keil, M, Winter, R., and Hönsch, H. 1994. Tropical rainforest investigation in Brazil using ERS-1 SAR data, Proceedings of the Second ERS-1 Symposium – Space at the Service of our Environment, Hamburg, Germany, 11–14 October, 1993, ESA SP-361 (January 1994), p. 481–484.

Kellndorfer, J. and Ulaby, F. 2003. Forest biomass inversion from SAR

using object oriented image analysis techniques, Proceedings of the International Geoscience and Remote Sensing Symposium IGARSS 2003, Toulouse, France, 21–25 July, 2003, IEEE, Piscataway, NJ, USA, Vol. 6, p. 3465–3467.

Koskinen, J., Pulliainen, J., Hyyppä, J., Engdahl, M., and Hallikainen, M. 2001. The seasonal behavior of interferometric coherence in boreal forest, *IEEE Transactions on Geoscience and Remote Sensing*, **39**, p. 820–828.

Kuplich, T. and Curran, P. 1999. Temporal analysis of JERS-1/SAR images over regenerating forests in Brazilian Amazonia, Proceedings of the International Geoscience and Remote Sensing Symposium IGARSS'99, Hamburg, Germany, 28 June – 2 July, 1999, IEEE, Piscataway, NJ, Vol. 4, p. 1895–1897.

Kuntz, S., Siegert, F., and Rücker, G. 1999. ERS SAR images for tropical rainforest and land use monitoring: change detection over five years and comparison with Radarsat and JERS SAR images, Proceedings of the International Geoscience and Remote Sensing Symposium IGARSS'99, Hamburg, Germany, 28 June – 2 July, 1999, IEEE, Piscataway, NJ, Vol. 2, p. 910–912.

Kwok, R., Rignot, E., Way, J., Freeman, A., and Holt, J. 1994. Polarization signatures of frozen and thawed forests of varying environmental state, *IEEE Transactions on Geoscience and Remote Sensing*, **32**, p. 371–381.

Leberl, F. 1975. Sequential and simultaneous SLAR block adjustment, *Photogrammetria*, **31**, p. 39–51.

Leclerc, G., Beaulieu, N., and Bonn, F. 2001. A simple method to account for topography in the radiometric correction of radar imagery, *International Journal of Remote Sensing*, **22(17)**, p. 3553–3570.

Lecomte, P. and Attema, E. 1992. Calibration and validation of the ERS-1 wind scatterometer, Proceedings of the First ERS-1 Symposium – Space at the Service of our Environment, Cannes, France, 4–6 November, 1992, European Space Agency, Paris, p. 19–29.

Lewis, J., Schnapf, A., Diesen, B., Martin, P., Schwalb, A., and Bandeen, W. 1983. Meteorological satellites, in Manual of remote sensing, Volume I, eds. Simonett, D. and Ulaby, F., American Society of Photogrammetry, Falls Church, Virginia, USA, p. 651–679.

Louet, J. 2001. The Envisat mission and system, *ESA bulletin* 106, June 2001, http://www.esa.int/esapub/bulletin/bullet106/bul106_1.pdf, checked 3.5.2005, p. 14–25.

Luckman, A., Baker, J., Kuplich, T., Yanasse, C., and Frery, A. 1997. A study of the relationship between radar backscatter and regenerating tropical forest biomass for spaceborne SAR instruments, *Remote Sensing of Environment*, **60(1)**, 1–13.

Menges, C., van Zyl, J., Hill, G., and Ahmad, W. 2001. A procedure for the correction of the effect of variation in incidence angle in AIRSAR data. *International Journal of Remote Sensing*, **22(5)**, p. 829–841.

Moore, R., Chastant, L., Porcello, L., and Stevenson, J. 1983. Imaging radar systems, in Manual of remote sensing, Volume I, eds. Simonett, D. and Ulaby, F., American Society of Photogrammetry, Falls Church, Virginia, USA, p. 429–474.

Morain, S. and Simonett, D. 1967. K-band radar in vegetation mapping, *Photogrammetric Engineering*, **33**, p. 730–740.

NASDA 1988. Earth Resource Satellite-1, National Space Development Agency of Japan, Tokyo, Japan, 1988, 4 p.

NOAA 2005. World Vector Shoreline, 'http://rimmer.ngdc.noaa.gov/mgg/coast/wvs.html', checked 26 April 2005.

Noltimier, K., Jezek, K., Sohn, H., Li, B., Liu, H., Baumgartner, F., Kaupp, V., Curlander, J., Wilson, B., and Onstott, R. 1999. Radarsat Antarctic mapping project – Mosaic construction, Proceedings of the International Geoscience and Remote Sensing Symposium IGARSS'99, Hamburg, Germany, 28 June – 2 1999, IEEE, Piscataway, NJ, USA, Vol. 5, p. 2349–2351.

Pierce, L., Liang, P., Dobson, C., Kellndorfer, J., Barros, O., dos Santos, J., and Soares, J. 2003. Regrowth biomass estimation in the Amazon using JERS-1/Radarsat SAR composites, Proceedings of the International Geoscience and Remote Sensing Symposium IGARSS 2003, Toulouse, France, 21–25 July, 2003, IEEE, Piscataway, NJ, USA, Vol. 3, p. 1933–1935.

Pravdo, S., Huneycutt, B., Holt, B., and Held, D. 1983. Seasat synthetic-aperture radar data user's manual, JPL Publication 82-90, Jet Propulsion Laboratory, California Institute of Technology, Pasadena California, 1 March, 1983, 113 p.

Press, W., Teukolsky, S., Vetterling, W., and Flannery, B. 1992. Numerical recipes in C: The art of scientific computing, Cambridge University Press, Cambridge, U.K., 2nd edition, p. 83–85.

Pulliainen, J., Kurvonen, L., and Hallikainen, M. 1999. Multitemporal behaviour of L- and C-band SAR observations of boreal forest, *IEEE Transactions on Geoscience and Remote Sensing*, **37**, p. 927–937.

Pulliainen, J., Engdahl, M., and Hallikainen, M. 2003. Feasibility of multitemporal interferometric SAR data for stand-level estimation of forest stem volume, *Remote Sensing of Environment*, **85**, p. 397–409.

Quegan, S., Le Toan, T., Yu, J., Ribbes, F., and Floury, N. 2000. Multitemporal ERS SAR analysis applied to forest mapping, *IEEE Transactions on Geoscience and Remote Sensing*, **38(2)**, p. 741–753.

Ranson, K. and Sun, G. 1994. Mapping biomass of a northern forest using multifrequency SAR data, *IEEE Transactions on Geoscience and Remote Sensing*, **32(2)**, p. 388–396.

Ranson, K., Saatchi, S., and Sun, G. 1995. Boreal forest ecosystem characterization with SIR-C/XSAR, *IEEE Transactions on Geoscience and Remote Sensing*, **33(4)**, p. 867–876.

Ranson, K. and Sun, G. 2000. Effects of environmental conditions on boreal forest classification and biomass estimates with SAR, *IEEE Transactions on Geoscience and Remote Sensing*, **38**, p. 1242–1252.

Rauste, Y. 1988. Rectification of spaceborne SAR images using polynomial rectification and a digital elevation model, *Photogrammetric Journal of Finland*, **11**, p. 53–67.

Rauste, Y. 1991. Results of measurements on forest geometric parameters of the Freiburg site 12–18 June 1991, VTT, Espoo, unpublished project report, 9 p.

Richards, J., Sun, G., and Simonett, D. 1987. L-band radar backscatter modeling of forest stands, *IEEE Transactions on Geoscience and Remote Sensing*, **25(4)**, p. 487–498.

Rignot, E. and van Zyl, J. 1993. Change detection techniques for ERS-1 SAR data, *IEEE Transactions on Geoscience and Remote Sensing*, **31(4)**, p. 896–906.

Rosaz, J., Maitre, H., and Rudant, J. 1994. Mosaicking ERS-1 images: Difficulties, solutions and results on the French Guyana, Proceedings of the Second ERS-1 Symposium – Space at the Service of our Environment, Hamburg, Germany, 11–14 October, 1993, ESA SP-361 (January 1994), p. 1221–1226.

Rosenqvist, A. 1996. The global rain forest mapping project by JERS-1 SAR, International Archives of Photogrammetry and Remote Sensing, ISPRS, Vienna, Austria, Vol. 31, Part B7, p. 594–598.

Rosenqvist, A., Shimada, M., Chapman, B., Freeman, A., De Grandi, G., Saatchi, S., and Rauste, Y. 2000. The Global Rain Forest Mapping project – a review, *International Journal of Remote Sensing*, **21(6&7)**, p. 1375–1387.

Rosenqvist, A., Shimada, M., Chapman, B., McDonald, K., De Grandi, G., Jonsson, H., Williams, C., Rauste, Y., Nilsson, M., Sango, D., and Matsumoto, M., 2004. An overview of the JERS-1 SAR Global Boreal Forest Mapping (GBFM) project, Proceedings of IGARSS 2004, Anchorage, Alaska, USA, Sept. 20–24, 2004, p. 1033–1036.

Rosisch, B. and Meadows, P. 2004, Absolute calibration of ASAR level 1 products generated with PF-ASAR, Technical Note, European Space Agency, ESA/ESRIN, Frascati, Italia, 23 January, 2004, 23 p.

Rudner, L., Glass, G., Evartt, D., and Emery, P. 2002. A user's guide to the meta-analysis of research studies, ERIC Clearinghouse on Assessment and Evaluation, University of Maryland, College Park, chapter 9, 7 p. "http://www.erdres.org/meta/chap9/chap9.htm", checked 14.10.2005.

Saatchi, S. and Moghaddam, M. 2000. Estimation of crown and stem water content and biomass of boreal forest using polarimetric SAR imagery, *IEEE Transactions on Geoscience and Remote Sensing*, **38**, p. 697–709.

Sader, S. 1987. Forest biomass, canopy structure, and species composition relationships with multipolarization L-band synthetic aperture radar, *Photogrammetric Engineering and Remote Sensing*, **53(2)**, p. 193–202.

Sader, S., Waide, R., Lawrence, W., and Joyce, A. 1989. Tropical forest biomass and successional age class relationships to a vegetation index derived from Landsat TM data, *Remote Sensing of Environment*, **28**, p. 143–156.

Santoro, M., Eriksson, L., Schmullius, C., and Wiesmann, A. 2004. Seasonal and topographic effects on growing stock volume estimates from JERS-1 backscatter in Siberian forests, Proceedings of the 23rd Symposium of the European Association of Remote Sensing Laboratories, Ghent, Belgium, 2–5 June 2003, Millpress Science Publishers, Rotterdam, the Netherlands, p. 151–158.

Santos, J., Araujo, L., Freitas, C., Sant'Anna, S., Dutra, L., Mura, J., Gama,

F., and Hernandez Filho, P. 2001. Inventory of forest biomass in Brazilian Amazon: A local approach using airborne P-band SAR data, Proceedings of the International Geoscience and Remote Sensing Symposium IGARSS 2001, Sydney, Australia, 9–13 July, 2001, IEEE, Piscataway, NJ, USA, Vol. 2, p. 786–788.

Santos, J., Pardi Lacruz, M., Araujo, L., and Keil, M. 2002. Savanna and tropical rainforest biomass estimation and spatialization using JERS-1 data, *International Journal of Remote Sensing*, **23**(**7**), p. 1217–1229.

Santos, J., Freitas, C., Araujo, L., Dutra, L., Mura, J., Gama, F., Soler, L., and Sant'Anna, S. 2003. Airborne P-band SAR applied to the above ground biomass studies in the Brazilian tropical rainforest, *Remote Sensing of Environment*, **87**, p. 482–493.

Shimada, M. 1996. Radiometric and geometric calibration of JERS-1 SAR, *Advances in Space Research*, **17**(**1**), p. 79–98.

Shimada, M. 2001. User's guide to NASDA's SAR products ver. 2, NASDA, Tokyo, Japan, 9 August, 2001, 23 p.

Shimada, M. and Isoguchi, O. 2002. JERS-1 SAR mosaic of Southeast Asia using calibrated path images, *International Journal of Remote Sensing*, **23**(**7**), p. 1507–1526.

Shimada, M., Tadono, T., and Matsuoka, M. 2002a. Calibration and validation of PALSAR, Proceedings of the International Geoscience and Remote Sensing Symposium IGARSS 2002, Toronto, Canada, 24–28 June, 2002, IEEE, Piscataway, NJ, USA, Vol. 1, p. 384–386.

Shimada, M., Tadono, T., Rosenqvist, A., and Shakil, A. 2002b. Incidence angle dependence of the L-band Pol-In-SAR sensitivity at forestry region – Alos PALSAR study using the Pi-SAR, Proceedings of the International Geoscience and Remote Sensing Symposium IGARSS 2002, Toronto, Canada, 24–28 June, 2002, IEEE, Piscataway, NJ, USA, Vol. 1, p. 632–634.

Shimada, M., Rosenqvist, A., Watanabe, M., and Tadono, T. 2005. The polarimetric and interferometric potential of ALOS PALSAR, Proceedings of POLinSAR 2005, 17–21 January 2005, 'earth.esa.int/workshops/polinsar2005/ participants/213/paper_Polarimetric_paper_S271587.pdf', checked 3.5.2005, 6 p.

Simard, M., de Grandi, G., Thompson, K., and Bennie, G. 1998. Analysis of speckle noise contribution on wavelet decomposition of SAR images,

IEEE Transactions on Geoscience and Remote Sensing, **36**, p. 1953–1962.

Siqueira, P., Hensley, S., Shaffer, S., Hess, L., McGarragh, G., Chapman, B., and Freeman, A. 2000. A continental-scale mosaic of the Amazon basin using JERS-1 SAR, *IEEE Transactions on Geoscience and Remote Sensing*, **38**, p. 2638–2643.

Small, D., Jehle, M., Meier, E., and Nüesh, D. 2004a. Radiometric terrain correction incorporating local antenna gain, Proceedings of EUSAR 2004, Ulm, Germany, 25–27 May, 2004, VDE Verlag, Frankfurt am Main, Germany, p. 929–932.

Small, D., Meier, E., and Nüesch, D. 2004b. Robust radiometric terrain correction for SAR image comparisons, Proceedings of the International Geoscience and Remote Sensing Symposium IGARSS 2004, Anchorage, Alaska, USA, 20–24 September, 2004, IEEE, Piscataway, NJ, USA, p. 1730–1733.

Smith, G. and Ulander, L. 1998. Forest biomass retrieval using VHF SAR. Retrieval of Bio- and Geophysical Parameters from SAR data for Land Applications, Symposium held in ESTEC Noordwijk, 21–23 October 1998, 'www.estec.esa.nl/conferences/98c07/papers/P027.PDF', checked on 13 May 2005, p. 301–307.

Smith, G. and Ulander, L. 2000. A model relating VHF-band backscatter to stem volume of coniferous boreal forest, *IEEE Transactions on Geoscience and Remote Sensing*, **38**, p. 728–740.

Sun, G. and Simonett, D. 1988. A composite L-band HH radar backscattering model for coniferous forest stands, *Photogrammetric Engineering and Remote Sensing*, **54**, p. 1195–1201.

Sun, G., Ranson, K., and Kharuk, V. 2000. Forest biomass estimation in Western Sayani mountains, Siberia from SAR, Proceedings of the International Geoscience and Remote Sensing Symposium IGARSS 2000, Honolulu, USA, 24–28 July, 2000, IEEE, Piscataway, NJ, USA, Vol. 1, p. 435–437.

Sun, G., Ranson, K., and Kharuk, V. 2002. Radiometric slope correction for forest biomass estimation from SAR data in the Western Sayani mountains, Siberia, *Remote Sensing of Environment*, **79**, p. 279–287.

Teillet, P., Guindon, B., Meunier, J., and Goodenough, D. 1985. Slope-aspect effects in synthetic aperture radar imagery, *Canadian Journal of Remote Sensing*, **11**, p. 39–49.

Le Toan, Beaudoin, A., Riom, J., and Guyon, D. 1991. Relating forest parameters to SAR data, Proceedings of the International Geoscience and Remote Sensing Symposium IGARSS'91, Helsinki University of Technology, Espoo, Finland, 3–6 June, 1991, IEEE, Piscataway, NJ, USA, Vol. 2, p. 689–692.

Tomppo, E. 1986. Stand delineation and estimation of stand variates by means of satellite images, Proceedings of the Seminars on Remote Sensing-Aided Forest Inventory, Hyytiälä, Finland, 10–12 December, 1986, Helsingin Yliopiston Metsänarvioimistieteen laitoksen tiedonantoja No. 19 (Research Notes No. 19, University of Helsinki, Department of Forest Mensuration and Management), p. 59–76.

Tsolomon, R., Tateishi, R., and Tetuko, J. 2002. A method to estimate forest biomass and its application to monitor Mongolian taiga using JERS-1 SAR data, *International Journal of Remote Sensing*, **22(22)**, p. 4971–4978.

Ulaby, F., Moore, R., and Fung, A. 1982. Microwave remote sensing, active and passive, Vol. II, Radar remote sensing and surface scattering and emission theory, (Addison Wesley Publishing Company, Reading, Massachusetts, USA), p. 457–1064.

Ulander, L. 1996. Radiometric slope correction of synthetic-aperture radar images, *IEEE Transactions on Geoscience and Remote Sensing*, **34**, p. 1115–1122.

Ulander, L. Askne, J., Fransson, J., Gustavsson, A., Le Toan, T., Manninen, T., Martinez, J-M. Melon, P., Smith, G., and Walter, F. 2000. Retrieval of stem volume in coniferous forest from low VHF-band SAR, Proceedings of the International Geoscience and Remote Sensing Symposium IGARSS 2000, Honolulu, USA, 24–28 July, 2000, IEEE, Piscataway, NJ, USA, Vol. 1, p. 441–443.

Villasenor, J., Fatland, D., and Hinzman, L. 1993. Change detection on Alaska's north slope using repeat-pass ERS-1 SAR images, *IEEE Transactions on Geoscience and Remote Sensing*, **31(1)**, p. 227–236.

Wagner, W., Luckman, Vietmeier, J., Tansey, K., Balzter, H., Schmullius, C., Davidson, M., Gaveau, D., Gluck, M., Le Toan, T., Quegan, S., Shvidenko, A., Wiesmann, A., and Yu, J. 2003. Large-scale mapping of boreal forest in SIBERIA using ERS tandem coherence and JERS backscatter data, *Remote Sensing of Environment*, **85**, p. 125–144.

Williamson, M. 1990. Radar in space, *Space*, **6**, p. 26–32.

Wulder, M. 2005, Correlation coefficient and coefficient of variation, Natural Resources of Canada, Canadian Forest Service, 1 p., "http://www.pfc.forestry.ca/profiles/wulder/mvstats/correl_coef_e.html", checked 14.10.2005.

Zebker, H. and Lou, Y. 1990. Phase calibration of imaging radar polarimeter Stokes matrices, *IEEE Transactions on Geoscience and Remote Sensing*, **28**, p. 246–252.

van Zyl, J., Zebker, H., and Elachi, C. 1987. Imaging radar polarisation signatures: Theory and observation, *Radio Science*, **22**, p. 529–543.

van Zyl, J. 1990. Calibration of polarimetric radar images using only image parameters and trihedral corner reflector responses, *IEEE Transactions on Geoscience and Remote Sensing*, **28**, p. 337–348.

Author(s)
Rauste, Yrjö

Title

Techniques for wide-area mapping of forest biomass using radar data

Abstract

Aspects of forest biomass mapping using SAR (Synthetic Aperture Radar) data were studied in study sites in northern Sweden, Germany, and south-eastern Finland. Terrain topography – via the area of a resolution cell- accounted for 61 percent of the total variation in a Seasat (L-band) SAR scene in a hilly and mountainous study site.

A methodology – based on least squares adjustment of tie point and ground control point observations in a multi-temporal SAR mosaic dataset – produced a tie point RMSE (Root Mean Square Error) of 56 m and a GCP RMSE of 240 m in the African mosaic of the GRFM (Global Rain Forest Mapping) project. The mosaic consisted of 3624 JERS SAR scenes. A calibration revision methodology – also based on least squares adjustment and points in overlap areas between scenes – removed a calibration artifact of about 1 dB.

A systematic search of the highest correlation between forest stem volume and backscattering amplitude was conducted over all combinations of transmit and receive polarisations in three AIRSAR scenes in a German study site. In the P-band, a high and narrow peak around HV-polarisation was found, where the correlation coefficient was 0.75, 0.59, and 0.71 in scenes acquired in August 1989, June 1991, and July 1991, respectively. In other polarisations of P-band, the correlation coefficient was lower. In L-band, the polarisation response was more flat and correlations lower, between 0.54 and 0.70 for stands with a stem volume 100 m^3/ha or less.

Three summer-time JERS SAR scenes produced very similar regression models between forest stem volume and backscattering amplitude in a study site in south-eastern Finland. A model was proposed for wide area biomass mapping when biomass accuracy requirements are not high. A multi-date regression model employing three summer scenes and three winter scenes produced a multiple correlation coefficient of 0.85 and a stem volume estimation RMSE of 41.3m^3/ha. JERS SAR scenes that were acquired in cold winter conditions produced very low correlations between stem volume and backscattering amplitude.

VTT PUBLICATIONS

574 Juslin, Kaj. A Companion Model Approach to Modelling and Simulation of Industrial Processes. 2005. 155 p. + app. 15 p.

575 Aura, Anna-Marja. *In vitro* digestion models for dietary phenolic compounds. 2005. 107 p. + app. 57 p.

576 Kyllönen, Hanna. Electrically or ultrasonically enhanced membrane filtration of wastewater. 2005. 79 p. + app. 54 p.

577 Monni, Suvi. Estimation of country contributions to the climate change. Viewpoints of radiative forcing and uncertainty of emissions. 2005. 99 p. + app. 76 p.

578 Hämäläinen, Anitta. Applying thermal hydraulics modeling in coupled processes of nuclear power plants. 2005. 103 p. + app. 99 p.

579 Korpipää, Panu. Blackboard-based software framework and tool for mobile device context awareness. 2005. 225 p.

580 Karppinen, Kaarina. Security Measurement based on Attack Trees in a Mobile Ad Hoc Network Environment. 2005. 57 p. + app. 8 p.

581 Urala, Nina. Functional foods in Finland. Consumers' views, attitudes and willing-ness to use. 2005. 79 p. + app. 109 p.

582 Human practice in the life cycle of complex systems. Challenges and methods. Edited by Maaria Nuutinen & Juha Luoma. 2005. 147 p.

583 Turunen, Erja. Diagnostic tools for HVOF process optimization. 2005. 66 p. + app. 92 p.

584 Measures for improving quality and shape stability of sawn softwood timber during drying and under service conditions. Best Practice Manual to improve straightness of sawn timber. Edited by Veikko Tarvainen. 2005. 149 p.

585 Hyötyläinen, Raimo. Practical interests in theoretical consideration. Constructive methods in the study of the implementation of information systems. 2005. 159 p.

586 Koivisto, Tapio. Developing strategic innovation capability of enterprises. Theoret-ical and methodological outlines of intervention. 2005. 120 p.

587 Ajanko, Sirke, Moilanen, Antero & Juvonen, Juhani. Kierrätyspolttoaineiden laadun-valvonta. 2005. 59 s.

588 Ebersberger, Bernd. The Impact of Public R&D Funding. 2005. 199 p. + app. 12 p.

589 Kutinlahti, Pirjo. Universities approaching market. Intertwining scientific and entre-preneurial goals. 2005. 187 p. + app. 4 p.

590 Jantunen, Erkki. Indirect multisignal monitoring and diagnosis of drill wear. 2005. 80 p. + app. 110 p.

591 Rauste, Yrjö. Techniques for wide-area mapping of forest biomass using radar data. 2005. 103 p. + app. 77 p.